Implementation of a bidirectional grid interface for an electric vehicle

MATHEUS MONTANINI BREVE

Supervised by

Prof. Dr. Américo Vicente Teixeira Leite

Prof. Dr. Luiz Francisco Sanches Buzachero

Prof. Dr. Ângela Paula Ferreira

Bragança

2018-2019

Implementation of a bidirectional grid interface for an electric vehicle

MATHEUS MONTANINI BREVE

Thesis presented in the School of Technology and Management of the Polytechnic Institute of Bragança to fulfill the requirements of a Master of Science Degree in Industrial Engineering (Electrical Engineering branch).

Supervised by

Prof. Dr. Américo Vicente Teixeira Leite

Prof. Dr. Luiz Francisco Sanches Buzachero

Prof. Dr. Ângela Paula Ferreira

Bragança

2018-2019

Acknowledgments

I would first like to thank my advisers of the IPB Prof. Dr. Américo Vicente Leite and Prof. Dr. Ângela Paula Ferreira for their support, document reviews, criticisms, discussions and suggestions, contributing directly to the achieved results. I would also like to acknowledge Prof. Batista for his help in the experimental steps of the thesis and Prof. Luíz Buzachero, who willingly accepted to be my superviser from the UTFPR in Brazil.

I would like to express my most profound gratitude to Marcio, my father, Murilo, my brother and Lara, my mother. Without them not only would my stay in Portugal have been impossible, but, without my mother's joy in my happy moments and unfailing support in difficult times, this present document would have stayed blank.

I am profoundly grateful to my girlfriend Charis Lieberum for her constant encouragement, support and company, especially in moments in which confidence was difficult to find. My thanks to her would fit a dedicated chapter.

I would like to thank my friends with whom I shared an apartment for almost an year in Bragança: Leonardo Candido, Lucas Azevedo and Luis Guilherme. With them I shared countless happy moments that will remain in memory whenever I remember my stay in Portugal, including long discussions about random topics, our theses, past and future travels and numerous stories.

Special thanks to all my friends and colleagues. Since mentioning all of them would be difficult, I would like to thank those I spent the most time with: João Teodoro, Gabriela Ribeiro, Isabella Scotta, Alberto Scortegagna, Bruna Freitas, Pedro Oleskovicz, Allana Netto, Wellington Maidana, Isabella Urbanetz, Lídia Ana, Nathalia Gonçales, Nadine Martelozo, Letícia Cena and William Molina.

My sincere thanks to Bruno Tangerino, a great friend who gave me useful advice whenever I needed, helping me with the visa, application and any other preparation processes related to Portugal. Finally, I would also like to acknowledge people not mentioned here who, whether directly or indirectly, contributed to the writing of this document.

Resumo

Sistemas de armazenamento de energia armazenam energia quando a produção excede a demanda. Veículos elétricos constituem um sistema de armazanemanto de energia, que, se integrado com a rede, pode melhorar sua estabilidade, eficiência e, além disso, ser uma fonte de renda adicional para seus proprietários, tecnologia denominada *vehicle-to-grid* (V2G).

Devido a clara relevância desta tecnologia em um futuro com veículos elétricos como principal meio de transporte, pesquisas são necessárias para analisar as possibilidades, ramificações, vantagens e desvantages da tecnologia V2G.

Com este propósito em mente, o principal objetivo desta tese é a implementação de uma interface de potência bidirecional monofásica entre a bateria de um veículo elétrico e a rede. O sistema proposto conta com funções como V2G para suporte à rede, *vehicle-to-home* (V2H) para alimentação de uma casa e *grid-to-vehicle* (G2V) para carregamento da bateria.

A modelagem, simulação e teste do sistema e suas funções foram realizados com o *software* MATLAB® e Simulink, permitindo a validação por simulação em domínio discreto. Para a validação experimental uma interface de controle em tempo real com componentes da dSPACE foi utilizada para a interface entre a estrutura de potência e o controle desenvolvido no Simulink em um esquema de teste *Hardware-in-the-Loop*, que permite a criação rápida de algoritmos de controle, aquisição, processamento e exportação de dados e com isto a validação experimental das funções implementadas.

Com a validação do sistema o objetivo principal da tese foi atingido e uma interface de potência bidirecional implementada com sucesso. O sistema proposto é estável, transiciona entre modos de operação suavemente e permite a definição das potências ativas e reativas a serem trocadas, função útil se os serviços a serem realizados pelos veículos são determinados externamente.

Palavras-chave: interface de potência bidirecional, interface veículo-rede, interface veículo-casa

Abstract

Battery storage systems store excess energy when energy production exceeds the demand. Electric vehicles constitute a distributed energy storage system and, if integrated with the supply grid, can improve grid stability, efficiency and be an additional revenue source for electric vehicle owners, technology denominated vehicle-to-grid (V2G).

Due to the clear relevance of this technology in a future where electrical vehicles are a major mean of transportation, research must be conducted to assess the possibilities, ramifications, advantages and disadvantages of V2G technology.

In order to contribute with further knowledge on this technology, the main objective of this thesis is the simulation and physical implementation of a bidirectional single-phase power interface between an electric vehicle battery and the grid. The proposed system counts with features such as V2G for grid support, vehicle-to-home (V2H) for powering a home and grid-to-vehicle (G2V) for regular battery charging.

The programs MATLAB® and Simulink were used for modelling, simulation and test of the system in a discrete simulation, allowing for conceptual validation of the power and control structure.

A real-time interface based from dSPACE was used to interface the hardware with the control algorithm developed in Simulink in a Hardware-in-the-Loop scheme, which allows rapid control prototyping, data acquisition, processing and export. Hence, a rigorous experimental validation of the implemented features.

With the system validation, the main thesis objective was reached and a bidirectional power interface was successfully implemented. The proposed system is stable, transitions smoothly between operation modes and allows the definition of the active and reactive powers to be exchanged, suitable if the services provided by the vehicles are defined externally.

Keywords: distributed storage, bidirectional power interface, vehicle-to-grid, vehicle-to-home

Contents

List of Tables

List of Figures

Acronyms

AC	Alternating Current
BADC	Bidirectional DC/AC Converter
BDC	Bidirectional DC/DC Converter
BEV	Battery Electric Vehicle
DC	Direct Current
ESTiG	Escola Superior de Tecnologia e Gestão
EV	Electric Vehicle
G2V	Grid-to-Vehicle
HEV	Hybrid Electric Vehicles
HIL	Harware-in-the-Loop
IGBT	Insulated-Gate Bipolar Transistor
IPB	Instituto Politécnico de Bragança
LSE	Laboratório de Sistemas Eletromecatrónicos
PHEV	Plug-in Hybrid Electric Vehicle
PID	Proportional-Integral-Derivative Control
PLL	Phase-Locked Loop
PV	Photovoltaic
SOC	State of Charge
SOH	State of Health
TSO	Tranmission System Operator
V2G	Vehicle-to-Grid
VGI	Vehicle and Grid Integration
VOC	Voltage-Oriented Control
VSI	Voltage-Source Inverter

List of Symbols

	Description	Unit if applicable
I	Electrical current	Ampere (A)
V	Voltage	Volts (V)
R	Resistance	Ohms (Ω)
L	Inductance	Henry (H)
C	Capacitance	Farad (F)
f	Frequency	Hertz (Hz or s^{-1})
ω	Angular frequency	Radians per second (rad/s)
ω_g	Grid angular frequency	Radians per second (rad/s)
t	Time	Seconds (s or Hz^{-1})
j	Imaginary unit	–
I_d	Current direct component	Ampere (A)
I_q	Current quadrature component	Ampere (A)
V_d	Voltage direct component	Volts (V)
V_q	Voltage quadrature component	Volts (V)
I_α	Current Alpha component	Ampere (A)
I_β	Current Beta component	Ampere (A)
V_α	Voltage Alpha component	Volts (V)
V_β	Voltage Beta component	Volts (V)
K_p	Gain - Proportional Component (PID)	-
K_i	Gain - Integral Component (PID)	-
K_d	Gain - Derivative Component (PID)	-

Chapter 1

Introduction

Electric vehicles are considered to be the next step in a long effort to reduce greenhouse-gas emissions and improve air quality in urban areas. Some cities plan to prohibit cars altogether by 2034, such as Hamburg, which intends to replace urban traffic with a public transport network as a viable alternative to driving a personal vehicle. As of 2018, older diesel vehicles are already forbidden to enter the two main roads of the city, affecting 214 thousand vehicles registered in the second largest city of Germany [1][2]. Other cities such as Paris, Mexico City, Madrid and Athens also have plans to keep diesel cars outside the city by 2025, as a desperate measure to improve air quality [3].

These measures are part of an overall trend present worldwide. Pushed by environmental concerns, they intend to promote electric vehicle (EV) fleets instead of internal combustion vehicle (IC) fleets, helping countries reach their reduction objectives concerning greenhouse-gas emissions. Therefore, allied with decreasing prices for battery packs, subsidies from governments, organizations promoting electric vehicle usage, governments rising taxes related to IC vehicles and the "Dieselgate" scandal, EVs appear as an alternative which is emission-free, silent and, with recently explored technologies such as vehicle-to-grid technology, could even help support the electric supply grid.

1.1 Organizations and initiatives

Various initiatives and organizations, both government backed or not, have been created in the recent decades to push forward the adoption of electric vehicles. One of the earliest organizations was created in Japan in 1996 by the Japanese Electric Vehicle Association and integrated into the Clean-Energy Vehicles Introduction Programme (CEV) two years later,

which also promoted methanol-fueled vehicles, compressed natural gas vehicles and, for the first time, hybrid electric vehicles (HEV) [4]. An example of a global cooperation is the Clean Energy Ministerial (CEM), an annual high-level forum in which energy ministers and other delegates discuss topics concerning three main areas: energy efficiency, clean energy supply and clean energy access worldwide. Founded in 2009 at the United Nations Framework Convention on Climate Change in Copenhagen [5], 26 countries are members as of 2018. One of the several initiatives launched by the CEM is called Electric Vehicles Initiative (EVI). Launched in 2010, it is a policy with the intention of accelerating the adoption of electric vehicles worldwide [6]. To achieve this goal, a campaign called "EV30@30" was created in 2017 by the EVI. Its objective is to make electric vehicles reach a market share of 30% by the year 2030 with the collaboration of governments, the private sector, nongovernmental institutions and aligned international initiatives.

In 2010 the German federal government together with industry representatives created the *Nationale Plattform Elektromobilität* (NPE), a platform with the vision of electrical mobility being widely accepted in society. Its objectives are to transform Germany into a market leader and have at least 1 million electric cars on the streets, quantity that, according to the NPE reports, will be reached by the year 2022 [7]. The NPE is part of the *Integriertes Energie- und Klimaprogramm* (IEKP) [8], a collection of 29 measures proposed in 2007 by the German government to address climate change and incentive the expansion of renewable energies and greater energy efficiency.

The Portuguese government launched in 2008 the program MOBI.E. Counting with the collaboration of local energy suppliers such as Galp and EDP, approximately four hundred charging stations have been distributed across the country as of 2018 and made available to electric cars owners [9]. Slow charging stations will remain free of charge until 2019 while fast charging stations, on the other hand, are no longer free of charge. One of the main objectives of MOBI.E is to constitute a powerful incentive for the development of knowledge and technologies around electric mobility, attracting companies and industries to Portugal. Environmental issues are also cited, with hopes that the incentive will curb greenhouse gas emissions, especially in larger population areas [10].

Electrical vehicles are being introduced in Brazil at a much slower rate, especially compared to European countries or the US. Due to the low demand and high costs, usually prohibitive to the average population, few sparse initiatives, mostly municipal or state backed and based on incentives via tax deductions, are being created to increase the market growth rate of EVs. Federal incentives or federal-backed organizations dedicated to promoting them are still nonexistent. The prefecture of the city of São Paulo can be cited as an example, having promulgated a municipal law in 2014 to promote the usage of hybrid or purely electrical vehicles, allowing the return of half of the vehicle tax to the owner and the possibility of using the vehicle even during periods of vehicle restrictions in the city [11] [12].

1.2 Market expansion of electric vehicles

With a growing number of initiatives and governmental incentives to promote electric vehicles as well as environment-related pressure, electric vehicles sales are also growing. According to the "Global EV Outlook" report released by the International Energy Agency in 2018, 1.1 million electric cars were sold globally in 2017 [13], a 54% increase compared with the year before. China was responsible for approximately half of the cars sold in this time period, followed by the United States responsible for 17% and the European members of the CEM responsible for 20% of the global market share. Figure 1.1 shows the evolution of the number of electric vehicles in circulation from 2013 to 2017 and its distribution in China, the US, Europe and other countries.

Two scenarios are investigated in the "Global EV Outlook" report, the "EV30@30" scenario and New Policies scenario. The "EV30@30" scenario is related to the campaign with the same name launched in the 8^{th} Clean Energy Ministerial forum. It sets the goal for EVI country members to achieve 30% of market share for EVs by 2030. The latest is a scenario comprising the already implemented governmental policies and measures and their probable future effects. In this New Policies scenario, 125 million EVs are expected to be on the road by 2030, while in the "EV30@30" scenario this number could surpass the mark of 200 million EVs on the road. Figure 1.2 shows the predicted evolution of the number of electric vehicles on the

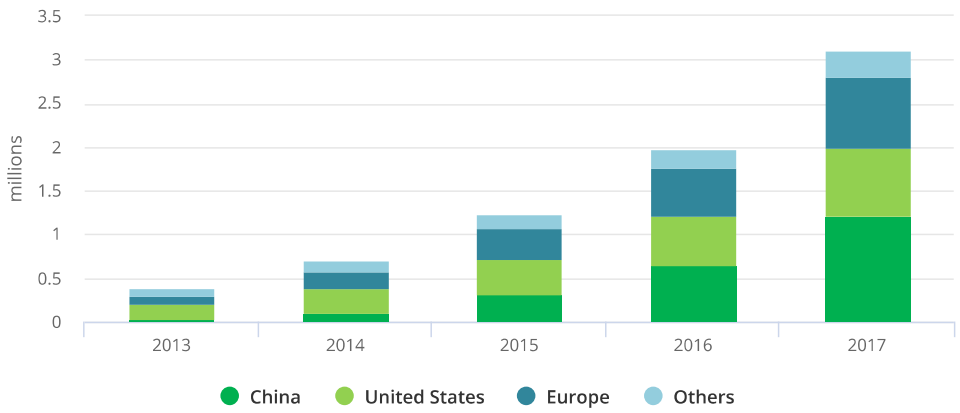

Figure 1.1: Percentage of global EV market share distribution (Taken from GEVO 2018 Key Findings [14]).

road by type from 2017 to 2030 under the conditions of both the New Policies and EV30@30 scenarios.

This significant increase in the numbers of EVs can be tracked down to two main factors, the decreasing price of battery packs, thus reducing the vehicles overall price and increasing their affordability, as well as efforts from traditional car manufacturers to develop and introduce electric vehicles in the market due to growing competition in the sector. Since the battery is the priciest component in an EV, dictating the range of EVs and, as consequence, the price range and market targets of different vehicles models, analyzing the price evolution of batteries can provide valuable information on the future growth of EVs. Lithium-ion based

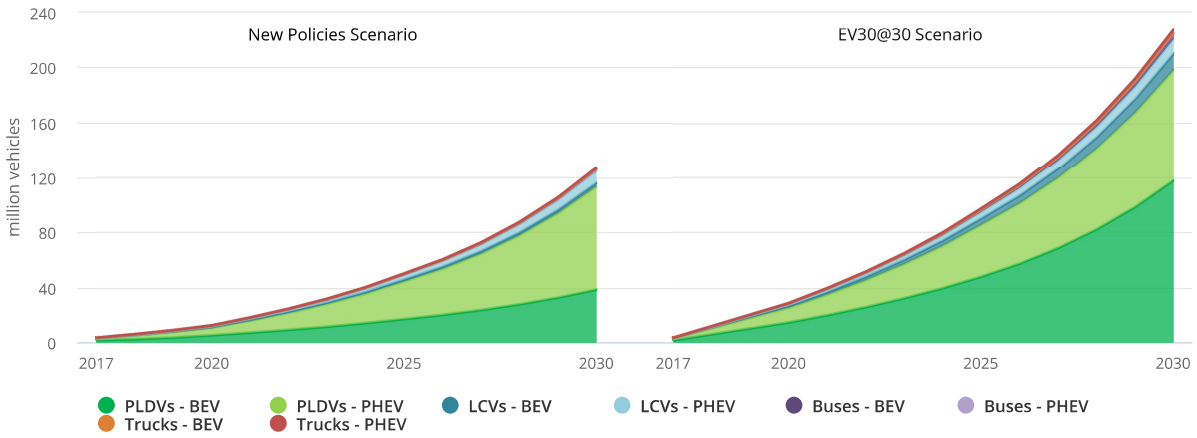

Figure 1.2: Predicted evolution of the number of electric vehicles on the road by type from 2017 to 2030 under the conditions of both the New Policies and EV30@30 scenarios. Acronyms: *BEV* - Battery Electric Vehicle, *PHEV* - Plug-in Hybrid Electric Vehicle, *LCV* - Light Commercial Vehicle, *PLDV* - Passenger Light-Duty Vehicle (Source: GEVO 2018 Key Findings [14]).

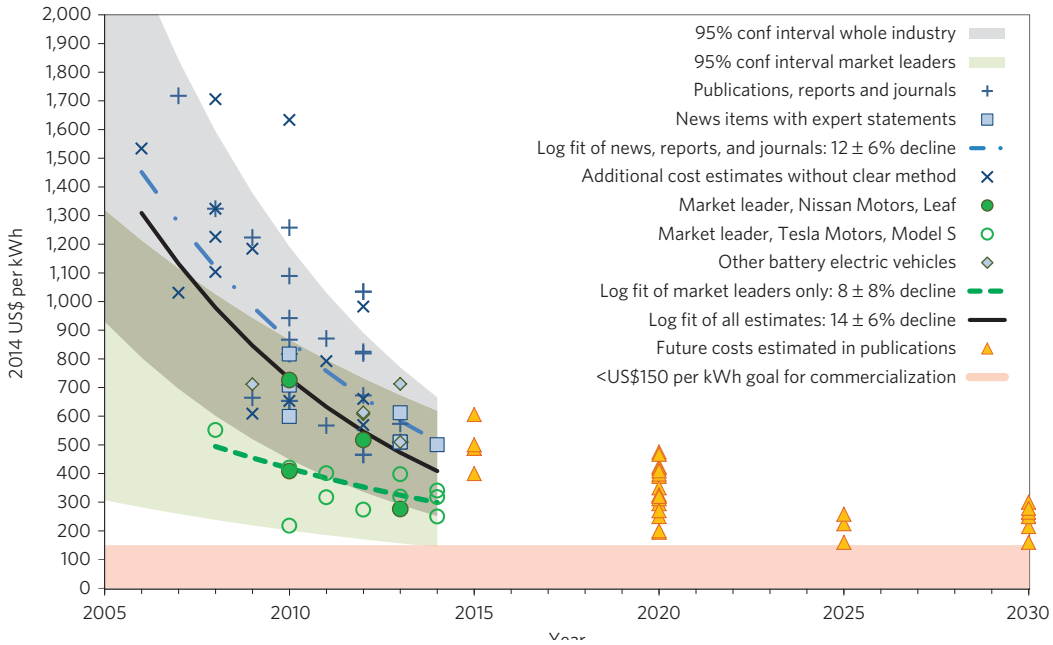

Figure 1.3: Price evolution in US dollars per kWh for different vehicle battery packs and predictions for the upcoming years (Source: [16]).

batteries, for example lithium-ion and lithium polymer batteries, are considered the standard for EV applications due to their high energy density [15].

Nykvist and Nilsson [16] analyzed the evolution of the prices of electric vehicles battery packs by collecting information published in papers, from statements by industry experts and from electric vehicles already in the market, such as Tesla Model S and Nissan Leaf (Figure 1.3). They estimated a 8% annual cost decrease for batteries in BEVs taking into account the market leaders [16]. As mentioned in the paper, estimations of price have a high level of uncertainty, since not only is the data sparse, but the industry is secretive about their batteries and their technical data. Still, it is reasonable to say that, based on the Global EV Outlook and Nykvist and Nilsson's paper, prices of batteries will continue dropping in the next years. The commercialization goal of producing batteries costing under 150 USD per kWh will be reached, according to the predictions, between the years 2025 and 2030. By then, together with subsidies from governments, increased environmental awareness and lower prices, electrical cars will provide enough advantages to replace most if not all internal combustion vehicles.

With the number of EVs on the road rising every year, so does the energy demand to charge them. In some countries, such as Norway, Sweden and Iceland gross final energy consumption is largely based on renewable energies, approximately 70%, 54% and 73% respectively as of 2016 [17]. Renewable energies, in most cases, operate under certain conditions, for example, photovoltaic with enough solar radiance, wind energy with sufficient wind speeds and, therefore, cannot be relied upon to supply energy whenever needed. This problem is commonly referred to as the "duck chart" problem. Coined by the California Independent System Operator in 2013, it refers to the shape that can be seen in a hourly electric load graph as depicted in Figure 1.4, which resembles a duck [18]. In technical terms, the graph shows the potential overgeneration with the increase of renewable energies active in a national electric grid over the years.

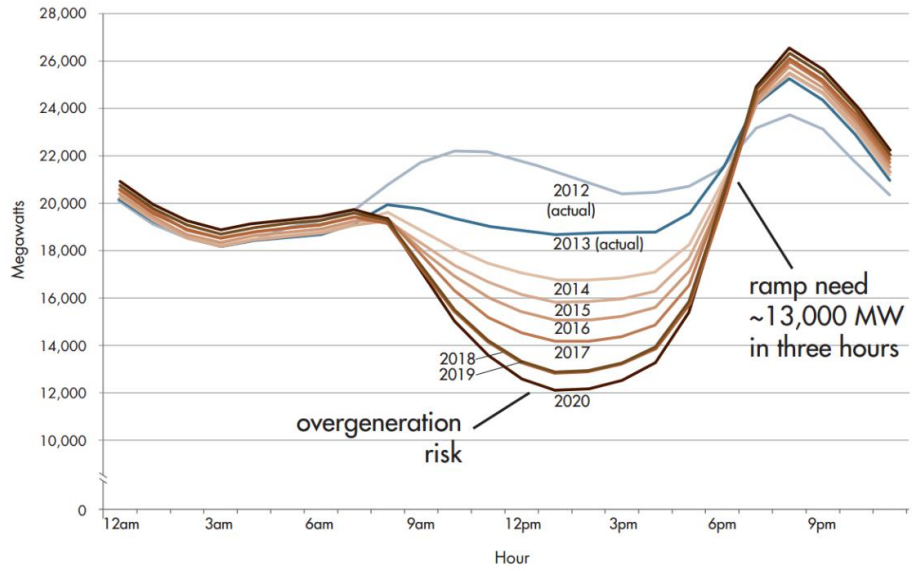

Figure 1.4: California Independent System Operator "duck chart". Taken from Denholm, O'Connell, Brinkman, *et al.* technical report [18].

In the chart, each line represents the net load, equal to the normal load minus wind and photovoltaic generation. During daytime PV generation increases proportionally to the solar radiation intensity, reaching its maximum generated power between 1 and 3 pm. California has a number of other traditional energy sources to help regulate and stabilize its energy grid, while, for example, Hawaii, with fewer traditional power plants and limited land area, is suffering from a similar effect due to its distributed photovoltaic generation, found on

residential and commercial rooftops around the country [19].

The situation in Hawaii has reached a critical point. In certain periods of peak solar radiation, Hawaii net electric load can become negative, pressuring the development of new strategies to regulate the grid energy balance. These strategies are complex for numerous reasons, for example, there are many non-monitored customer-owned PV systems installed on rooftops across the islands, making the control of the produced energy complicated if not impossible. The situation has led to controversial measures, such as approval of new policies and requirements to be fulfilled by even small-scale PV systems that customers may wish to install at their homes [19].

Solutions to this issue have been proposed and investigated in the past decades. The simplest one is building more power plants that can be regulated directly by the grid operators, called dispatchable sources, a category to which most of the traditional energy sources, i.e. coal or gas, belong. Due to environmental issues, countries are striving to cut down emissions of greenhouse gases, as a consequence gas and coal power plans are currently being phased out in many countries, although some intend to maintain a small number of traditional power plants operating as a form of backup [20] [21]. Besides, these power plants are not operationally flexible, that is, they have long activation and deactivation delays and a certain time to reach the full load generation power, effectively inhibiting their use to level the grid energy balance [22].

Other sources, such as geothermal and hydroelectric, are employed extensively due to their relatively constant and reliable energy production, requiring on the other hand great land area, a significant initial capital investment and years to finish construction and to finally become operational, thus not commercially viable in some locations. Additionally, most geothermal plants are considered inflexible and used for base-load purposes, hence not fully appropriate for the overgeneration issue at hand, even though newer developments in power plant and control techniques might turn geothermal plants into a more flexible energy source [23].

As an alternative to these solutions, battery storage systems are being further explored and can already be encountered in a deployment phase. Companies like Helen from Finland and

Tesla from the United States are building commercially-viable energy storage complexes with li-ion batteries. Tesla for example built the world's largest lithium-ion battery in Hornsdale, Australia, with a capacity of over 120 MWh [24], while Helen built the largest electricity storage system in the Nordic countries with a 600 kWh capacity, capable of momentarily storing energy from the Suvilahti solar power plant located in the Suvilahti district in Helsinki [25]. Allied to the aforementioned declining battery prices, low land area usage due to their compact nature and short construction times, storage systems can be considered an upcoming trend to solve the energy balance issue in places like Hawaii or California.

1.3 Electric vehicles as a distributed energy storage system

The facilities of Tesla and Helen mentioned as examples are central storage systems whereas electric vehicles with batteries, such as plug-in hybrid and battery electric vehicles, can serve as a distributed and mobile energy storage or generation system that can be integrated with the electric grid, integration often shortened as VGI. Not only has this technology the potential to be useful to grid operators, but to customers as well. Enabling information and power exchange between grid operators and electric vehicles owners would allow customers to charge their cars during low-energy-demand hours and discharge energy into the grid during peak-demand hours, technique called peak shaving (FIgure 1.5, for example. Grid operators on the other hand could benefit from an additional grid stabilization source by allowing peak shaving, which could prove useful in situations similar to those faced by Hawaii or California, which will become more prominent in other countries where the usage of photovoltaic energy is also growing, enabling a clean electricity grid [26].

With the capability of electric vehicles to exchange power with the grid, vehicles could therefore become an additional part of the power grid. Some car models that have been announced recently, the new Nissan Leaf, possess this technology and might help with grid stabilization, pre-qualifying as a large power station under the German Transmission System Operators (TSOs) guidelines according to Nissan [28].

The integration of vehicles and the electrical grid varies depending on the type of vehicle

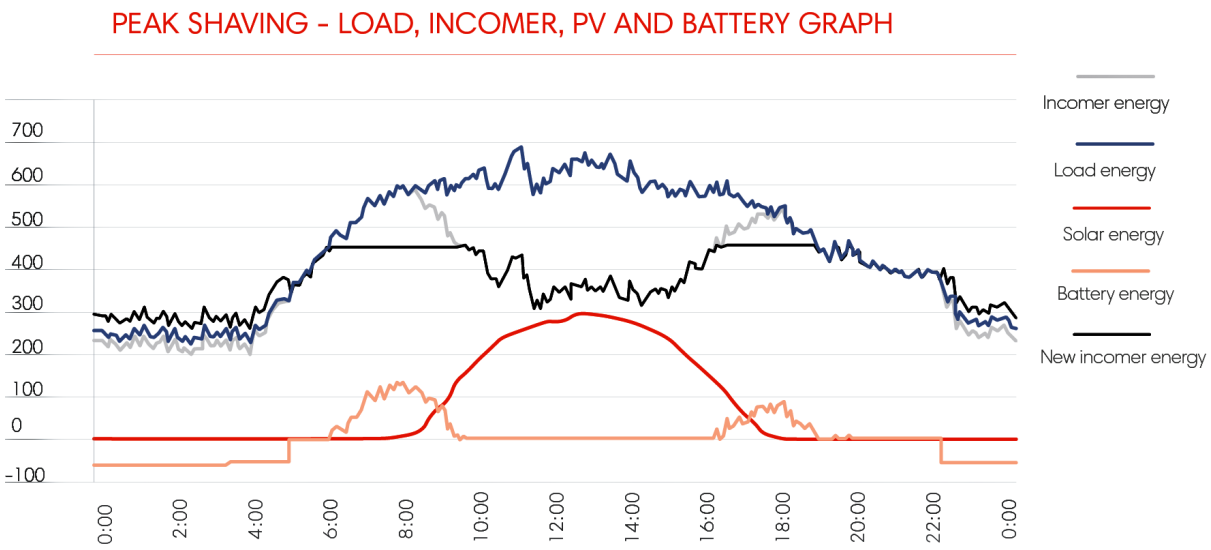

Figure 1.5: Example of peak shaving (Source: SOLA [27]).

and energy flux direction. Integration with an unidirectional power flow usually consists of smart charging methods and it is often referred as V1G. Smart charging techniques can take into account the price of electricity to charge the battery in certain day periods during which electricity is cheaper, which happens with time-of-use-based electricity prices. Bidirectional power flow, denominated as V2G, allows for power to be extracted from or delivered to the grid on the expense of little additional equipment compared to V1G. Besides, V2G is estimated to be in average 13 times more valuable considering the value provided to the grid if participating in electricity markets [29].

Other types of electric vehicles, such as hybrid electric vehicles (HEV), cannot be charged from an external energy source, instead relying on power from the internal combustion motor using power from a small-sized battery to only improve motor efficiency. Plug-in hybrid electric vehicles (PHEV), on the other hand, can be charged externally, similar to purely battery-based electric vehicles (BEV), being these vehicle types the target for bidirectional vehicle-to-grid integration. The possibility of a bidirectional power flow could also be used to power homes during short electricity shortages, electric grid instabilities or to store energy while charging in low-energy demand times and selling the stored energy back when energy demand is higher, mentioned as Vehicle-to-Home (V2H).

Vehicle-to-Home is a feature built in the latest model of the aforementioned Nissan

Leaf [30]. V2H could help reduce consumption of grid power in periods of the day when demand is highest and thus costlier, or simply as a backup power supply in case of emergencies. Usage of this system requires installation of a power controller acting either as a battery charging system or home energy supplier. According to the Nissan Leaf specifications, its battery has a 40 kWh capacity. With a maximum power output as energy supplier of 6 kW [30], it could power a home load of 6 kW for approximately 7 hours. This technology could become important taking into account the expanding connectivity between home appliances in a Smart Home scenario and the growing number of households with renewable energy sources like photovoltaics (PV). Tuttle, Fares, Baldick, *et al.* [31] analyzed a scenario in which an EV is used for backup power. Depending on the vehicle configuration, time of the year and integration with PV systems, an EV could provide up to 600 hours of backup power. An example of EV integration is shown in Figure 1.6.

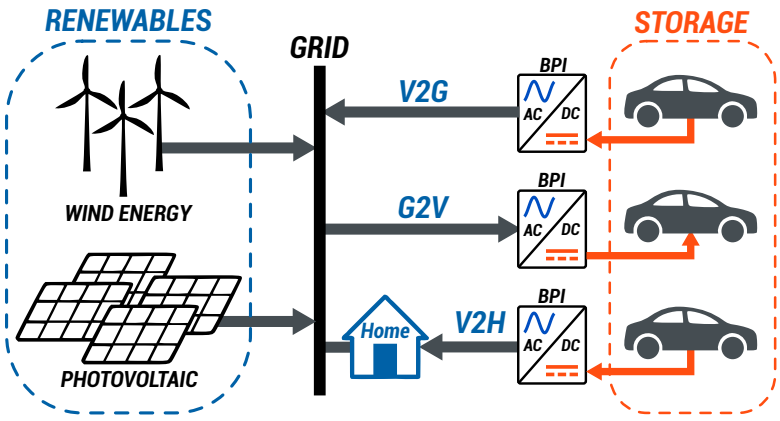

Figure 1.6: Opportunities for electric vehicle integration with the supply grid.

Usage of electric vehicles as a power source for utilities was first analyzed by Kempton and Letendre back in 1997. Impacted by the constant increase of the number of EVs in use, this concept has propelled investigations on many related concepts, such as possible benefits and disadvantages, resulting issues and probable solutions, as well as future research trends [29][33][34][35][36]. Given the topic's clear importance in a future dominated by smart and connected systems, V2G/H has the potential to drastically change how EVs are used within society, thus its potentials have to be further explored and its drawbacks investigated with depth.

1.4 Related challenges

Usage of V2G or V2H technologies faces many challenges since it is a still immature technology, posing many implications to different sectors of society. The main challenges it faces can be summarized in four topics: technology adoption rate, consumer payment and contract terms, power exchange control coordination and optimization, and the related battery wear. Several authors have analyzed these challenges, for instance Tan, Ramachandaramurthy, and Yong [34], Sovacool, Noel, Axsen, *et al.* [35] and Sovacool, Axsen, and Kempton [29]. Due to the complexity and many possible ramifications, only the main challenges are addressed and briefly explained in this section.

1.4.1 Technology adoption

A single BEV or PHEV does not possess a useful amount of energy storage, but an electric vehicle fleet might provide sufficient energy storage to be useful for grid operators. Thus, efficiency and feasibility of V2G in a large scale depends heavily on the adoption of electric vehicles. Even if EVs are the main transportation mean, bidirectional power flow, used for V2G, requires EVs with proper equipment. Although electric vehicles tends to expand in numbers in the near future, as evidenced by the findings in [13], V2G adoption on the other hand depends not only on overcoming technical obstacles, but also on social barriers.

A survey conducted by Parsons, Hidrue, Kempton, *et al.* [37] addressed the willingness of consumers to acquire vehicles with V2G capabilities and also how different conditions and restrictions, as consequence of V2G, affect consumers' choice on contract terms. The survey suggests that consumers are extremely sensitive to V2G restrictions and perceive a high inconvenience cost related to V2G-EV contracts. Possible reasons for this outcome is the drivers' preference for flexibility - that is, not be restricted by a contract determining when to provide services to the grid, as well as unawareness of car idleness.

Geske and Schumann [38] suggest that adoption of V2G depends heavily on two factors: range anxiety, or fear that the vehicle does not have sufficient charge to reach its destination, and the desired minimum range, value that EV owners must set, restricting how much energy

grid operators could withdraw from the vehicle. These factors are deemed more important than remuneration to determine EV-owners willingness to adopt the technology, a conclusion shared by Parsons, Hidrue, Kempton, *et al.* [37].

These surveys support tailoring V2G based on consumers' needs, reducing the inconvenience perceived by customers and thus increasing the technology attractiveness and the percentage of EV owners participating in V2G-based services for the power grid, increasing the overall system efficiency.

1.4.2 Financial-related issues

Kempton and Tomić [39] claim that V2G is only useful if its energy is sold to high-value and short-duration power markets, providing ancillary services, which include services such as peak power shifting, frequency regulation or spinning reserve services. This is due to the low durability and high cost per kWh of electric energy in electric vehicles, thus limiting the V2G usage for these specific purposes in order to be economically viable and to take advantage of the main advantages of V2G, which include its quick response time, low standby costs, and low capital cost per kW.

This raises the question of how to determine the payback value each EV owner should receive in return for the vehicle availability to provide grid-support services. Different factors might influence that, such as service type provided, duration and time of vehicle availability, energy price and energy quantity exchanged, minimum battery charge level the customer desires and several other factors, therefore making definition of policies, contract terms and possible revenue difficult to assess, issue that was already taken into account by Kempton and Tomić [39], who devised methods for estimating revenue from V2G services, but with the downside of basing the results on a single vehicle, thus less relevant in a context where a fleet is used for this purpose.

1.4.3 Communication and control

Communication is necessary to allow grid operators to decide which types of services are most needed, coordinating the EV fleet as necessary. Given the distributed nature of V2G, communication between the power grid operators and the vehicles becomes an issue and must also be further researched. Different strategies have been proposed to simplify communication, such as creation of hierarchical structures, in which EVs would be subjected to decisions of an aggregator, such as a parking lot operator, which would be responsible for managing the parked vehicles while fulfilling the desired service requested by a higher hierarchy level, the grid operator for example. Still, the problem related to control remains, that is, how grid operators or aggregators will coordinate individual vehicles to achieve a common goal. This challenge has been further investigated in the past years, with for example Nguyen, Zhang, and Mahmud [40] devising a centralized control strategy in a micro-grid with high renewable energy penetration, Krueger and Cruden [41] suggesting a modular strategy for V2G control and Liu, Wang, Jia, *et al.* [42] proposing an aggregative architecture to integrate PHEVs and BEVs into a power system.

1.4.4 Battery wear

One of the downsides often mentioned concerning V2G technology is the potentially higher associated battery wear compared to that of regular driving, thus reducing battery life span and damaging EV owners. Battery wear can be measured by the battery state of health (SOH), itself a function of numerous variables, such as ambient and cell temperature, depth of discharge (DOD), number of charge and discharge cycles, charge and discharge rates, total energy withdrawn from the battery, the state of charge (SOC) and the battery chemistry as well [43]. Due to the high number of factors influencing battery health, it is often challenging to develop accurate models to predict and assess battery wear over time, with numerous battery models currently being investigated, such as energy-throughput and electrical models, which are appropriate for different needs.

Since batteries are the costliest components in electric vehicles, assessing or estimating

the wear V2G services could cause is an important step to determine its feasibility, both in technical and financial terms. However, the true impact of this higher number of cycling has not yet been precisely assessed, with studies addressing this issue applying different analysis methods and reaching different conclusions.

On the favorable side, Peterson, Apt, and Whitacre [44] concluded that V2G support using a PHEV battery causes approximately half the capacity loss compared to that associated with regular driving, being the depth of discharge not relevant in either case. Wang, Coignard, Zeng, *et al.* [45] reached a similar conclusion, estimating that the capacity losses from frequency regulation and peak load shaving, assuming an extreme scenario in which EVs would provide support services 2 hours every day for 10 years, only increase by 3.62% for frequency regulation and 5.6% for peak load shaving compared to a base case scenario in which EVs are only driven and charged uncontrolled. Wang, Coignard, Zeng, *et al.* [45] also considered a scenario in which EVs are only utilized to provide the V2G services occasionally. For that scenario the 10-year average capacity losses are 0.38%, 0.21% and 1.18% more than that of the base case, if EVs provide peak load shaving, frequency regulation and net load shaping services for 20 times per year. Kempton and Letendre [32] suggest that, even assuming unfavorable impacts on the EV battery life, electric-drive vehicles could serve as storage or generation for the electric supply system and generate revenue higher than the estimated cost to the owner.

An unfavorable result was found by Bishop, Axon, Bonilla, *et al.* [46], who claimed that providing ancillary or bulk energy services will incur a significant battery wear after performing simulations of lithium-ion cells in PHEVs and BEVs, leading to an approximately 57 times higher wear rate providing ancillary services when compared with regular driving and 115 times higher providing bulk energy services. This means that customers might have to replace the vehicle power-train annually, thus challenging the claim that V2G causes a lower battery capacity loss compared to driving. Dubarry, Devie, and McKenzie [47] reached an unfavorable result as well, corroborating that additional cycling by discharging vehicle batteries to the power grid shortens the vehicle lifetime.

Based on the results of these studies, it can be said authors have not been able to reach uniform conclusions regarding battery wear incurred by V2G operation, especially taking into

account the different analysis methods employed by the different authors, such as different modelling of V2G operation, battery chemistry and charging cycles. Despite the inconclusive results, it seems to be a consensus that using V2G as grid support will incur additional battery wear unless an additional optimization strategy is employed [48].

Impact of V2H on battery life has not yet been explored, with current research focused on developing solutions for issues such as seamless transition between grid-support (V2G) and grid-forming (V2H) modes, devising different topologies with lower harmonic distortions and power losses, or hypothesizing about V2H opportunities in the future, for example. Battery wear in a V2H scenario, due to the relatively rarity of power shortages and, in most cases, their short duration, is most likely lower compared to the V2G scenario, in which the battery might be constantly supporting the grid and as a result undergo a higher number of charge and discharge cycles.

The battery wear could be minimized by a number of optimization strategies that take into account each of the EV owners' needs, as well as other factors, such as their states of charge and different battery chemistry in the vehicles, a crucial factor determining battery wear as conclusion of the analysis led by Marongiu, Roscher, and Sauer [49]. An example of an optimization method was proposed by Uddin, Jackson, Widanage, *et al.* [50], who developed a smart-grid algorithm which reduces capacity fade in lithium-ion batteries by up to 9.1% and power fade by up to 12.1%. This algorithm could, allied with other advanced optimization techniques and grid-and-vehicle communications in a smart grid environment, further improve the V2G financial viability, on the expense of making V2G dependent on advances in other areas.

1.5 Objectives

- Simulation of a bidirectional single-phase power interface between an electric vehicle battery and the grid and test of the following features implemented in simulation and their respective control algorithms with MATLAB® and Simulink:
  - Battery-charging mode (G2V);
  - Grid-support mode (V2G);
  - Grid-forming mode (V2H);
- Validation and analysis of the employed control algorithms under different simulated test conditions, being these defined as it follows:
  - Grid fault: this test aims to assess the features of islanding detection and seamless transfer mode to grid-forming mode;
  - Grid reconnection: this test demonstrates the seamless transfer feature and grid re-synchronization capabilities of the system;
  - Continuous grid-connected operation: demonstrates the different system modes of operation while connected to an electric grid, including V2G and G2V operation modes with varying power references;
  - Transitions between grid-connected operation modes: displays the system capability of switching between V2G and G2V operation modes maintaining system stability;
- Experimental system validation and analysis with a real-time control interface (RTI) based on a dSPACE Controller Board in a Hardware-in-the-Loop (HiL) test platform.

1.6 Thesis structure

- Chapter 1: Introduction
  - Contains a contextualization of V2G and V2H technologies and their possible benefits, associated challenges and the thesis objectives.

- Chapter 2: State of the Art
  - Contains the literature review on bidirectional interfaces between electric vehicles and the energy supply grid.
- Chapter 3: Theoretical background
  - Contains a brief explanation on some theoretical concepts referred throughout the thesis, such as voltage-oriented control, reference frame transformations, proportional-integral-derivative control, grid connection requirements and passive unintentional islanding detection methods.
- Chapter 4: Methodology
  - Explains the proposed power structure and its relevant components, such as the battery, the bidirectional DC/DC and DC/AC converters, the output filter and the grid representation, as well as the control algorithms employed by the bidirectional DC/DC converter (BDC) and bidirectional DC/AC converter (BADC).
- Chapter 5: Simulation results
  - Contains the results obtained via simulation of the proposed power structure in MATLAB/Simulink®.
- Chapter 6: Experimental results
  - Contains the results obtained via physical implementation of the proposed power structure with a dSPACE-based real-time interface platform.
- Chapter 7: Analysis and Discussion
- Chapter 8: Conclusion

Chapter 2

Bidirectional Power Topologies and their Control

This chapter presents the state of the art of bidirectional power interfaces between electric vehicles and the grid, explaining the different topologies commonly used, as well as their respective control algorithms.

2.1 Power structures

Sharma and Sharma [51] provide a review of power structures commonly employed in V2G contexts, addressing and comparing different topologies of bidirectional inverters (BADCs) and bidirectional DC/DC converters (BDCs).

2.1.1 Bidirectional power structures

The typical structure used in V2G/G2V schemes to allow bidirectional power flow can be seen in Figure 2.1.

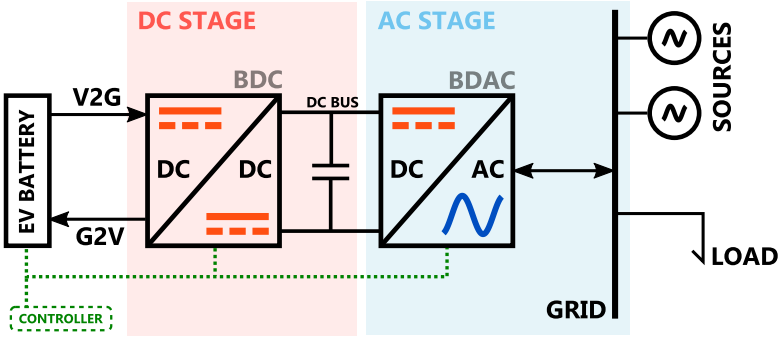

Figure 2.1: V2G using bidirectional converters (Source: [51]).

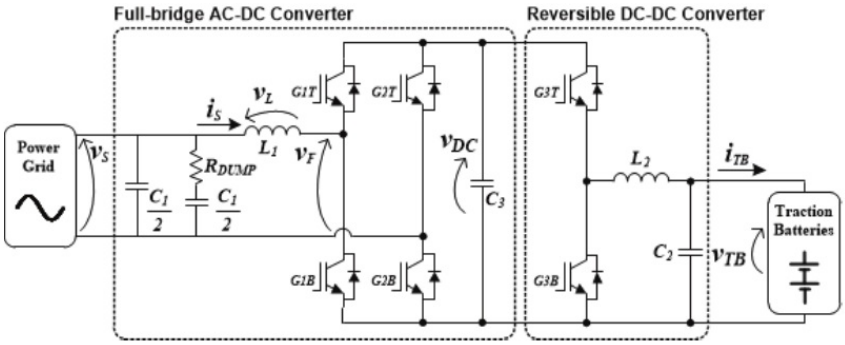

Figure 2.2: Typical full-bridge layout topology (Source: [52]).

According to Sharma and Sharma [51] the most commonly employed power topology in bidirectional systems for V2G purposes is the full-bridge layout (Figure 2.2), due to its circuit layout and flexibility in control. It also facilitates a third operating mode – V2H or Vehicle-to-Home.

Drawbacks of this structure include its bulkiness due to the number of necessary components, which also cause a higher cost and higher losses, thus making it less efficient [53]. Jang, Ciobotaru, and Agelidis [53] propose a compact single-phase bidirectional buck-boost-inverter topology to overcome these drawbacks, using a front-end buck-boost converter with an inductance to store energy between the DC and AC stages and only a capacitor filter in the output.

This dual-stage structure is explored and validated in the papers by Leite, Ferreira, and Batista [54], Pinto, Monteiro, Gonçalves, *et al.* [52], Vittorias, Metzger, Kunz, *et al.* [55], Zgheib, Al-Haddad, and Kamwa [56], all of them proposing a dual-stage bidirectional power structure for usage in V2G contexts, some of them validating the structure experimentally.

Concerning the DC/DC converter power topology, Leite, Ferreira, and Batista [54] use a half-bridge topology with 2 IGBTs as a DC/DC converter, operating either as a buck or as a boost converter. The same structure for the DC/DC is employed by Pinto, Monteiro, Gonçalves, *et al.* [52]. Zgheib, Al-Haddad, and Kamwa [56] on the other hand uses a more complex dual-active-bridge topology. Vittorias, Metzger, Kunz, *et al.* [55] do not show the bidirectional DC/DC topology, focusing on the DC/AC converter part and assuming the DC-side

voltage constant. A comparison of some common BDC topologies can be found in Table 2.1[1].

Table 2.1: Comparison of BDC topologies with respect to the number of components.

Topology	Capacitors	Inductors	Switches	Diodes	Employed in
Half-bridge	1	1	2	2	[54] [52]
Dual-active bridge	1	1 TF	8	2	[56]
Non-regulating half-bridge SRC	4	1 TF	4	4	[57] [58]
Bidirectional Ćuk	3	2	2	2	-

As evidenced by Table 2.1, the half-bridge topology is the simplest considering the number of passive elements and by using only two switches the control scheme is simplified, offering a fair compromise between efficiency and simplicity.

Recent research is focusing on developing a single-stage power processing system instead of the common dual-stage system, which is composed by a coupling between dedicated DC/DC (BDC) and DC/AC (BADC) converters. Other topologies for BADCs include the eight-switch, three-level, single-stage, and the matrix converter-based topologies [51]. Employing a single-stage power conversion might reduce energy losses and requires a reduced number of components and thus reduced costs. Concerning control methods resonant controllers are being used to reduce the current harmonics, as well as predictive algorithms and non-linear pulse-width modulations [59]. Another topology that can be employed involves inductive power transfer. This possibility was already investigated by Madawala and Thrimawithana [60] and Narula and Verma [61], enabling a contact-less power interface.

2.2 Control algorithms

In this section some of the control algorithms employed in relevant papers with similar bidirectional systems are listed and compared.

[1] A comparison between different BDC topologies with their respective details and features is shown on pages 350 and 351 in Sharma and Sharma' review on power electronics topologies in G2V / V2G contexts [51]

2.2.1 Bidirectional voltage-source inverter - BADC control algorithms

In the bidirectional interface by Leite, Ferreira, and Batista [54] the BADC is controlled via the voltage-oriented control applied in a single-phase system with emulation of a fictive axis and *dq* current control. The BADC is also responsible for maintaining the DC bus voltage constant in both G2V and V2G operation modes and also for defining the reactive power output determined externally.

Zgheib, Al-Haddad, and Kamwa [56] uses a similar control algorithm for the BADC, using however current controllers acting on the $\alpha\beta$ reference frame. The BADC in this paper is responsible for maintaining the DC bus voltage constant in both G2V and V2G operation modes while keeping reactive power output null. When battery is fully charged and there is no demand for power to be injected, the BADC can be controlled to act as an active power filter.

Vittorias, Metzger, Kunz, *et al.* [55] employ a space-vector modulation allied with $\alpha\beta$-*dq* reference frame transformations to the current components and power outputs similarly to [54] and [56]. In this paper the DC/DC converter is not shown and the DC link voltage is assumed constant.

Pinto, Monteiro, Gonçalves, *et al.* [52] use a predictive current control algorithm and in it the DC/AC converter operates as active rectifier with sinusoidal current and unitary power factor in G2V mode, and as an inverter with sinusoidal current and unitary power factor in V2G mode. A different characteristic in this control algorithm is the non-usage of reference frame transformations.

2.2.2 BDC control algorithms

In the bidirectional interface by Leite, Ferreira, and Batista [54] the BDC is controlled via a simple PWM and PI controller. In V2G mode the BDC acts as a boost converter and the battery current is controlled by a PI controller, which generates the BDC control signal and regulates the pulse-width modulation to reach the defined active power set-point. In G2V mode the BDC acts as buck converter and the battery is charged in a three-stage charging sequence,

defined by the battery manufacturer.

Zgheib, Al-Haddad, and Kamwa [56] proposes a dual-active bridge topology controlled by phase-shift modulation, allowing the bidirectional charger to be used not only in EV applications and in PHEV applications, due to this control technique being able to deal with a higher variety of battery voltages. In this paper the BDC is controlled to follow a CC/CV battery charging algorithm.

Pinto, Monteiro, Gonçalves, *et al.* [52] use a BDC control algorithm similar to that used by Leite, Ferreira, and Batista [54]. In V2G mode the BDC acts as a boost converter and in G2V mode as a buck converter, following a CC/CV charging pattern as well. Additionally to G2V and V2G modes, Pinto, Monteiro, Gonçalves, *et al.* present a V2H mode, in which the BDC is responsible for maintaining the DC link voltage constant.

Another approach is using a non-regulating half-bridge series resonant converter, effectively turning the BDC into a DC transformer. This control method is employed by Kwon, Jung, and Choi [58].

2.2.3 Vehicle as temporary energy supplier (V2H)

Due to the complexity of such a system there is a limited number of papers dealing with this possibility. Some authors have developed bidirectional systems with this feature. Pinto, Monteiro, Gonçalves, *et al.* [52] for example devised a system with V2H capabilities. They do not, however, mention how the transition between these modes of operation is performed.

Vittorias, Metzger, Kunz, *et al.* [55] propose a dual-stage power system capable of operating in three different modes, G2V, V2G and V2H. A technique for re-synchronization with the grid is shown, using an additional PI controller controlling the output phase with large time constants to prevent large transients during the transition.

Kwon, Jung, and Choi [58] present an isolated bi-directional EV charger and its control methods for V2G and V2H. Their structure allows for smooth transitions between operation modes due to all control algorithms being related with the BADC, since the BDC is a non-regulating series resonant converter.

Chapter 3

Modelling and Control of Grid Interfaces

This chapter presents relevant theoretical background concepts that are important for understanding how a grid interface is modelled and controlled.

3.1 Inverters

Inverters are devices that convert a direct current source (DC) into an alternating current (AC) source. Modern inverters are made of electronic switches (IGBTs, IGCTs) that are switched on and off at high frequencies, at specific times and in a given sequence, generating an alternating current output.

Inverters can be divided into different categories, depending on their structure, number of output levels, usage of a transformer, nominal power and other aspects. A common high-level categorization is dividing inverters into the following three categories: voltage-source inverters (VSIs), current-source inverters (CSIs) and impedance-source inverters (ZSIs) [62]. Among these options, VSIs are the most commonly employed [63].

In VSI configurations the DC stage voltage is maintained constant regardless of the current drained by the inverter, which can be achieved by controlled rectifiers, a battery or DC/DC converters. The typical structure of a VSI can be seen in Figure 3.1.

3.2 Reference frame transformations for AC systems modelling

In this section the transformations of reference frames, that is, the Clarke and Park transformations, are explained in greater detail. These transformations are used in the voltage-oriented control algorithm to extract continuous DC-like components of the grid voltage and currents.

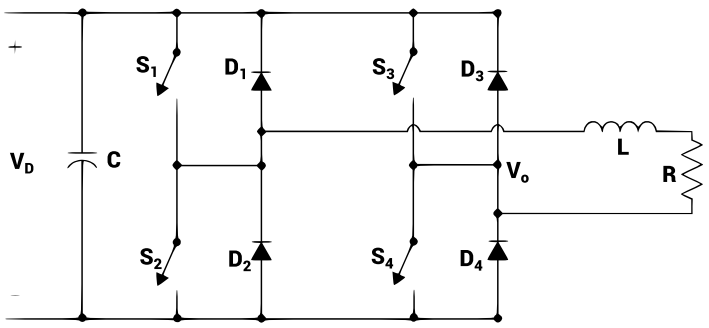

Figure 3.1: Typical single-phase VSI configuration.

3.2.1 Clarke Transformation

The Clarke Transformation, also called $\alpha\beta\gamma$ Transformation, is a mathematical transformation envisioned by Edith Clarke in 1951 [64] that can be used to facilitate the analysis of three-phase systems. By applying the Clarke Transformation to a balanced system of three phases a, b and c, the result is a set of three orthogonal components, i_α, i_β and the zero component i_γ. The horizontal axis is called α-axis and the vertical axis called β-axis. As long as the three-phase system is balanced, the component i_γ has zero value. In simpler terms the Clarke transformation is the decomposition of a three-phase system in a two-phase system.

Equation (3.1) describes the power variant Clarke Transformation [64],

$$i_{\alpha\beta\gamma}(t) = T\ i_{\text{abc}}(t) = \frac{2}{3}\begin{bmatrix} 1 & -\frac{1}{2} & -\frac{1}{2} \\ 0 & \frac{\sqrt{3}}{2} & -\frac{\sqrt{3}}{2} \\ \frac{1}{2} & \frac{1}{2} & \frac{1}{2} \end{bmatrix}\begin{bmatrix} i_{\text{a}}(t) \\ i_{\text{b}}(t) \\ i_{\text{c}}(t) \end{bmatrix} \tag{3.1}$$

where $i_{\alpha\beta\gamma}$ is the set of resulting components in the α and β-axis, T is the transformation matrix and i_{abc} is the set of phasors of a three-phase system, the i_{a}, i_{b} and i_{c} phasors.

The inverse Clarke transformation can be calculated using the Equation (3.2) and, by applying it to a set of phasors in the $\alpha\beta\gamma$ reference frame, the original phasors in the *abc* sequence can be recovered.

$$i_{\text{abc}}(t) = T^{-1}\, i_{\alpha\beta\gamma}(t) = \begin{bmatrix} 1 & 0 & 1 \\ -\frac{1}{2} & \frac{\sqrt{3}}{2} & 1 \\ -\frac{1}{2} & -\frac{\sqrt{3}}{2} & 1 \end{bmatrix} \begin{bmatrix} i_\alpha(t) \\ i_\beta(t) \\ i_\gamma(t) \end{bmatrix}. \tag{3.2}$$

Figure 3.2 contains a graphical example of the Clarke Transformation. Figure 3.2a shows a three-phase positive-sequence current system composed by phasors i_a, i_b and i_c and Figure 3.2b represents the resulting phasors, i_α and i_β, in the $\alpha\beta\gamma$ reference frame.

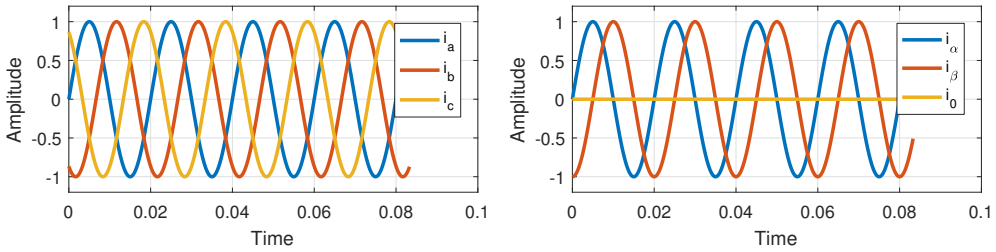

(a) Currents in the *abc* reference **(b)** Currents in the $\alpha\beta\gamma$ reference

Figure 3.2: Graphical example of Clarke Transformation.

Since the three-phase system in Figure 3.2a is balanced, the i_γ, the zero component, has null value in Figure 3.2b. In the *abc* system the phase difference between the phases is 120 degrees, while in the $\alpha\beta\gamma$ system the components phasors are orthogonal, that is, the phase difference between them is 90 degrees, as represented in Figure 3.3, which contains an explanation of the Clarke Transformation with phasor diagrams.

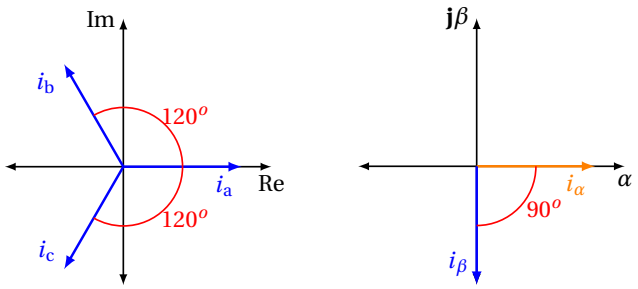

(a) Balanced phasors of a 3-phase *abc* system **(b)** Components after Clarke Transformation

Figure 3.3: Graphical example of Clarke Transformation with phasors.

3.2.2 Park Transformation

The Park Transformation, similarly to the Clarke Transformation, is a mathematical transformation that can be used to ease analysis of three-phase systems. It was first proposed by Robert H. Park in 1929 [65], who defended it as a method to calculate current, power and torque in salient and non-salient poles synchronous machines. Although first developed for synchronous machine analysis, the Park Transformation has since then been used extensively in other areas, such as in power electronics control and asynchronous machines analysis.

Unlike the Clarke Transformation in which phasors are projected onto a stationary reference frame, the Park Transformation proposes the projection of phasors onto a rotating reference frame, denominated *dq*. By doing so, it essentially converts periodic signals into DC quantities if the angular velocity of rotation of the *dq*-frame matches that of the periodic signal used as input. A graphical example can be seen in Figure 3.4, where the Park Transformation is applied to a balanced positive-sequence three-phase system, yielding the *dq0* components as represented in Figure 3.4b.

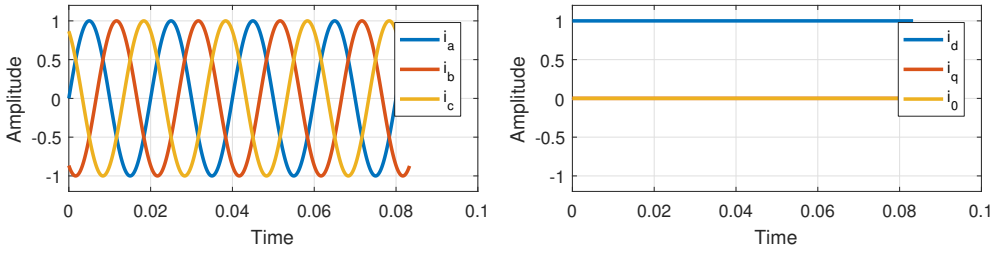

(a) Currents in the *abc* reference **(b)** Currents in the *dq0* reference

Figure 3.4: Graphical example of Park Transformation.

The power invariant Park Transformation is described in Equation (3.3),

$$i_{\mathrm{dq0}} = \sqrt{\frac{2}{3}} \begin{bmatrix} \cos(\theta) & \cos\left(\theta - \frac{2\pi}{3}\right) & \cos\left(\theta + \frac{2\pi}{3}\right) \\ -\sin(\theta) & -\sin\left(\theta - \frac{2\pi}{3}\right) & -\sin\left(\theta + \frac{2\pi}{3}\right) \\ \frac{\sqrt{2}}{2} & \frac{\sqrt{2}}{2} & \frac{\sqrt{2}}{2} \end{bmatrix} \begin{bmatrix} i_{\mathrm{a}}(t) \\ i_{\mathrm{b}}(t) \\ i_{\mathrm{c}}(t) \end{bmatrix} \tag{3.3}$$

where i_{dq0} is the resulting set of phasors in the rotating *dq0* reference frame, i_a, i_b and i_c the phases of a three-phase *abc*-sequence system and θ the angular displacement of the

rotating *dq0* frame in relation to the α-axis in the Clarke Transformation reference frame ($\alpha\beta\gamma$) as seen in Figure 3.3b. The Park Transformation is the successive employment of two transformations, the Clarke transformation and the reference frame transformation, allowing the direct extraction of the *dq* components from an balanced three-phase *abc*-sequence system.

The inverse Park Transformation is described in Equation (3.4). The transformation matrix in this case is the transposed transformation matrix of the Park Transformation in Equation (3.3).

$$i_{\text{abc}} = \sqrt{\frac{2}{3}} \begin{bmatrix} \cos(\theta) & -\sin(\theta) & \frac{\sqrt{2}}{2} \\ \cos\left(\theta - \frac{2\pi}{3}\right) & -\sin\left(\theta - \frac{2\pi}{3}\right) & \frac{\sqrt{2}}{2} \\ \cos\left(\theta + \frac{2\pi}{3}\right) & -\sin\left(\theta + \frac{2\pi}{3}\right) & \frac{\sqrt{2}}{2} \end{bmatrix} \begin{bmatrix} i_{\text{d}}(t) \\ i_{\text{q}}(t) \\ i_0(t) \end{bmatrix} \tag{3.4}$$

3.3 Proportional-Integral-Derivative Control

Proportional-Integral-Derivative Control (PID) refers to a control method widely employed in several applications, due to its ease of use, relatively low complexity and robustness, if its parameters are tuned correctly [66]. It is named after its three components, also called correcting terms, the proportional, integral and derivative components. Each of these components acts in a different way to eliminate the distance, that is, the error, between the measured value and a desired value for a process variable. The desired value is also called the set-point of the controller, while the controller output is called the control variable. The usefulness of PID controls lies in their general applicability, especially in cases where the mathematical model of the plant is not known and thus analytic design methods are not practical, PID controls prove to be most useful [67].

The basic structure of a PID controller can be seen in Figure 3.5, where $r(t)$ is the set-point, $u(t)$ the controller output or control variable and $y(t)$ the measured value, or feedback signal. The PID components act on the error signal $e(t)$ and their outputs are summed to produce the control variable control signal, that acts on a plant, process or system. A system variable can be measured and used as a feedback signal acquired from the plant, which is compared with the set-point to produce the error signal.

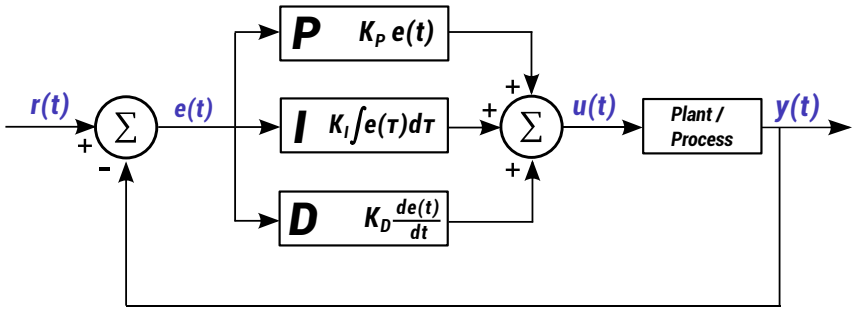

Figure 3.5: PID Controller block diagram in a parallel topology.

The proportional component determines how fast the response of the controller will be once a difference between the set-point and control variable is detected. In mathematical terms it is simply a constant, the proportional gain, multiplied by the calculated error. Setting high values of proportional gain causes a faster dynamic response, the system may however become unstable. The proportional component alone cannot fully eliminate the steady-state error. Solving that problem requires an integral component.

Unlike the proportional component, which is only proportional to the error calculated in real time, the integral component produces an output proportional to the error integrated over time. This component eliminates the steady-state error and will also correspond to a faster rise time but larger settling time [68]. One of its major drawbacks is evident in practical applications, where, for example, the output of the controller is limited and unable to properly control the desired variable. In those cases, saturation of the integral component might occur, and thus, even though the error might be small, due to the accumulated error the controller output deviates from the set-point. This issue can be overcome with a anti-windup integrator, that is, one with a limit for the integration and a integral reset function [68].

The derivative component does not act on the value of the error itself, rather on its rate of change at the instant. The derivative component will produce an output proportional to that change, and, in practical terms, will alter the output more aggressively in case the error rate of change is higher. This component prevents or dampens overshooting, thus making the controller output smoother. One of its drawbacks is the sensitivity to high-frequency signals, such as white noise, since the derivative of those signals will have a high amplitude and interfere with the control output.

Equation (3.5) contains a mathematical formulation of a traditional PID control in a parallel topology in continuous-time domain. The term $u(t)$ represents the controller output over time.

$$u(t) = K_{\mathrm{p}} e(t) + K_{\mathrm{i}} \int_0^t e(t')\,dt' + K_{\mathrm{d}} \frac{de(t)}{dt} \tag{3.5}$$

Other terms are defined as it follows:

- K_{p} - proportional gain;
- K_{i} - integral gain;
- K_{d} - derivative gain;
- $e(t)$ - error calculated over time, representing the distance between the variable measured value and its desired value;
- t - instantaneous time;
- t' - variable of integration (takes on values from time 0 to the present time).

Employing a PID controller in software or in microcontrollers requires a discrete PID equation, since microcontrollers operate with a definite frequency - thus limiting a measurement sampling frequency, for example - and discrete variables. A generic mathematical expression for a discrete PID controller is found in Equation (3.6) by simply converting Equation (3.5) to its discrete counterpart, although there are other more complex formulations in literature.

$$u(t_k) = K_p e(t_k) + T_i^{-1} e(t_k) \left(\frac{T_s}{z-1}\right) + T_d \left(\frac{e(t_k) - e(t_{k-1})}{T_s}\right)\left(\frac{z+1}{T_s\, z}\right) \tag{3.6}$$

The parameters T_i and T_d are discrete counterparts of the K_i and K_d parameters in the continuous-time PID equation. They represent the integrator time and derivative time, respectively.

3.4 Voltage-Oriented Control

Voltage-Oriented Control (VOC) is a control method for switched-mode power processors, such as buck-and-boost converters and inverters, that is based on the Field-Oriented Control

(FOC) employed in the control of three-phase AC-motor drives. It is classified as a vector control method because it deals with vector quantities, unlike the scalar control methods to regulate speed in induction motors, for example. Voltage-Oriented Control uses a synchronous reference frame, the *dq* frame, with the *dq* axes rotating with the same angular velocity ω_g of the grid voltage and with the *d* axis aligned with the grid voltage phasor. By doing so, the quadrature component of the grid voltage remains null and, consequently, active and reactive powers can be controlled separately by controlling, respectively, the *d* (grid aligned) and *q* components of the grid current, as shown in Figure 3.6.

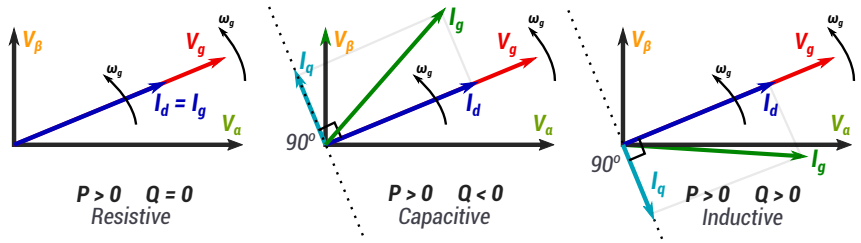

Figure 3.6: Phasor diagrams showing how i_d remains aligned with the grid voltage phasor and thus is related to active power, while i_q is perpendicular to i_d and therefore is related to reactive power control.

Apparent power can be calculated with Equation (3.7). It corresponds to the multiplication of a voltage phasor and the complex conjugate of a current phasor.

$$S = VI^* \tag{3.7}$$

Since the output voltage in a grid-tried inverter is the grid voltage and this voltage can be assumed constant in terms of RMS value V_g and frequency ω_g. If the grid voltage is used as a reference, apparent power becomes

$$P = V_g I_g \tag{3.8}$$

but active power depends on the phase difference between the grid voltage and grid current, as in

$$P = V_g I_g \cos(\theta_{\Delta VI}) \tag{3.9}$$

where I_g is the output current RMS value and $\theta_{\Delta VI}$ is the phase difference between the grid voltage and grid current. Equation (3.8) thus shows that the active power output is effectively

controlled by the phase difference between the current output and grid voltage. Reactive power output depends too on the phase difference, but inversely proportional, that is, if the phase difference is zero, so is the reactive power.

In VOC two phasor transformations are necessary, being them the Clarke and the Park transformations[1]. These transformations will be responsible for converting signals, voltages and currents, to their respective components in the $\alpha\beta$ or dq reference frames.

This allows these signals to be controlled with traditional PI controllers, for example. By controlling the dq-components of the output current, it is possible to control the phase difference between the current and the grid voltage. The current d components is related to the active power and the current q component related to the reactive power, as evidenced in Equation (3.8).

If a single-phase frequency inverter is used there is no three-phase voltage system to be used as grid reference and therefore obtaining the grid dq components requires emulation of a two-axis reference frame by applying a ninety-degree shift to the grid current I_G and grid voltage V_G signals, thus obtaining orthogonal components in the $\alpha\beta$ reference frame, I_{G_α}, I_{G_β}, V_{G_α} and V_{G_β}. The emulation is equivalent to creating an imaginary single-phase inverter circuit connected in parallel to the real one [69] [70], the virtual one generating an alternating current waveform 90^o delayed in relation to the real circuit output. A representation of this concept can be found in Figure 3.7, which shows the connection of the VSI to the grid represented by the alternating current sources V_{G_α} and V_{G_β}.

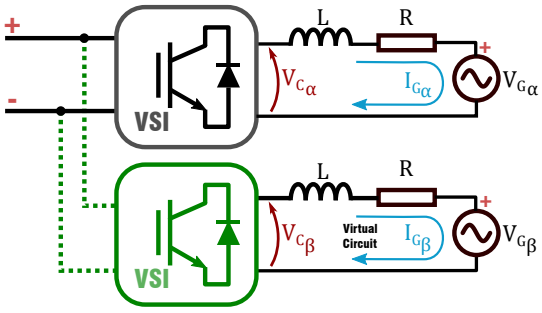

Figure 3.7: Virtual parallel-connected inverter circuit to model voltage-oriented control.

[1]These transformations are explained with further detail in Subsections 3.2.1 and 3.2.2.

Voltages and currents can be expressed in terms of their α and β components using complex numbers, as in Equation (3.10)

$$\begin{cases} \underline{V}_{\alpha\beta} & = V_\alpha + \mathbf{j}V_\beta \\ \underline{I}_{\alpha\beta} & = I_\alpha + \mathbf{j}I_\beta \end{cases} \tag{3.10}$$

and, applying the Kirchhoff's law to the circuit presented in Figure 3.7, the Equation (3.11) is obtained.

$$\underline{V}_{C_{\alpha\beta}} = \underline{I}_{G_{\alpha\beta}} R + \frac{L\, d\, \underline{I}_{G_{\alpha\beta}}}{dt} + \underline{V}_{G_{\alpha\beta}} \tag{3.11}$$

Using the Park Transformation it is possible to convert the components in Equation (3.11), projected onto the stationary $\alpha\beta$ reference frame, to the dq reference frame rotating with angular frequency ω_g, equal to the angular frequency of the grid. To accomplish that a phase shift in polar coordinates can be applied, as represented in Equation (3.12).

$$\underline{x}_{\alpha\beta} = \underline{x}_{\mathrm{dq}}\, e^{\mathbf{j}\omega_g t} \tag{3.12}$$

where $\underline{x}_{\alpha\beta}$ is a given phasor already in the $\alpha\beta$ reference frame. Therefore, using Equation (3.12) to replace the phasors in the $\alpha\beta$ reference frame in Equation (3.11) Equation (3.13) is obtained

$$\frac{L\, d\left(\underline{I}_{G_{\mathrm{dq}}}\, e^{\mathbf{j}\omega_g t}\right)}{dt} + R\underline{I}_{G_{\mathrm{dq}}}\, e^{\mathbf{j}\omega_g t} = \underline{V}_{C_{\mathrm{dq}}} e^{\mathbf{j}\omega_g t} - \underline{V}_{G_{\mathrm{dq}}} e^{\mathbf{j}\omega_g t} \tag{3.13}$$

and, to simplify it even further, decomposing the derivative of the grid current using the product rule results in Equation (3.14),

$$L\left(\frac{d\underline{I}_{G_{\mathrm{dq}}}}{dt} e^{\mathbf{j}\omega_g t} + \mathbf{j}\omega_g \underline{I}_{G_{\mathrm{dq}}} e^{\mathbf{j}\omega_g t}\right) + R\underline{I}_{G_{\mathrm{dq}}}\, e^{\mathbf{j}\omega_g t} = \underline{V}_{C_{\mathrm{dq}}} e^{\mathbf{j}\omega_g t} - \underline{V}_{G_{\mathrm{dq}}} e^{\mathbf{j}\omega_g t} \tag{3.14}$$

dividing the two sides of the Equation (3.14) by $e^{\mathbf{j}\omega_g t}$ we get Equation (3.15),

$$L\left(\frac{d\underline{I}_{G_{\mathrm{dq}}}}{dt} + \mathbf{j}\omega_g \underline{I}_{G_{\mathrm{dq}}}\right) + R\underline{I}_{G_{\mathrm{dq}}} = \underline{V}_{C_{\mathrm{dq}}} - \underline{V}_{G_{\mathrm{dq}}} \tag{3.15}$$

expanding it and replacing the *dq* components by their real and imaginary parts, similar to Equation (3.10),

$$L\frac{d\left(I_{G_\mathrm{d}}+\mathbf{j}I_{G_\mathrm{q}}\right)}{dt}+\mathbf{j}L\omega_g\left(I_{G_\mathrm{d}}+\mathbf{j}I_{G_\mathrm{q}}\right)+R\left(I_{G_\mathrm{d}}+\mathbf{j}I_{G_\mathrm{q}}\right)=V_{C_\mathrm{d}}+\mathbf{j}V_{C_\mathrm{q}}-V_{G_\mathrm{d}}-\mathbf{j}V_{G_\mathrm{q}} \tag{3.16}$$

this way, it is possible to organize a system of equations as represented in Equation (3.17) by separating the real and imaginary terms of Equation (3.16).

$$\begin{cases} V_{C_\mathrm{d}}=L\dfrac{dI_{G_\mathrm{d}}}{dt}+RI_{G_\mathrm{d}}-\omega_g LI_{G_\mathrm{q}}+V_{G_\mathrm{d}} \\ V_{C_\mathrm{q}}=L\dfrac{dI_{G_\mathrm{q}}}{dt}+RI_{G_\mathrm{q}}+\omega_g LI_{G_\mathrm{d}}+V_{G_\mathrm{q}} \end{cases} \tag{3.17}$$

Another simplification is possible. Assuming

$$\begin{cases} V_{C_\mathrm{d}}=V'_\mathrm{d}-\omega_g LI_{G_\mathrm{q}}+V_{G_\mathrm{d}} \\ V_{C_\mathrm{q}}=V'_\mathrm{q}+\omega_g LI_{G_\mathrm{d}}+V_{G_\mathrm{q}} \end{cases} \tag{3.18}$$

where V'_d and V'_q represent, respectively,

$$\begin{cases} V'_\mathrm{d}=L\dfrac{dI_{G_\mathrm{d}}}{dt}+RI_{G_\mathrm{d}} \\ V'_\mathrm{q}=L\dfrac{dI_{G_\mathrm{q}}}{dt}+RI_{G_\mathrm{q}} \end{cases} \tag{3.19}$$

by applying the Laplace transformation and performing some algebraic manipulations it is possible to obtain Equation (3.20)

$$\begin{cases} I'_\mathrm{d}=\dfrac{V'_\mathrm{d}}{R+sL} \\ I'_\mathrm{q}=\dfrac{V'_\mathrm{q}}{R+sL} \end{cases} \tag{3.20}$$

and thus, by using a PI controller cascaded with the obtained electrical system transfer

function $(R + sL)^{-1}$, a mathematical description of the entire system is obtained.

Instantaneous power values can be calculated using *pq*-theory in the *dq* reference frame. Instantaneous active power is calculated using Equation (3.21) and the reactive power using Equation (3.22).

$$P = \frac{V_d i_d}{2} \tag{3.21}$$

$$Q = -\frac{V_d i_q}{2} \tag{3.22}$$

3.5 Grid connection requirements

Commercial solar or wind energy inverters have to fulfill the grid requirements to establish a connection and provide power to the grid they are connected to. As defined in the

- *IEEE 1547 - 2018,* "*Standard for Interconnection and Interoperability of Distributed Energy Resources with Associated Electric Power Systems Interfaces*" [71];
- *IEC 61727 - 2004,* "*Characteristics of the utility interface*" [72]

bidirectional V2G interfaces have to comply to these requirements as well [73] and have to be tested according to the definitions found in the IEC 62116 - 2014 "*Standard for Testing Procedure of Islanding Prevention Measures for Grid Connected Photovoltaic Power Generation Systems*" [74] European norm, for example. These requirements can be summarized as follows:

- DC Current Injection;
  - *IEEE 1547* - $I_{\mathrm{DC}} < 0{,}5\%$ of the rated RMS current;
  - *IEC 61727* - $I_{\mathrm{DC}} < 1\%$ of the rated RMS current.
- Harmonics - The total rated-current distortion of the inverter under normal operating conditions must be under the limit defined in the norms.
  - *IEEE 1547* - maximum current distortion for harmonics below the 11^{th} order is 4%;
  - *IEC 61727* - same limits as in IEEE 1547.

- Utility Synchronization and Seamless Transfer Capability - the interface must be synchronized with the grid and, in the case of grid failure, must be able to change between states of operation seamlessly (reconnection, ride-through, etc) and causing minimal system transients;
  - *IEEE 1547* - no time delay for reconnection after tripping. The voltage and frequency must be within the allowed range, respectively $0,88 < V < 1,10$ pu and $59,3 < f < 60.5$ Hz;
  - *IEC 61727* - minimum time delay of 3 minutes before reconnection and voltage and frequency within allowed range, respectively $0,85 < V < 1,10$ pu and $f_n - 1 < f < f_n + 1$ (Hz), thus between 49 Hz and 51 Hz.
- Response to Abnormal Voltages (see Table 3.1);
- Response to Abnormal Frequencies (see Table 3.2);
- Unintentional Islanding;
  - *IEEE 1547* - islanding conditions must be detected within 2 seconds;
  - *IEC 61727* - same requirements as IEEE 1547.
- Short Circuit Test.

Tables 3.1 and 3.2 show the disconnection times for voltage and frequency variations according to the IEEE and IEC norms.

Table 3.1: Disconnection time for voltage variations (Extracted from [59])

IEEE 1547		IEC 61727	
Voltage range (pu)	Disconnection time	Voltage range (pu)	Disconnection time
V < 0,5	0,16 s	V < 0,5	0,10 s
0,5 ≤ V < 0,88	2,00 s	0,5 ≤ V < 0,85	2,00 s
1,1 ≤ V < 1,2	1,00 s	1,10 ≤ V < 1,35	2,00 s
V ≥ 1,2	0,16 s	V ≥ 1,35	0,05 s

Table 3.2: Disconnection time for frequency variations (Extracted from [59])

IEEE 1547		IEC 61727	
Frequency range (Hz)	Disconnection time	Frequency range (Hz)	Disconnection time
$59{,}3 < f < 60{,}5$	0,16 s	$f_n - 1 < f < f_n + 1$	0,10 s

3.6 Unintentional islanding detection methods

Unintentional islanding refers to a scenario in which the utility grid is suddenly disconnected following normal operation, resulting in so-called islands of distributed generation units independently trying to maintain grids in smaller scale. Islanding conditions may damage distributed generation units in cases where the load in a microgrid cannot be matched, or after grid reconnection, since the generators might be out of synchronization in relation to the grid, leading to high inrush and peak currents [75].

Methods for detecting islanding can be categorized in passive and active methods. Active methods uses small perturbations in the inverter output and observes the system behaviour in order to determine if the situation configures an islanding condition. While active methods are complex and rely on altering the inverter output parameters, passive methods on the other hand are cheaper and simpler to implement and are usually based solely on detection of a change or rate-of-change in a power system parameter. The voltage, frequency or harmonics, in the event of loss of grid references, will suffer variations most fault situations [75].

Passive methods have limitations, one example is the non-detection zone, that is, the range of values for which an islanding condition is not detected. In cases where the power supplied by a grid into a microgrid is very small, the disturbance created due to grid disconnection is very small as well [76]. According to Zhihong Ye, Kolwalkar, Yu Zhang, *et al.* [77], these passive detection schemes possess a large non-detection zone, allowing nearly 6% reactive power mismatch and 29% active power mismatch.

Due to the low cost and simplicity, these passive methods will be explained with further details based on the report published by Bower and Ropp [78] and the paper by Noor,

Arumugam, and Vaziri [75].

Grid-connected inverters are required to have over and under-frequency protection methods and over- and under-voltage protection methods. Crossing the thresholds for those values cause the inverter to stop supplying power to the utility grid. These protection methods protect consumers' equipment but also serve as anti-islanding detection methods.

Frequency relays are responsible for being activated once the frequency is not within a certain range, which is between 59,5 Hz and 60,5 Hz for 60 Hz systems corresponding to a tolerance of 0,83% which would be equivalent to a range between 49,59 Hz and 50,41 Hz for 50 Hz systems. Other relays are activated depending on the rate of change of the frequency, being called Rate of Change of Frequency Relay (ROCOF). These relays are normally configured in 60 Hz systems to trip when the frequency rate of change reaches values between 0.10 Hz/s and 1.20 Hz/s [75].

The behaviour of the system after a grid disconnection occurs depends on the active and reactive powers being delivered at the moment of the fault. If the active power is not null, the output voltage increases and thus the over-voltage protection can act to prevent damages. In a scenario where the reactive power is not null, there will be a change in the output frequency, which can also be detected by an over-and-under-frequency protection system [78].

Phase jump detection involves the detection of a sudden change between the phase difference of the inverter's terminal voltage and its output current. As a passive method, phase jump detection does not affect the output power quality of the inverter and does not impact system transient response [78].

Chapter 4

Proposed Power Topology and Control Algorithms

This chapter contains the proposed power structure and explains its relevant components, the battery, the bidirectional DC/DC and DC/AC converters, the output filter, the grid, and the control algorithms employed by the DC/DC and DC/AC converters. In this chapter the simulation and experimental methods are also described.

4.1 Power structure

The power structure chosen to accomplish the integration of an electrical vehicle with the electric grid is composed of five parts, these being

- Vehicle, represented as a battery;
- Bidirectional DC/DC converter (BDC);
- Bidirectional single-phase voltage-source inverter (VSI or BADC);
- Output filter;
- Grid and common-coupling point (CPP).

A simplified block diagram of the proposed power structure can be seen in Figure 4.1. The connection lines between the blocks represent the bidirectional nature of the power flow in the system.

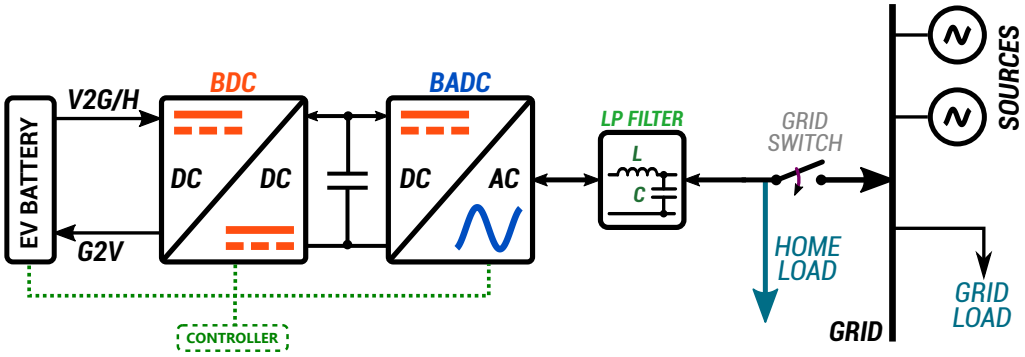

Figure 4.1: General overview of the proposed power structure

An electrical diagram of the power structure represented in Figure 4.1 is pictured with greater detail in Figure 4.2.

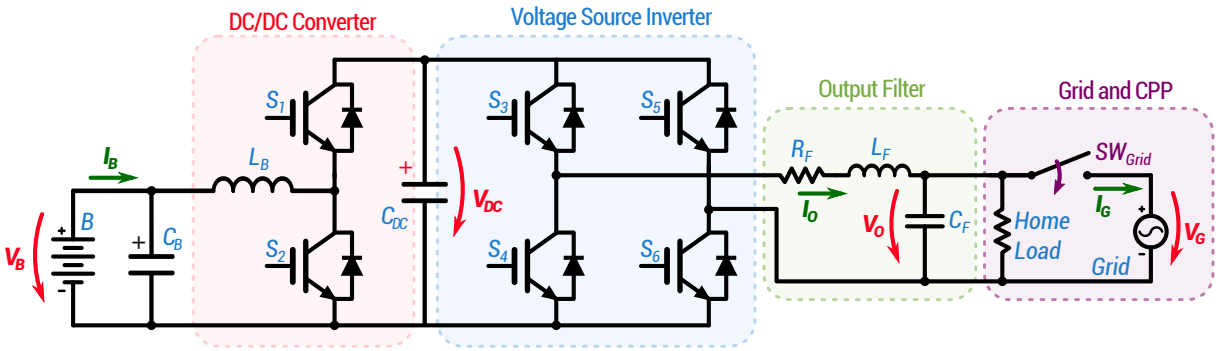

Figure 4.2: Power structure electrical schematic

The following subsections contain further explanations about the five components of the aforementioned power topology.

4.1.1 Battery

The battery is a representation of the electric vehicle. As aforementioned, EV batteries are lithium-ion batteries with voltages ranging from 200 to 800 V in the Porsche Taycan to be released in 2019. Given their usually high prices, in this thesis a lead-acid battery is used instead, since these batteries are readily available and allows for simpler experimental validation of the proposed power structure.

4.1.2 Bidirectional DC/DC converter

The bidirectional DC/DC converter (BDC) is a buck-boost converter that alternates between two modes of operation, step-down and step-up modes, to respectively charge (G2V) and discharge the battery (V2G and V2H). It consists of one of the three legs of a three-phase voltage source inverter, as represented in the red box in Figure 4.2, where the IGBT switches S_1 and S_2 control the power flux of the DC/DC converter. The other four switches represent the single-phase voltage source inverter connected to the grid and controlled separately as described in subsection 4.1.3. The capacitor C_{DC} stores energy and acts as a voltage-based (V_{DC}) energy buffer between the two stages.

4.1.3 Bidirectional single-phase voltage source inverter

The bidirectional single-phase frequency inverter (BADC) is a full-bridge inverter with IGBTs and free-wheel diodes and it is shown in the light-blue box in Figure 4.2. It is made of two legs of a three-phase inverter. It contains the electronic switches S_3, S_4, S_5 e S_6 and it is controlled by the voltage-oriented control algorithm, which is further explained in Section 4.2.

4.1.4 Output filter

The output filter is a low-pass LC filter, used to improve the inverter current output waveform and reduce the higher-order harmonics. In the simulation the capacitance and inductance values were chosen to reproduce the experimental values, enabling the simulation of real-world conditions and therefore allowing for testing of different behaviours and faster parameter adjusts, for example the proportional and integrative gains of the PI controllers.

Concerning the experimental setup, the filter values were chosen by trial and error, observing the output current waveform. Other filter topologies that might produce better results can be used, such as LCL [79]. Therefore the filter topology is subject to further tests and optimization, but not the main research focus of this thesis.

4.1.5 Grid and common-coupling point (CPP)

The grid is represented by an AC source with capability of exchanging any given amount of active and reactive power, thus acting as an infinite bus. In practical terms, it is the internal microgrid installed in the LSE laboratory of the IPB for educational and research purposes.

The common-coupling point represents where home loads can be connected to and the point which, after a grid fault condition is detected, remains energized in case the V2H feature is enabled.

4.2 Control algorithms

The power structure is controlled by two control algorithms, the BDC and BADC control algorithms. An overview of the power structure along with the respective control blocks can be seen in Figure 4.3.

The BDC control algorithm is responsible for determining whether the BDC will operate as a buck (G2V) or a boost (V2G) converter to respectively charge and discharge the battery. While operating as a buck converter in G2V mode, the BDC control algorithm controls the battery charging mode following a CC/CV battery charging algorithm. While operating as a boost converter in V2G or V2H mode, the BDC control algorithm is responsible for maintaining the DC link voltage constant.

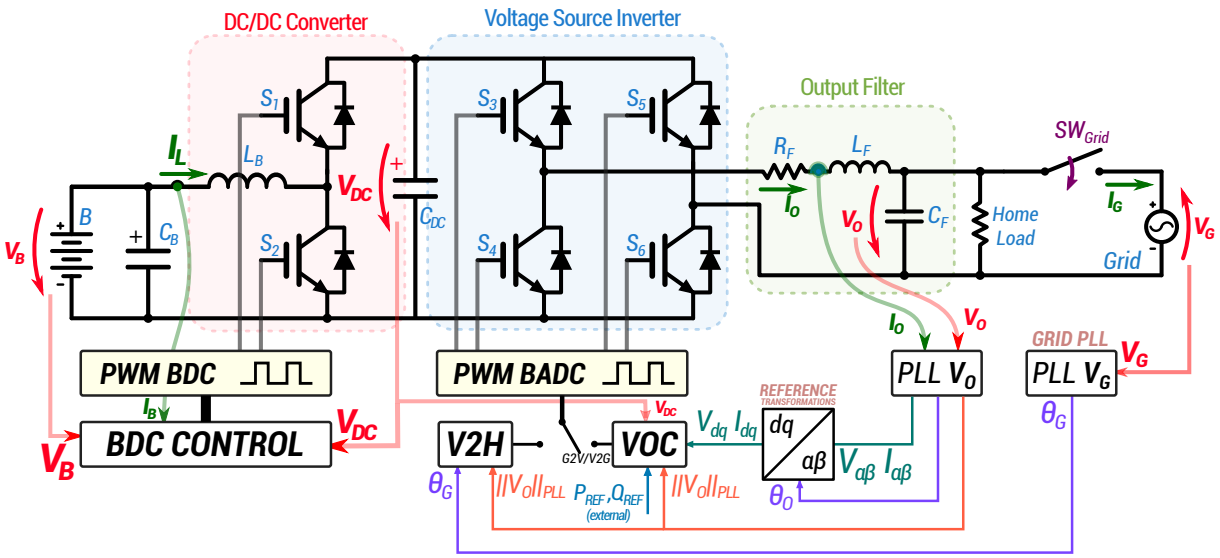

Figure 4.3: Power and control structure.

The BADC control algorithm in buck mode (G2V) is responsible for maintaining the DC link voltage constant. In V2G mode it controls the active and reactive power exchange with the grid, while in V2H mode it maintains the output voltage at a fixed reference voltage set point. Table 4.1 contains a summary of the system operation modes and the control targets of the BDC and BADC under them.

The transition between different modes of operation is performed by a high-hierarchy logical control and can be represented by a flowchart as displayed in Figure 4.4.

Table 4.1: Summary of system operation modes and the respective control targets of the DC/DC and DC/AC converters.

Operation modes			Control target	
Mode	Grid connected	Battery	BDC	BADC
G2V	Yes	Charging	CV and CC charging	DC bus voltage
V2G	Yes	Discharging	DC bus voltage	P and Q
V2H	No	Discharging	DC bus voltage	AC voltage

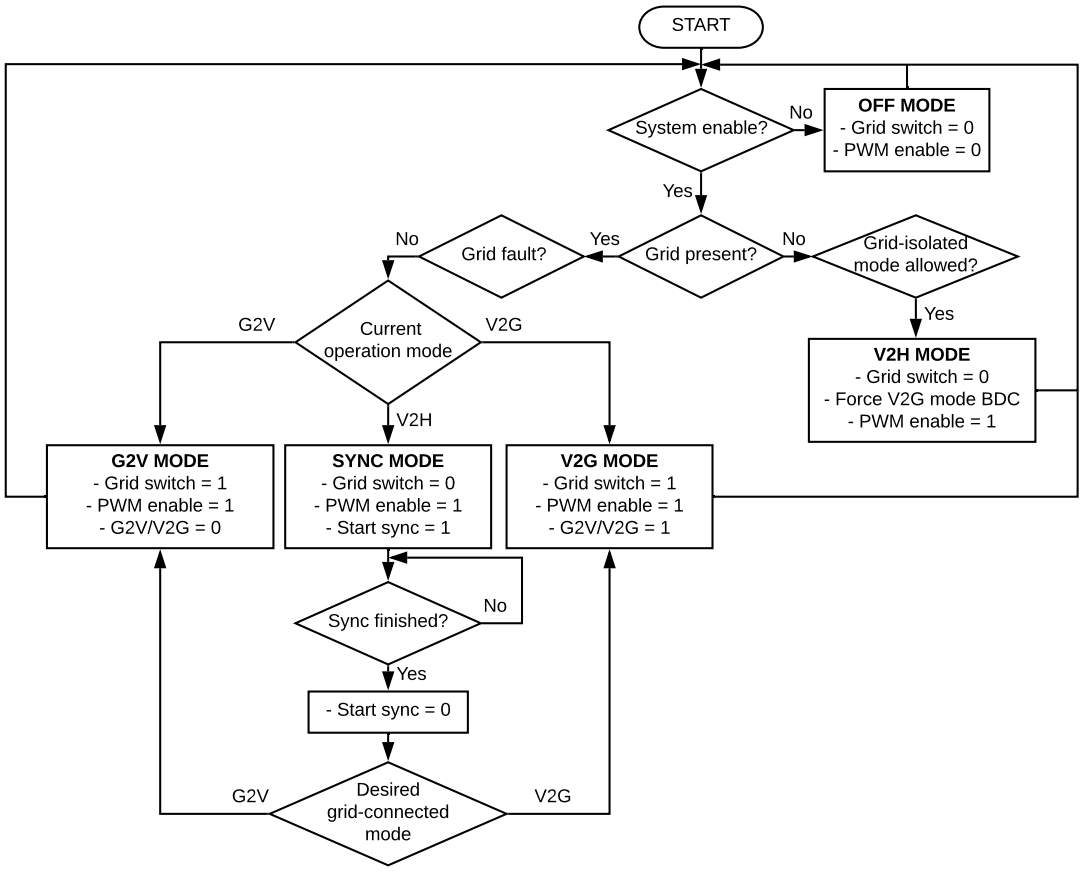

Figure 4.4: High-level control logic to determine the system mode of operation.

4.2.1 DC/DC converter control

The proposed BDC control strategy is represented in Figure 4.5 and it requires the following measurements and set points:

- Measurements
  - V_B - battery voltage,
  - I_L - battery-side inductance current,
  - V_{DC} - DC-link voltage.
- Set points
  - $V^*_{B_{\mathrm{CV}}}$ - constant battery voltage in CV charging mode (battery specifications)
  - $I^*_{B_{\mathrm{CC}}}$ - constant battery current in CC charging mode (battery specifications)
  - V^*_{DC} - DC-link voltage set point

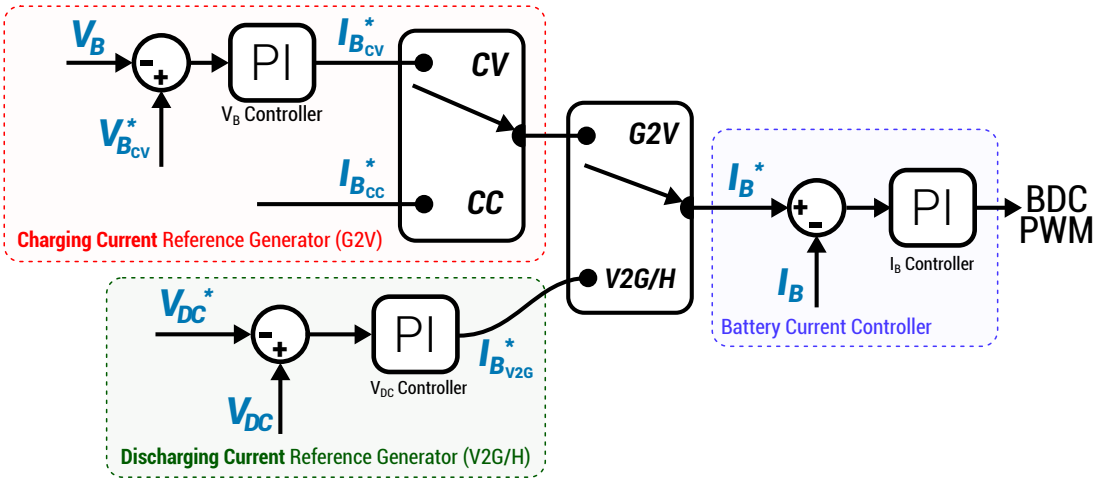

Figure 4.5: BDC control strategy in grid-connected (G2V/V2G) and in grid-isolated (V2H) mode.

The BDC control strategy can be divided in three subsystems, explained as it follows:

- Charging Current Reference Generator (G2V)
  - Responsible for generating a battery current reference I_B^* to control the battery charging current in G2V mode, be it in a constant current (CC) or a constant voltage (CV) charging mode. In constant current (CC) charging mode the current reference $I_{B_{CC}}^*$ can be set to equal the maximum or a given percentage of the battery nominal charge current. In constant voltage (CV) charging mode a PI controller compares the battery voltage with the nominal battery charging voltage $V_{B_{CV}}^*$ and generates a battery current reference $I_{B_{CV}}^*$ to maintain the battery voltage constant. This charging current reference is only generated in grid-connected mode.
- Discharging Current Reference Generator (V2G/H)
  - Responsible for generating a battery drain current reference to maintain the voltage across the capacitor in the DC bus constant. In this mode a PI controller compares the voltage V_{DC} with the reference value V_{DC}^* and generates the needed $I_{B_{V2G}}^*$ to maintain the DC bus voltage constant. This V_{DC} control method is used both in V2G and V2H modes, grid-connected and grid-isolated modes, respectively.

- Battery Current Controller

  - This subsystem contains a PI controller comparing the battery current reference I_B^* given by the two aforementioned subsystems and the current battery current value I_B, generating a BDC control signal. This signal is converted to a PWM signal to drive the IGBT gates in the BDC converter in order to achieve the desired battery current.

4.2.2 Bidirectional single-phase voltage source inverter control

The VSI is controlled differently depending on the mode of operation, requiring the following measurements:

- Measurements

  - V_{DC} - DC-link voltage
  - $I_{O_{\mathrm{dq}}}$ - output current *dq*-components (output PLL)
  - $V_{O_{\mathrm{dq}}}$ - output voltage *dq*-components (output PLL)
  - θ_{g} - grid voltage phase (grid PLL)
  - θ_{o} - output voltage phase (output PLL)

- Set points

  - V_{DC}^* - DC-link voltage set point
  - P_{REF} - active power reference
  - Q_{REF} - reactive power reference

In grid-connected mode, it can operate in G2V or V2G modes using a voltage-oriented control scheme, which allows separate control of the active and reactive powers being exchanged with the grid, as well as guaranteeing grid synchronization due to usage of a phase-locked loop (PLL). The separate control of the active and reactive powers is performed as depicted in Figure 4.6 and it works as it follows:

- *V2G mode*: in V2G mode, the active and reactive power is set externally by P_{REF} and Q_{REF}. Since the active power delivered to the grid is proportional to the output current d-component, i_d, and the reactive power proportional to the output current q-component,

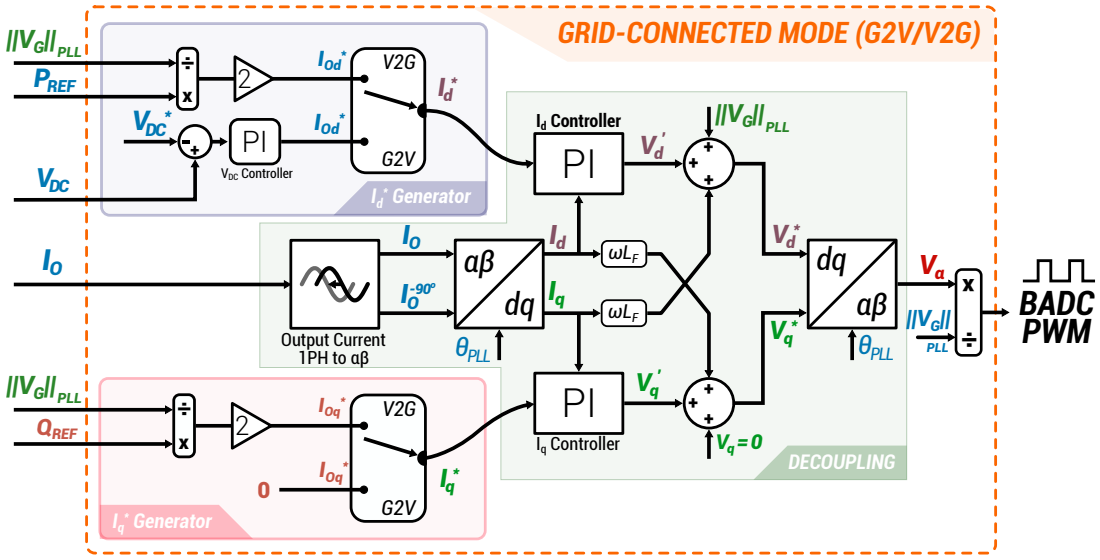

Figure 4.6: BADC control algorithm overview while operating in grid-connected mode (G2V or V2G).

i_q, converting these power quantities into the desired dq-components of the output current requires power calculations in dq-theory[1], resulting in dq-current references, i^*_{Od} and i^*_{Oq}, which are fed into classical PI controllers that in turn give out V'_d and V'_q, called demand values [80].

- *G2V mode*: in G2V mode the VSI is responsible for maintaining the DC link voltage constant, acting similar to the BDC in V2G mode as aforementioned. In this mode a PI controller compares the voltage V_{DC} with the reference value V^*_{DC} and generates the needed current to be extracted from the grid and injected into the DC link I^*_{DC} to maintain the DC bus voltage constant while maintaining unitary power factor, since the q-component of the grid component is kept null. Thus, in this mode there is a 180º phase difference between the VSI voltage and current outputs.

As displayed in Figure 4.6 the dq-current controllers only calculate the demand values V'_d and V'_q. In order to obtain the true V_d and V_q values, a process called decoupling is necessary. Decoupling takes into account the dynamics of the inverter AC-side, including output filter.

[1] See page 36 with the Equations (3.21) and (3.22) respectively for instantaneous active and reactive power calculations in dq-theory.

Signals such as θ_{PLL} and $||V_G||_{\text{PLL}}$ represent respectively the grid voltage phase and amplitude, needed for grid synchronization. These signals are calculated via a Phase-Locked Loop (PLL)[2].

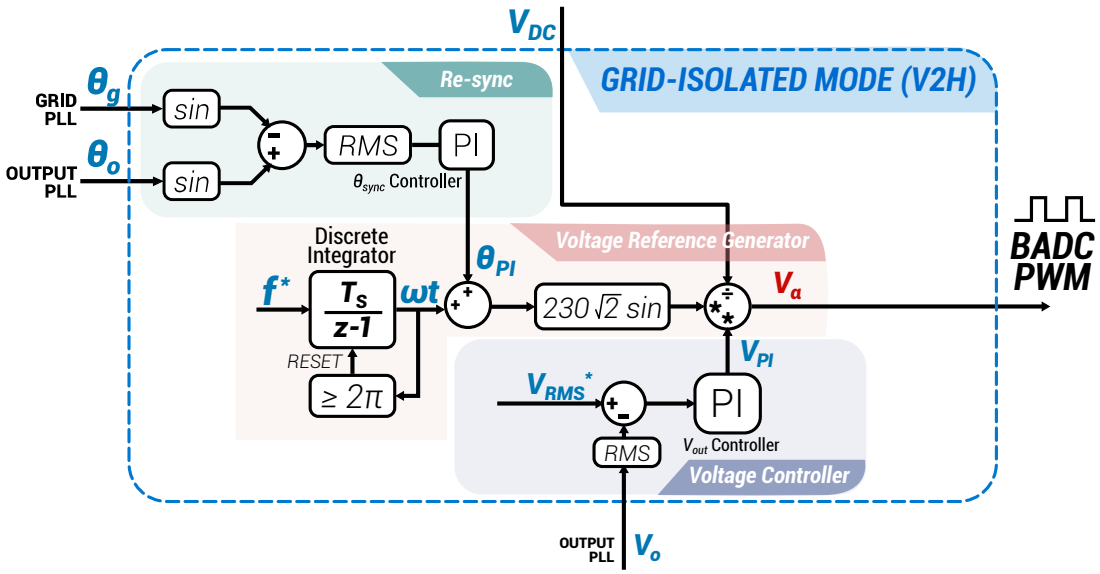

Figure 4.7: BADC control algorithm overview while operating in grid-isolated mode (V2H).

In grid-isolated mode the VSI must be controlled with a fixed sinusoidal voltage reference since grid synchronization is not possible. This voltage reference in V2H mode is obtained via the system represented in Figure 4.7. This system uses a fixed frequency reference, 50 Hz, to generate a signal ωt via a discrete integrator. The maximum value of ωt is limited 2π, that is, 360º, given that the integrator is reset when ωt reaches this value.

In the event of grid reconnection in V2H mode, the VSI output might be at a different frequency or out-of-phase in relation to the grid voltage and thus a grid re-synchronization strategy is required. For that, an initial phase, θ_0, given by a PI controller that compares and reduces the difference between the grid and output phase, is added to the resulting signal.

The sum $\omega t + \theta_0$ is converted into a sinusoidal reference with a 230 V RMS value. The peak voltage is divided by the DC link voltage to obtain the PWM reference signal corresponding to a 230V RMS output. The voltage output requires a closed-loop control to ensure a steady V^*_{RMS} voltage regardless of the load, up to the specified inverter power limits. The voltage controller

[2]Further details about the PLL structure used can be found in Subsection 4.3.3 on page 52.

output is limited to a ±5% variation to prevent over-voltage conditions.

4.3 Simulation model

This section concerns the methods and materials used to create a computational model of the power structure and control algorithms described in Sections 4.1 and 4.2 respectively. Simulation is useful to assess the system behaviour in relevant environments and different conditions by gathering and analyzing data from the simulation results. The gathered data is used to validate the control algorithm experimentally later on.

The simulation of the system was carried out with the software MATLAB and Simulink by MathWorks, as well as the *Specialized Power Systems* library under Simscape. In order to emulate the physical setup the simulation step-time was chosen to be 2 μs, corresponding to a 500 kHz sampling rate. The control algorithm, however, is executed with a lower sampling rate of 10 kHz, since the physical IGBTs have a maximum switching rate of 10 kHz. The experimental setup is further explained in section 4.4.

In this section the subsystems of the model created in Simulink are listed, along with relevant explanations about their functions and features.

4.3.1 Model overview

An overview of the Simulink model showing the two main blocks can be seen in Figure 4.8 on page 52. One block contains the power structure and measurements and the other contains the control algorithm and PWM signal generators. The blocks placed between the two main blocks are low-pass filters used to improve the measurement signals sent to the control algorithm.

The following subsections contain more details on the sub-components of these two main blocks, such as the phase-locked loop model, the power structure itself, the VOC algorithm and the PWM generators.

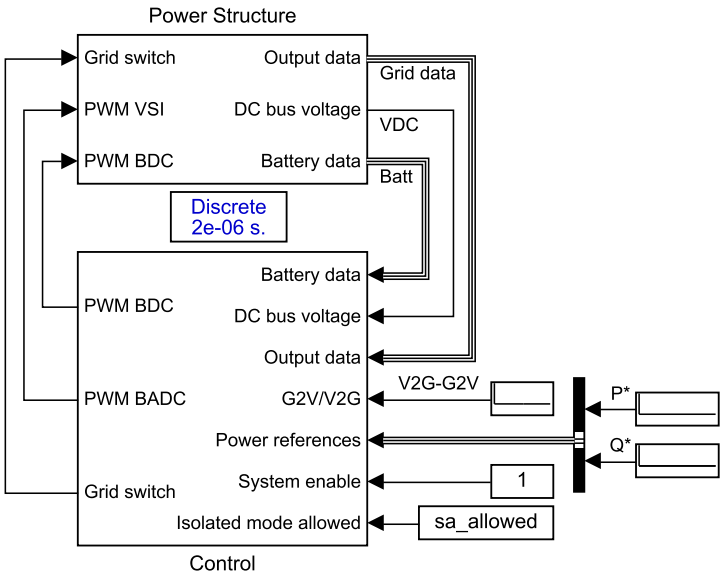

Figure 4.8: Simulink model overview.

4.3.2 Battery model

The battery is modelled using a Simulink-built-in block from the Simscape Specialized Power System library. The block implements a generic dynamic model parameterized to represent most popular types of rechargeable batteries [81]. To reflect the physical implementation in which 8 UCG-12 batteries from Ultracell are used, the battery type in the simulation is set to lead-acid, with a 20 Ah capacity, 120 mΩ internal resistance, fully charged voltage of 104,5263 V and maximum charging current of 4 A.

4.3.3 Phase-locked loop model

The phase-locked loop (PLL) is responsible for extracting the phase (θ) of an input signal. In Simulink the PLL responsible for extracting the grid voltage phase and its peak value was implemented as displayed in Figure A.1. Its structure is based on the structure devised by Ciobotaru, Teodorescu, and Blaabjerg [82].

4.3.4 Power structure model

The power structure was modelled using the Simscape *Specialized Power Systems* library in Simulink. It comprises a three-phase inverter with 6 IGBTs representing both the VSI, using 4 switches controlled by the VOC algorithm, and the DC/DC converter, which uses 2 IGBTs. The grid representation is achieved via addition of a transformer coupled with a swing-type AC voltage source, which controls its magnitude and phase and thus models an infinite bus, absorbing or delivering whatever power rating is needed.

The power structure as modelled in Simulink can be seen in Figure 4.9 and the control structure in Figure A.2.

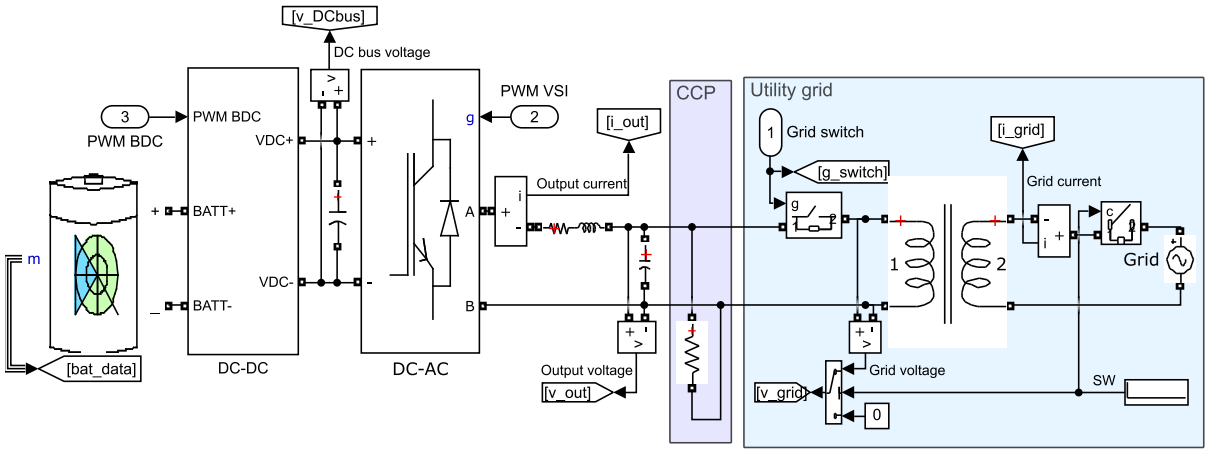

Figure 4.9: Power structure modelled in Simulink.

4.3.5 Logical control

The logical system control in Simulink is shown in Figures A.3 and A.4. It controls the transition between different modes of operation.

4.3.6 Voltage-oriented control model

The voltage-oriented control algorithm as modelled in Simulink can be seen in Figure A.6. The *dq* current controllers are also shown in Figures A.7 and A.8. A rate limiter was added to the active and reactive power references given externally, to prevent abrupt changes in these

values.

4.3.7 Bidirectional DC/DC control model

An overview of the BDC control model in Simulink is exhibited in Figure A.12. It comprises three different subsystems, the battery current controller as in Figure A.13, and the battery current reference generators used in V2G/H (Figure A.15) and G2V operation mode (Figure A.14), the latest containing the constant-voltage and constant-current battery charging algorithm.

4.3.8 Vehicle-to-Home model

Figure A.9 shows the voltage reference generator used for operation in V2H mode. For voltage regulation the PI controller represented in Figure A.10, was implemented in Simulink and for grid re-synchronization the PI controller in Figure A.11 controls the initial phase of the voltage generator to match the output voltage with that of the grid.

4.3.9 Pulse-width modulation model

Figure A.19 contains the Simulink model with the BADC and BDC PWM signal generators, each, respectively, shown in Figures A.21 and A.20 with more details.

4.3.10 Fault detection model

The fault detection module in Simulink is displayed in Figure A.16 and it contains the subsystems to verify if the grid voltage (Figure A.17) or frequency (Figure A.18) present abnormal values or rates of change. If yes, the system is shut down in case V2H mode is not allowed or if V2H is allowed the system transitions to a grid-isolated operation mode.

4.3.11 Parameters

Simulation parameters are listed in Table A.1 along with a short description and respective units.

4.3.12 Tests

Four simulated tests are proposed to evaluate the system operation in different conditions, being them:

- *Grid fault test*: in this test the electric grid connected to the inverter is disconnected, simulating a grid fault, and the features of islanding detection and seamless transfer mode to grid-isolated mode are tested.
- *Grid reconnection test*: this test shows again the seamless transfer mode and grid re-synchronization capabilities of the system.
- *Continuous grid-connected operation*: demonstrates the different system modes of operation while connected to an electric grid, thus including V2G and G2V operation modes with varying power references.
- *Grid-connected operation mode transition*: displays the system capability of switching between V2G and G2V operation modes maintaining system stability.

4.4 Experimental platform

Experimental validation was performed using a Real-Time Interface (RTI). The dSPACE DS1103 PPC Controller Board was used for real-time control of measurements and interfacing between the hardware and software, namely, the Simulink control model and the supervision and data collection software, the dSPACE Control Desk.

A signal conditioning (SC) step was added between the measurements and the Controller Board allowing it to acquire all the relevant signals in the allowed voltage ranges.

Six IGBT switches belonging to the BDC and BADC are housed in the PM75RLA120 power module from Mitsubishi Electric [83], a three-phase full-bridge inverter. Two of its inverter arms are used for the BADC and the remaining inverter arm is used for the BDC. The IGBT switches are controlled via the BP7B isolation circuit from Powerex [84].

The DC link capacitance is 1 mF, achieved by connecting two 1 mF capacitors in parallel, each with 400V rating, in series with other two 1 mF capacitors with 400V rating connected in

parallel, resulting in an overall 1 mF capacitance and 800V maximum rated voltage.

An overview of the experimental platform is shown in Figure 4.10 and more details about the experimental components are given in the following subsections.

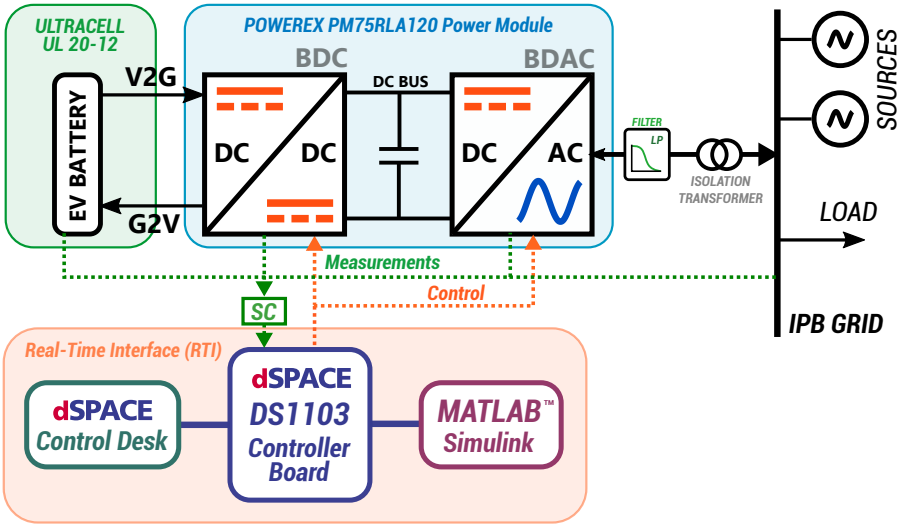

Figure 4.10: Experimental layout overview.

4.4.1 Controller board DS1103 from dSPACE

The dSPACE DS1103 real-time controller board offers sixteen 16-bit multiplexed channels equipped with 4 sample and holds A/D converters, eight D/A channels with 16-bit resolution, 32-bit parallel digital I/O, a CAN and serial interfaces, slave DSPs, 6-channel analog incremental encoder interface and interrupt controllers. The board within the experimental platform is shown in FIgure 4.11.

4.4.2 dSPACE Control Desk 3.7.1

The Control Desk software from dSPACE is an instrumentation software for electronic control unit (ECU) development with integrated ECU calibration, measurement and diagnostics access, allowing for synchronized data capture across Electronic Control Unit, Rapid Control Prototyping and Hardware-in-the-Loop platforms and bus systems. It provides layouting,

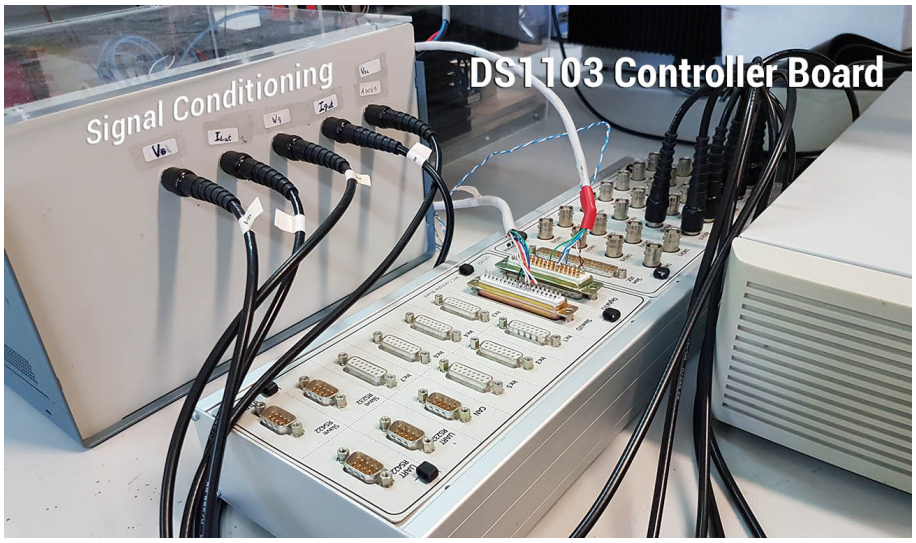

Figure 4.11: DS1103 Controller Board and outputs from signal conditioning module.

instrumentation, measurement and post-processing features [85]. The layout developed for testing of the proposed system in the Control Desk software is displayed in Figure 4.12.

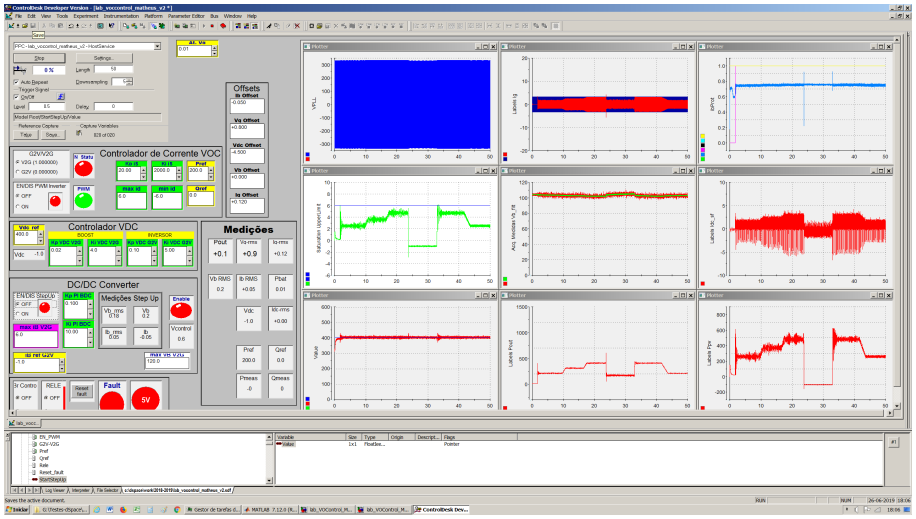

Figure 4.12: dSPACE Control Desk 3.7.1 window for monitoring and testing of the physical implementation showing the implemented test layout.

4.4.3 Signal conditioning

Signal conditioning was performed to allow the measured voltage and current signals to be read by the dSPACE Controller Board, which has an input range of ± 10V.

The signal conditioning module, as displayed in Figure 4.13, is powered by three TRACO Power power supplies, TML10205 (± 5 V), TML30215 (± 15 V) and TML10124 (24 V). It contains 5 measurement channels, each filtered by a LTC1065 Linear Phase 5^{th} Order Bessel Lowpass Filter and converted to values within the Controller Board input voltage range of ± 10 V by an OP270 operational amplifier.

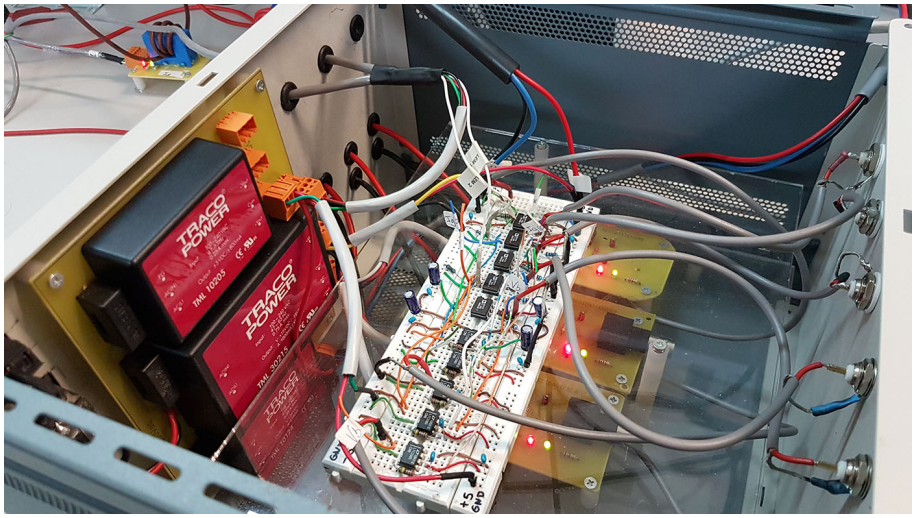

Figure 4.13: Signal conditioning module.

4.4.4 Batteries

The battery energy storage system contains 8 batteries UCG20-12 from Ultracell connected in series, each with a 20 Ah capacity and 12 V nominal voltage, as in Figure 4.14. Thus, the battery system has a nominal voltage of 96 V and 20 Ah capacity, or 1,96 kWh.

4.4.5 Power electronics module

The IGBT switches are housed in the PM75RLA120 power module from Mitsubishi, each with a nominal collector current of 75 A. The IGBTs are active low (< 0.8 V) and need a 15V control supply voltage (from the signal conditioning module), being isolated from the control signals by the BP7B isolation circuit from Powerex. The module is supplied by the 24V power supply in the signal conditioning module as well. The power electronics module and the isolation

Figure 4.14: Ultracell UCG20-12 batteries.

circuit can be seen in Figure 4.15.

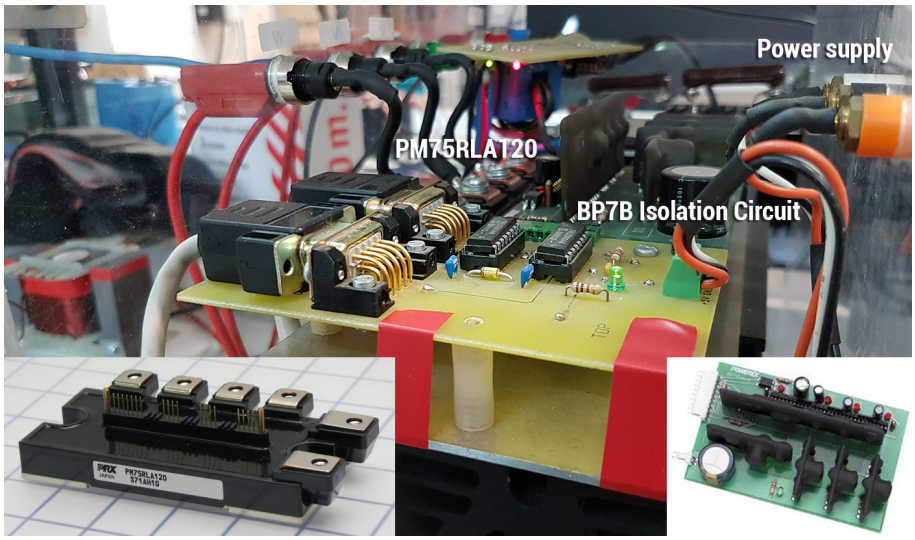

Figure 4.15: Power electronics module PM75RLA120 (bottom left corner) and BP7B isolation circuit (bottom right corner).

4.4.6 Real-time simulation model in Simulink

In order to control the power electronics module a Simulink control model that acts in real time was used. In this simulation, input and output blocks are provided by the RTI library from dSPACE, containing the PWM outputs and analog measurements inputs. This model is built from MATLAB, generating a file in which the control is built in and so are the labels,

inputs and outputs. These can be controlled within the Control Desk software, allowing real-time interfacing between the Simulink control model and the power structure.

Chapter 5

Simulation Results

This chapter contains the results obtained via simulation of the power system under study. Four tests were executed to evaluate the system operation, being them:

- *Grid fault test*: in this test the electric grid connected to the inverter is disconnected, simulating a grid fault, and the features of islanding detection and seamless transfer mode to grid-isolated mode are tested.
- *Grid reconnection test*: this test shows the seamless transfer and grid re-synchronization capabilities of the system.
- *Continuous grid-connected operation*: demonstrates the different system modes of operation while connected to an electric grid, thus including V2G and G2V operation modes with varying power references.
- *Grid-connected operation mode transition*: displays the system capability of switching between V2G and G2V operation modes maintaining system stability.

The PI parameters used in the simulation are listed in Table A.1. The simulation was performed in the discrete domain to reflect the physical implementation and allows for usage of similar PI parameters in the experimental validation section.

5.1 Grid fault

This section contains the results obtained by simulating the system fault-detection/islanding-detection module and grid-isolated feature (V2H) when a grid disconnection or fault is detected during operation in grid-connected mode.

5.1.1 V2H mode disabled

Figure 5.1 shows the VSI output current and output voltage after a grid disconnection occurs at the 3 seconds mark. In this test the transition to a grid-forming operation mode is not allowed. At the 6 seconds mark the grid is back on, and Figure 5.1 shows the output current and voltage after detection of grid presence and following system reboot as well.

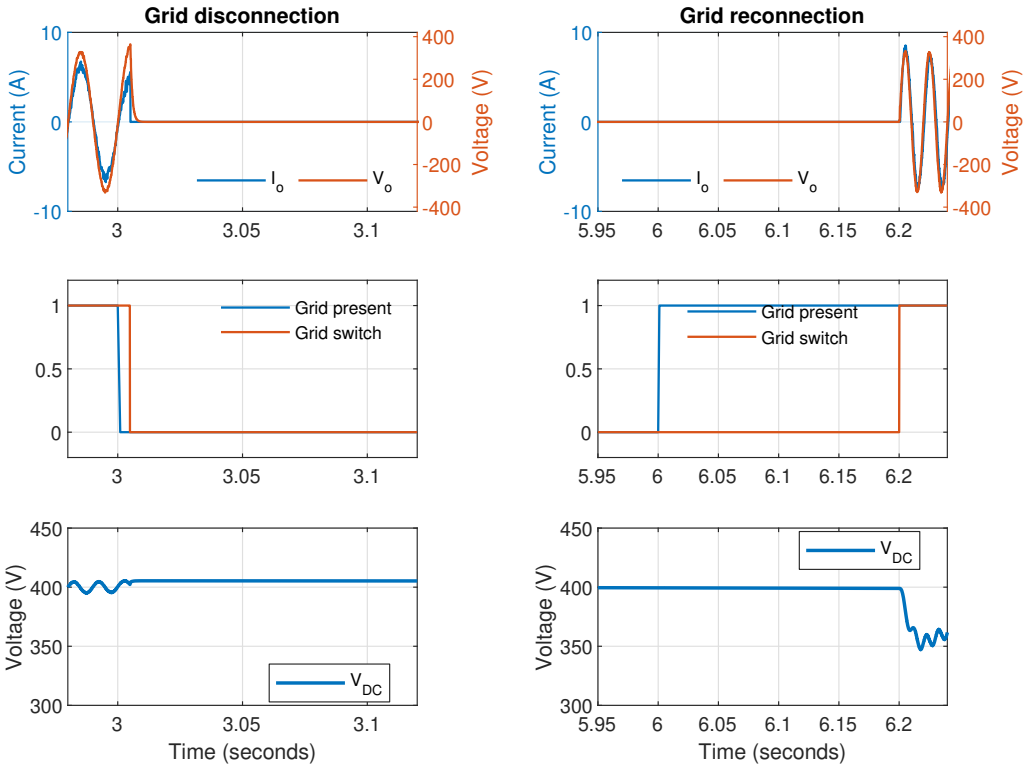

Figure 5.1: Left column: current and voltage output and DC link voltage after detection of a grid fault condition and following system shutdown. Right column: same variables after detection of grid presence and following system reboot.

5.1.2 V2H mode enabled

Figure 5.2 and 5.3 show the VSI output current and output voltage after a grid disconnection occurs at the 3 seconds mark and the transition to a grid-forming operation mode is allowed. A 700W load is connected to the common-coupling point to demonstrate the grid-forming capability and the smooth transition between delivering power to the grid and to supplying loads connected to the CCP.

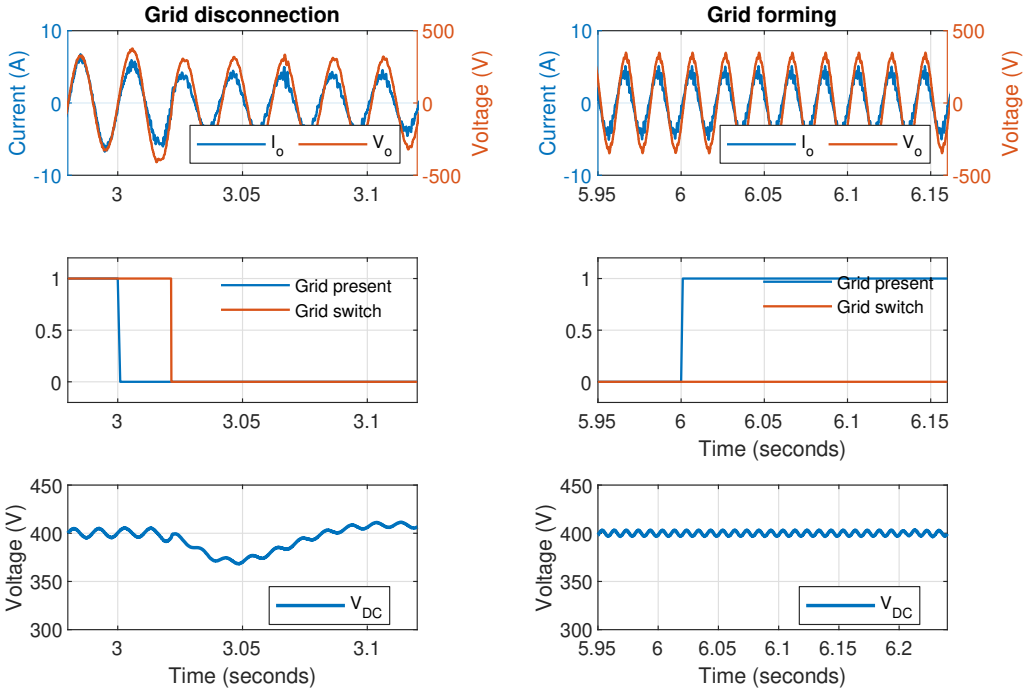

Figure 5.2: Output current and current during detection of a grid fault condition and beginning of transition from V2G to grid-isolated mode (V2H).

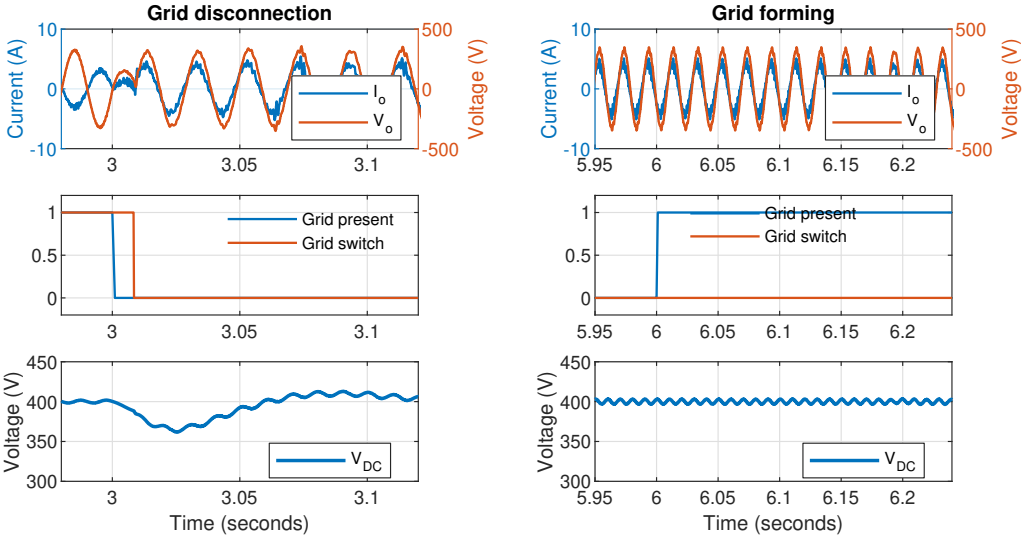

Figure 5.3: Output current and current during detection of a grid fault condition and transition from G2V to grid-isolated mode (V2H).

5.2 Grid reconnection

This section contains the results obtained by simulating the system grid-isolated feature (V2H) and seamless transition with smooth grid re-synchronization after a grid reconnection

is detected. For this test the grid voltage was set to be leading 45 degrees compared to the V2H voltage reference.

Figure 5.4 shows more details of the re-synchronization and transition processes from V2H to V2G and Figure 5.6 from V2H to G2V. Both figures display the output and grid phases, the error between them, the grid status, the current and voltage waveforms and the power output during these test conditions.

The transition from V2H to grid-tied operation modes is always executed when a voltage zero-crossing is detected to ensure a smooth transition. Complete re-synchronization takes approximately 3.2 seconds starting after detecting the grid presence for G2V and 1 second for V2G.

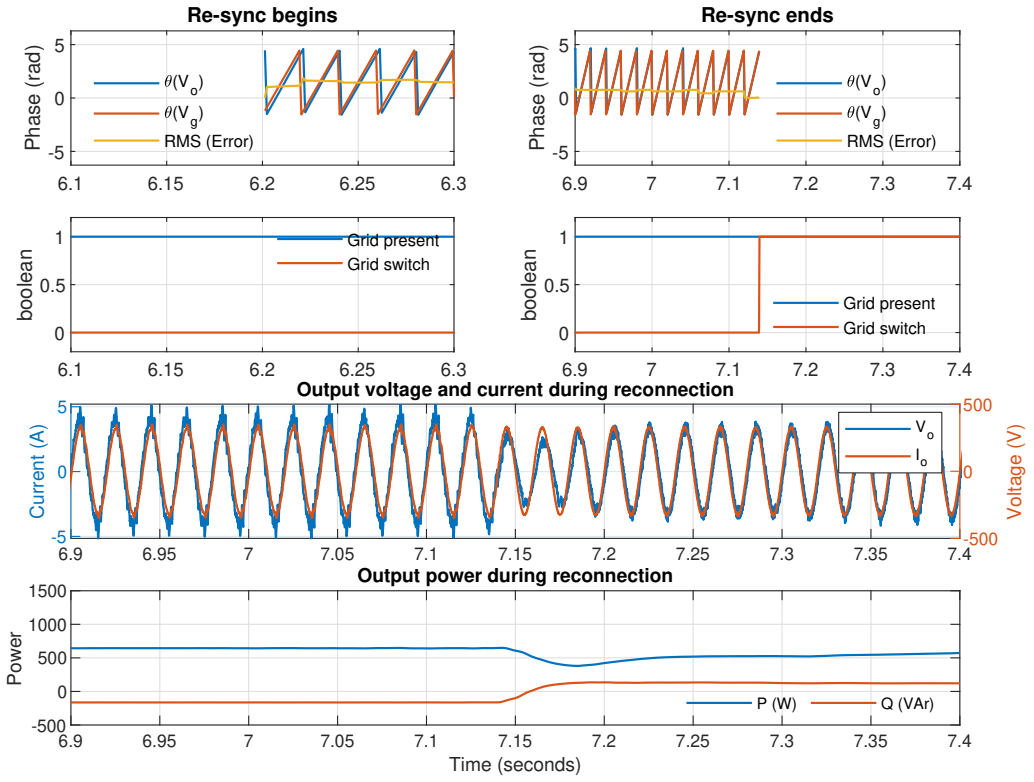

Figure 5.4: Re-synchronization and transition from grid-isolated to grid-tied V2G mode.

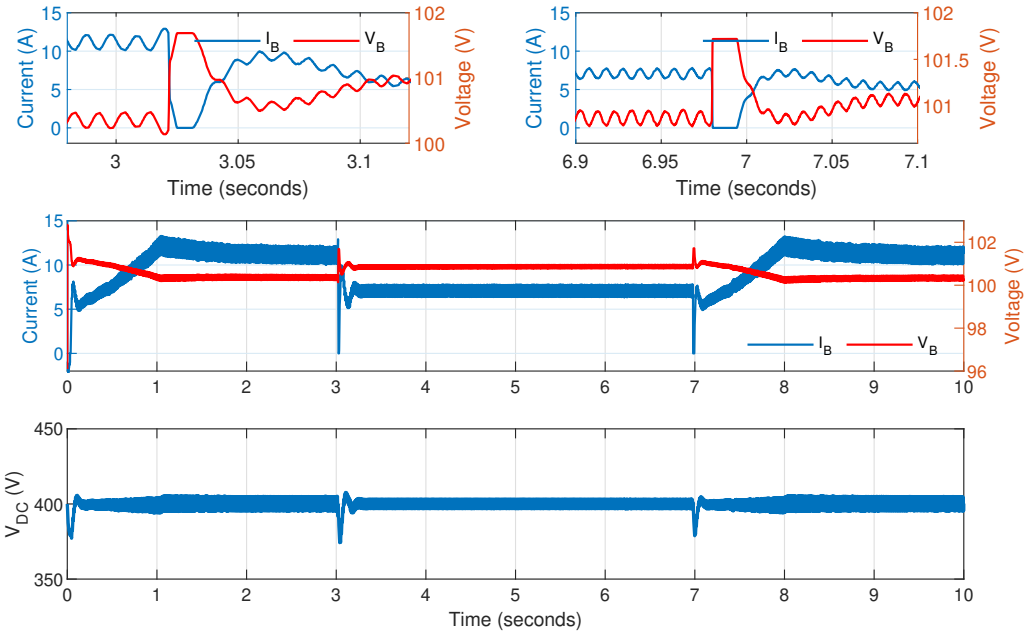

Figure 5.5: Battery current, voltage and DC link voltage during transitions between grid-isolated and grid-tied V2G mode.

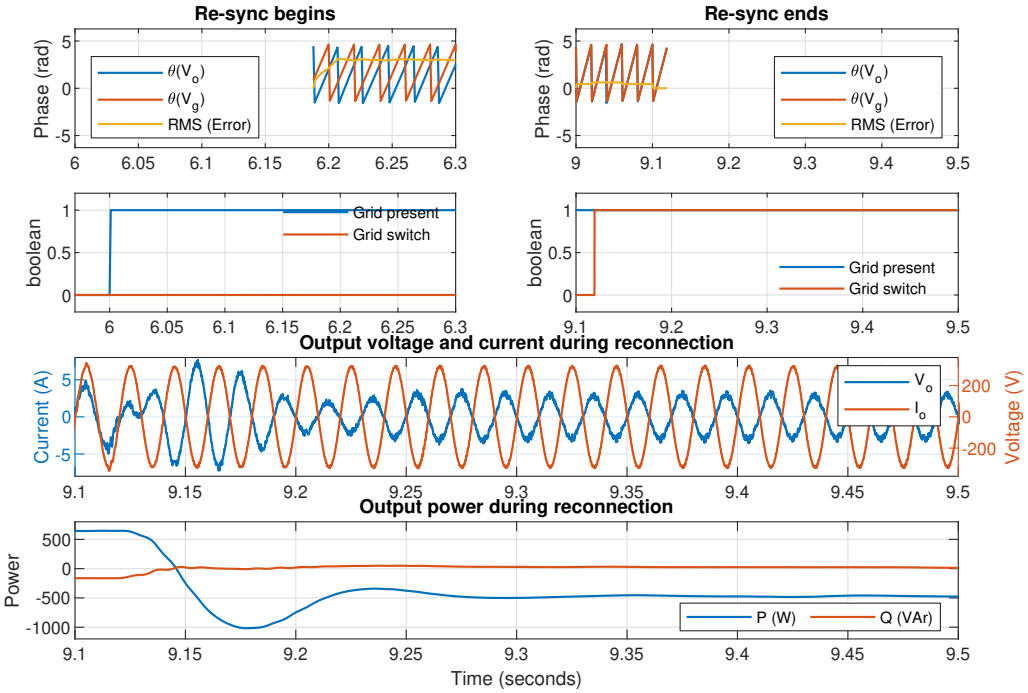

Figure 5.6: Re-synchronization and transition from grid-isolated to grid-tied G2V mode.

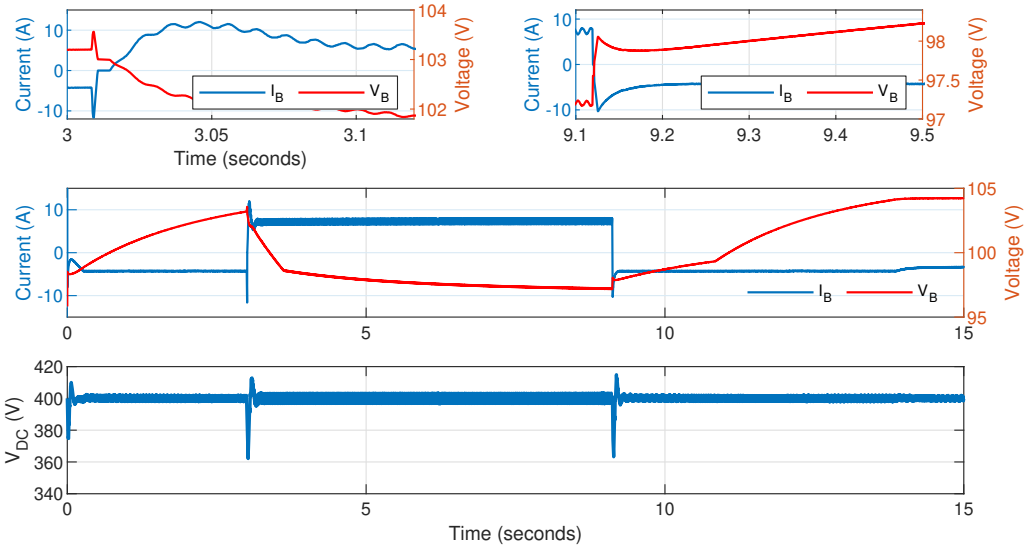

Figure 5.7: Battery current, voltage and DC link voltage during transitions between grid-isolated and grid-tied G2V mode.

5.3 Continuous grid-connected operation

The following results demonstrate the different system modes of operation while connected to an electric grid, thus including V2G and G2V operation modes with varying power references.

5.3.1 Vehicle-to-Grid (V2G) mode

In this simulation the active and reactive power references were varied during the simulation lasting 12.5 seconds to show operation in 5 different power combinations shown in Table 5.1.

Table 5.1: Active and reactive power references to test the system operation in 5 different power combinations in V2G mode.

Time	$0 < t \leq 2.5$	$2.5 < t \leq 5.0$	$5.0 < t \leq 7.5$	$7.5 < t \leq 10.0$	$10.0 < t \leq 12.5$
Active power (W)	1000	700	700	0	0
Reactive power (VAr)	0	700	-700	-700	700
Apparent power (VA)	1000	990	990	700	700

The measured power and reference power quantities are shown in Figure 5.8. Figure 5.9 shows the current and voltage outputs in the 5 power combinations.

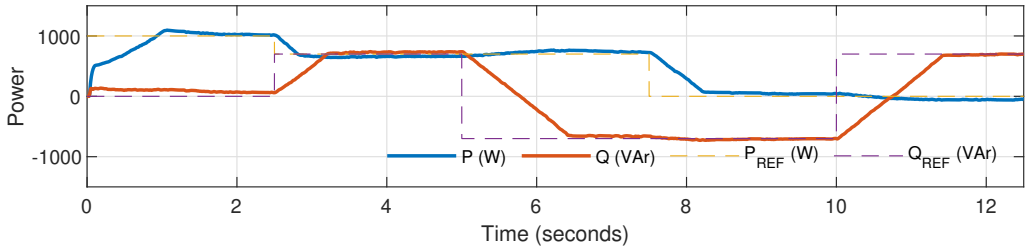

Figure 5.8: VSI output power measurements and power references from Table 5.1 in V2G mode.

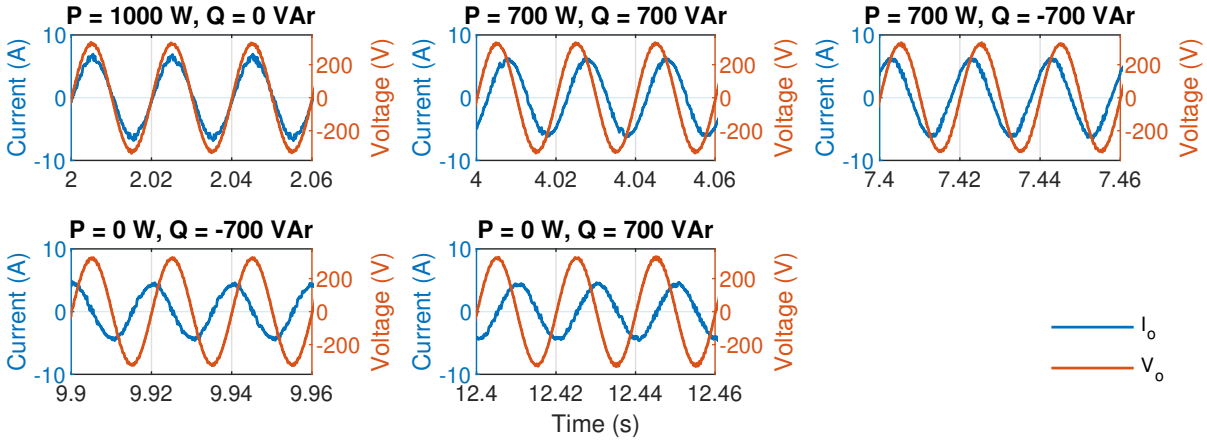

Figure 5.9: VSI output current waveform in the five different power references combinations from Figure 5.8 in V2G mode.

Figure 5.10 displays the battery voltage while operating in V2G. Battery voltage decreases proportionally to the active power requested externally. Figure 5.10 shows the inverse relationship for the battery current, directly proportional to the requested apparent power.

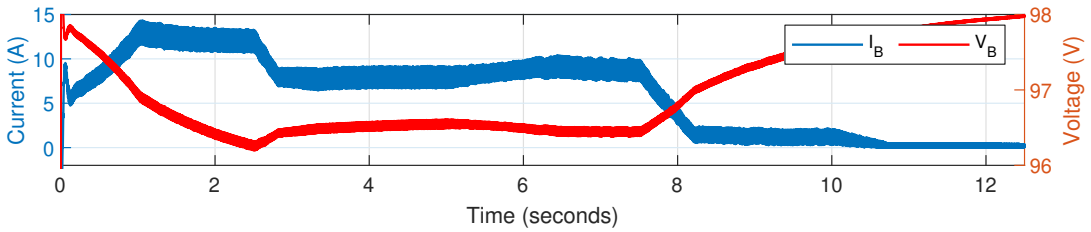

Figure 5.10: Battery voltage and current in the five different power references combinations from Figure 5.8 in V2G mode.

5.3.2 Grid-to-Vehicle (G2V) mode

During continuous G2V operation the grid current leads the grid voltage by 180 degrees. In this simulation the active and reactive power references were also varied during the simulation to show operation in 4 different power combinations, as displayed in Table 5.2. Since the active power withdrawn from the grid is defined by the battery charging algorithm - approximately 490 W in constant-current mode, the active power reference is given either by the CC or CV charging schemes.

Table 5.2: Active and reactive power references to test the system operation in 3 different power combinations in G2V mode.

Time (s)	$0 < t \leq 2.5$	$2.5 < t \leq 5.0$	$5.0 < t \leq 7.5$	$7.5 < t \leq 12.5$
Active power (W)	CC	CC	CV	CV
Reactive power (VAr)	0	700	-700	0

The measured power and reference power quantities are shown in Figure 5.11.

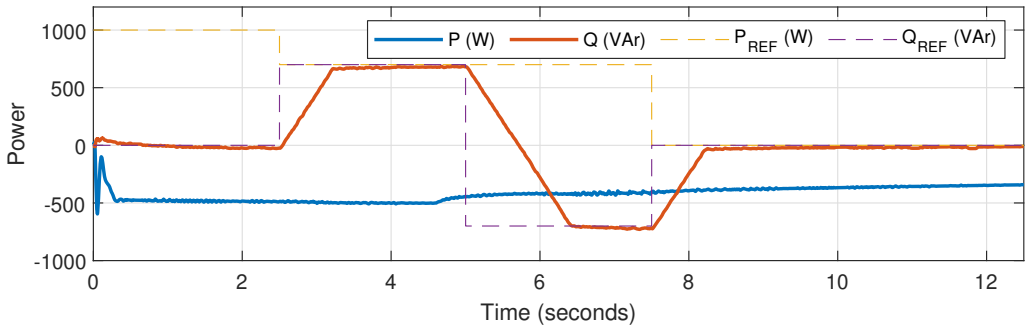

Figure 5.11: VSI output power measurement and power references in G2V mode.

Figure 5.12 shows the current and voltage outputs in the 3 power combinations. The active power in G2V mode is not set externally, but rather internally by the battery charging controller. This can clearly be seen in Figure 5.11 where the power reference line does not have any influence on the power being withdrawn from the grid to charge the battery. The reactive power however can be set externally, and thus, simultaneously charge the battery and act an active power factor corrector if needed. Figure 5.13 displays the battery voltage and current while operating in G2V.

Throughout operation, despite the changes in the requested reactive power output, the DC link voltage represented in Figure 5.14 remains fairly constant, proving the system stability.

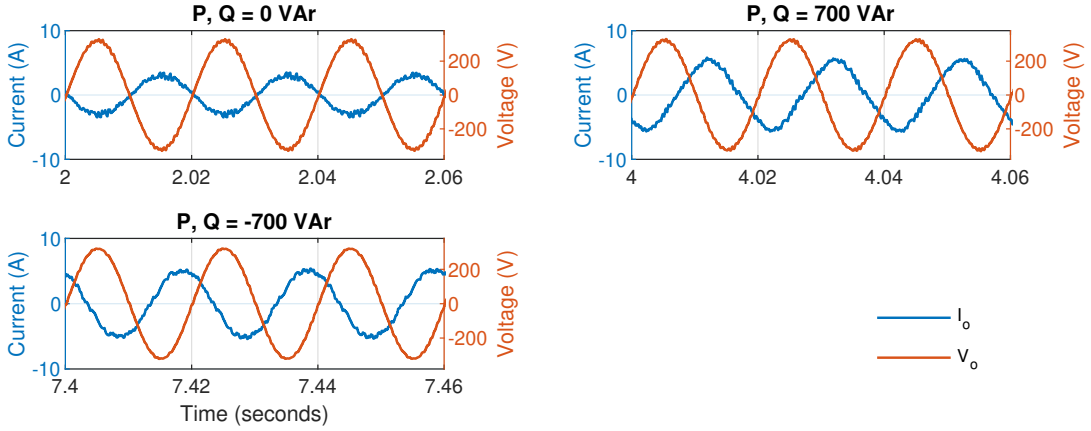

Figure 5.12: VSI output current waveform in the three different power references combinations from Figure 5.11 in G2V mode.

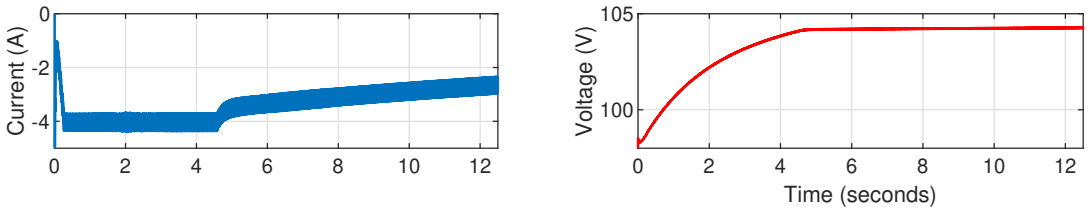

Figure 5.13: Battery voltage and current in the four different power references combinations from Figure 5.11 in G2V mode.

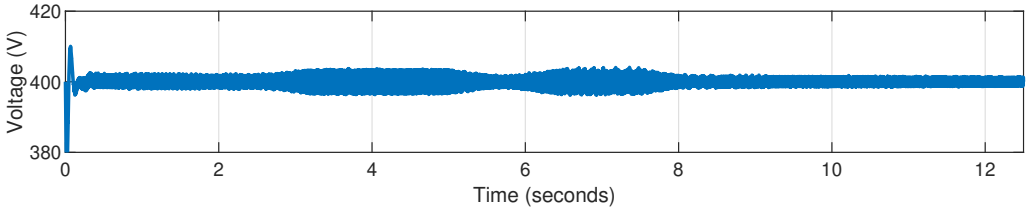

Figure 5.14: DC link voltage in the four different power references combinations from Figure 5.11 in G2V mode.

5.4 Grid-connected operation mode transition

The following results display the system capability of switching between V2G and G2V operation modes maintaining system stability. All the switching operations are only performed when the output current crosses zero in order to reduce transients.

5.4.1 Transition from V2G to G2V

Figure 5.15 exhibits the VSI output current waveform and output power during mode transition from V2G to G2V. The transition is requested at the 3 seconds mark and the figure shows the transition of the current phase in relation to the grid voltage, from being in opposite phase before the 3 seconds mark and becoming in-phase after the 3 seconds mark.

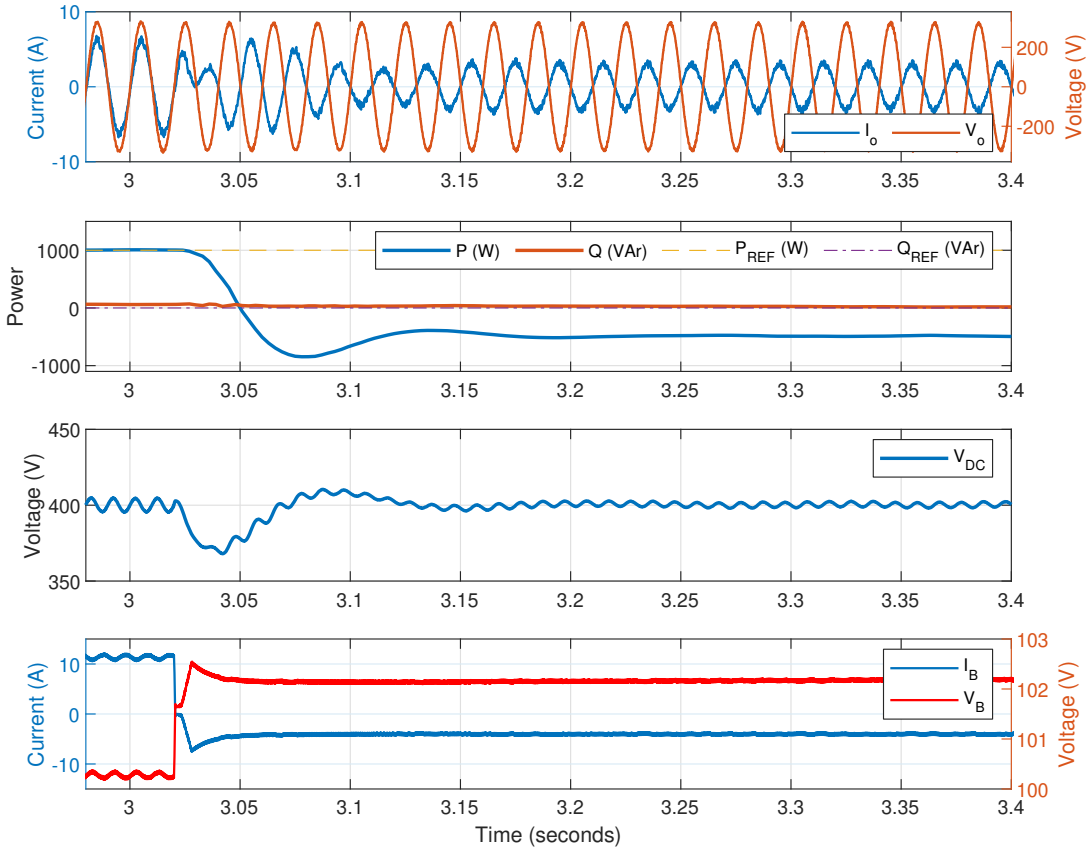

Figure 5.15: VSI output current waveform and output power during mode transition from V2G to G2V.

5.4.2 Transition from G2V to V2G

Figure 5.16 exhibits the VSI output current waveform and output power during mode transition from G2V to V2G. The transition is requested at the 2 seconds mark and the figure shows the transition of the current phase in relation to the grid voltage, from being in-phase before the 2 seconds mark and becoming in opposite phase after the 2 seconds mark.

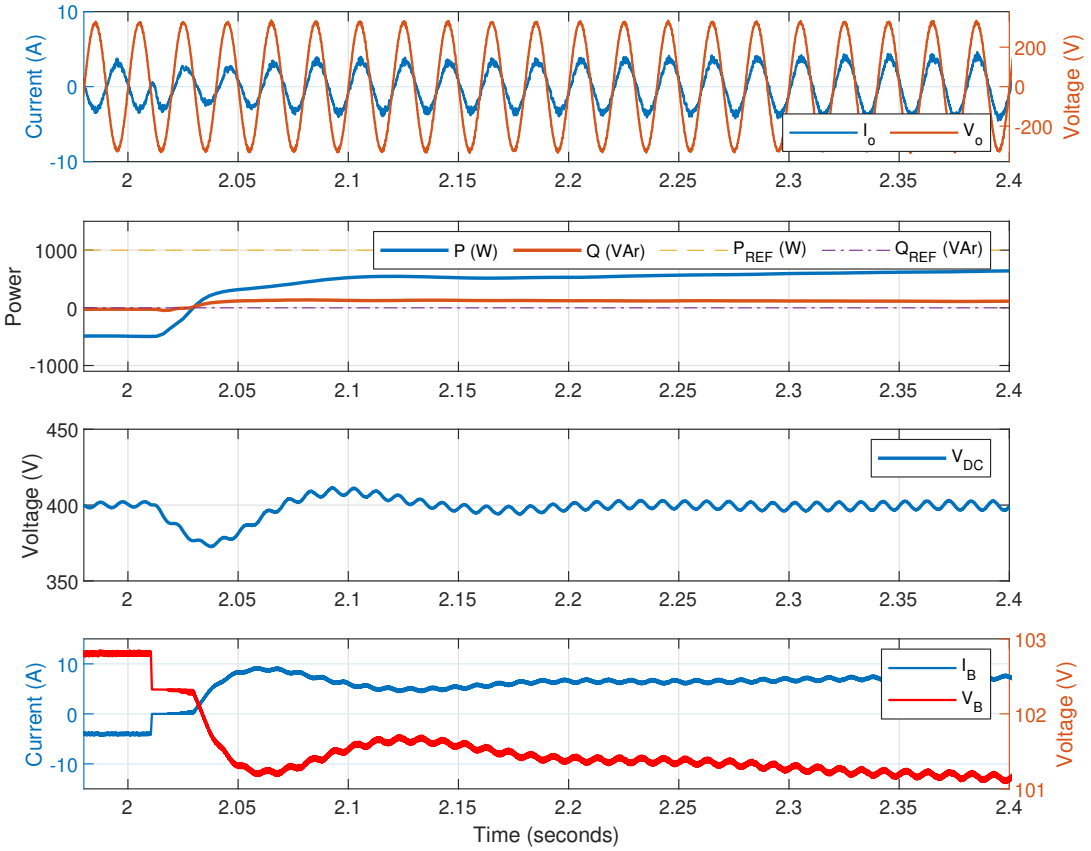

Figure 5.16: VSI output current waveform and output power during mode transition from G2V to V2G.

Chapter 6

Experimental Results

This chapter contains the results obtained via experimentation with the physical implementation of the power system under study. The V2G and G2V grid-connected features and the transition between these modes was tested with the real-time interface explained in Section 4.4. Operation in grid-isolated mode (V2H) was not tested experimentally.

The PI controllers parameters were changed from the simulation parameters to optimize the system behaviour in the experimental validation. The new PI parameters used are listed in Table 6.1.

Table 6.1: PI controllers parameters for experimental validation.

Parameter	Values	
	Simulation	Experimental
PI controller - dq Currents		
kp_iS	20	20
ki_iS	30	2000
PI controller - DC link voltage - V2G		
kp_vDC_V2G	0,2	0,02
ki_vDC_V2G	10	4
PI controller - DC link voltage - G2V		
kp_vDC_G2V	0,1	0,1
ki_vDC_G2V	10	5
PI controller - Battery current		
kp_bb	0,1	0,1
ki_bb	5	10

The tests that were performed are listed as it follows:

- *Test 1* - Vehicle-to-Grid (V2G) mode with varying reactive power references and static active power output;
- *Test 2* - Vehicle-to-Grid (V2G) mode with varying active power references and null reactive power output;
- *Test 3* - Grid-to-Vehicle (G2V) mode with varying battery charging current references and null reactive power compensation;
- *Test 4* - Transition between the G2V and V2G operation modes.

6.1 Continuous grid-connected operation

The following results demonstrate the different system modes of operation while connected to an electric grid, thus including V2G and G2V operation modes with varying power references.

6.1.1 Vehicle-to-Grid (V2G) mode

In the first test the active and reactive power references were varied during the experiment lasting 40 seconds. The operation mode was set to V2G and the results show stable operation in 5 different power combinations, being them:

- Active power 200 W and reactive power 0 VAr, total apparent power 200 VA
- Active power 200 W and reactive power 100 VAr, total apparent power 223 VA
- Active power 200 W and reactive power 200 VAr, total apparent power 282 VA
- Active power 200 W and reactive power -100 VAr, total apparent power 223 VA
- Active power 200 W and reactive power -200 VAr, total apparent power 282 VA

The grid voltage and the VSI current output during operation with the aforementioned power combinations in the first test are shown in Figure 6.1. The power withdrawn from the battery and the power delivered to the grid during the first test are displayed in Figure 6.2, while Figure 6.4 shows the battery voltage and current during the test. Figure 6.3 shows the DC link voltage, proving the stable operation in the test conditions.

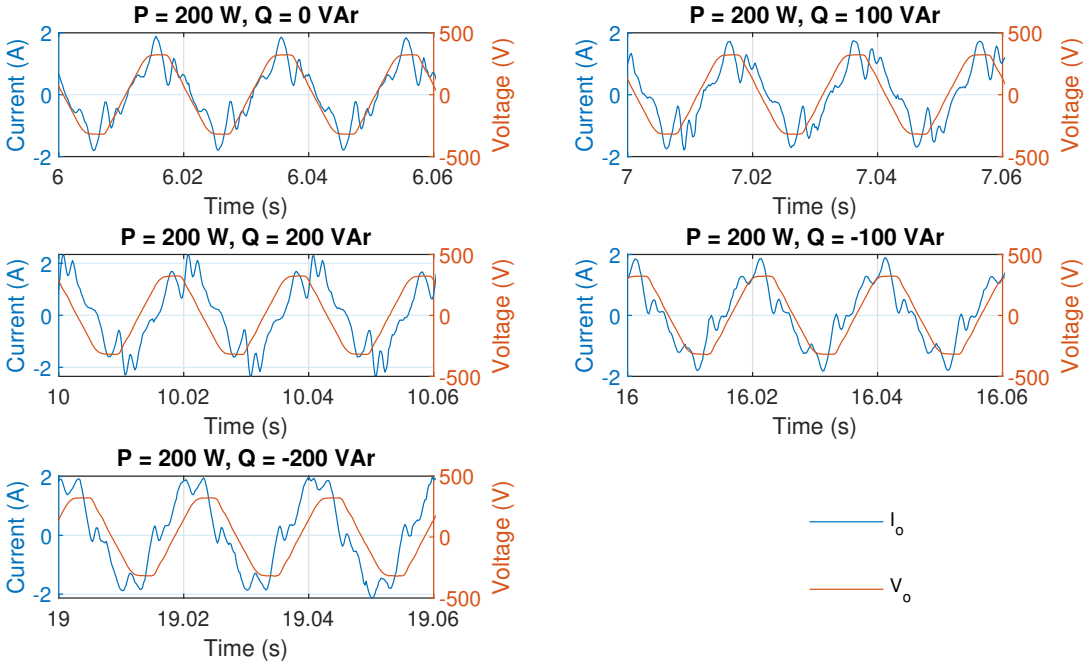

Figure 6.1: Test 1 - Output current and grid voltage during V2G operation mode.

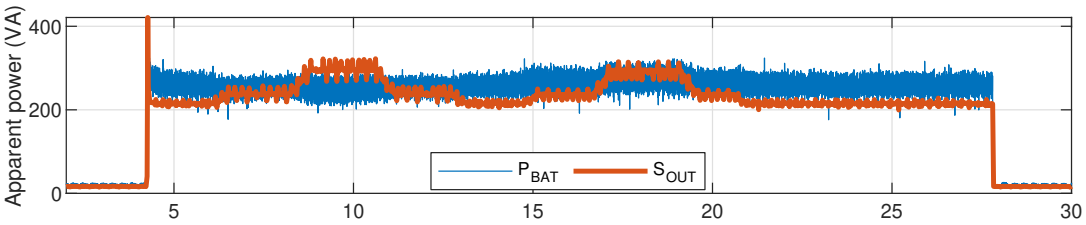

Figure 6.2: Test 1 - Battery and output power during V2G operation mode.

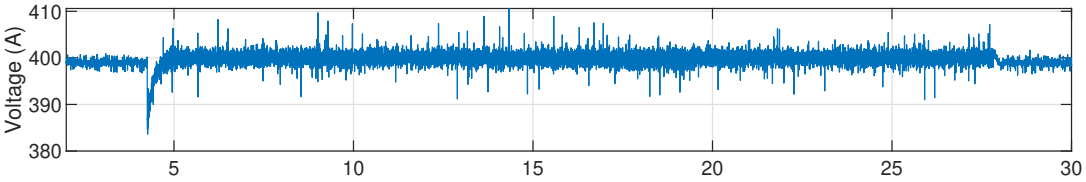

Figure 6.3: Test 1 - DC link voltage during V2G operation mode.

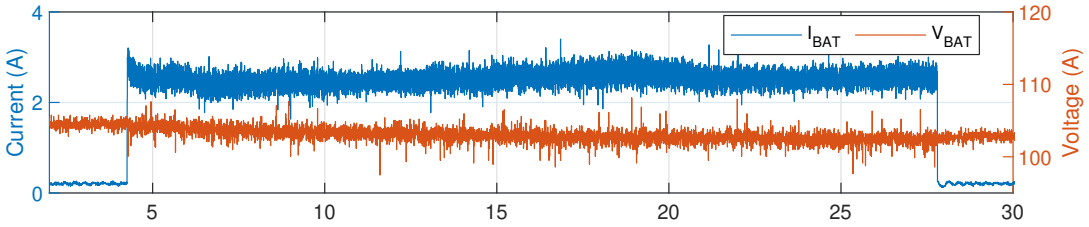

Figure 6.4: Test 1 - Battery current and voltage during V2G operation mode.

A second test was performed in which only the active power reference was varied during the experiment lasting 40 seconds. The operation mode was set to V2G and the results show stable operation in 5 different power combinations, being them 200 W, 300 W, 400 W, 500 W and 600 W.

The grid voltage and the VSI current output during operation with the aforementioned power combinations of the second test are shown in Figure 6.5. The power withdrawn from the battery and the power delivered to the grid during the second test are displayed in Figure 6.6, while Figure 6.4 shows the battery voltage and current during the test. Figure 6.9 shows the DC link voltage, proving the stable operation in the test conditions.

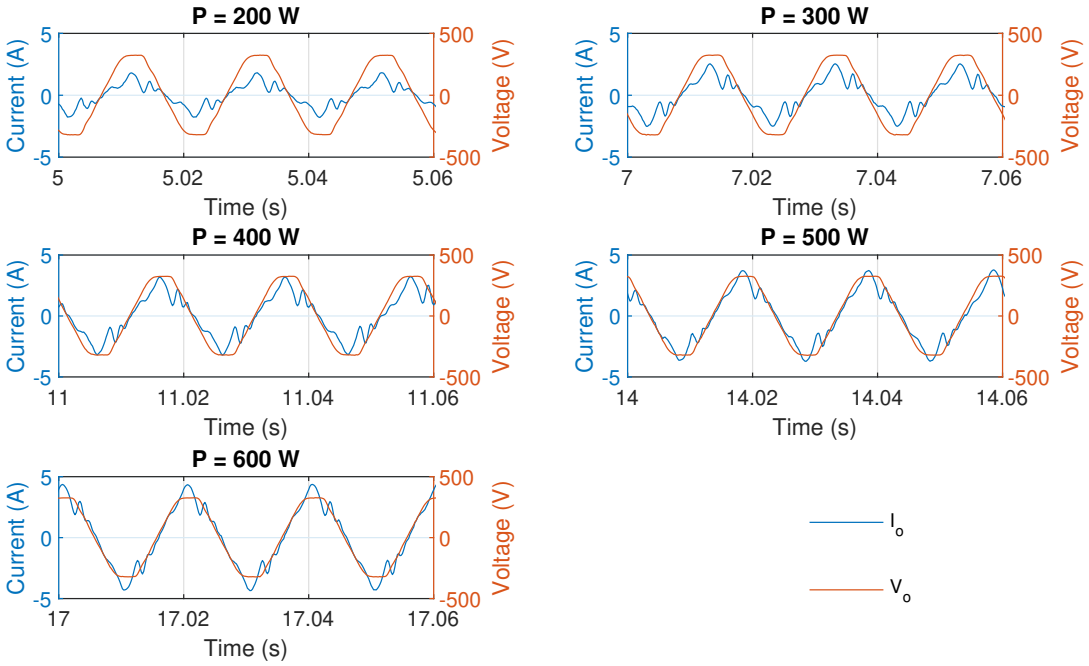

Figure 6.5: Test 2 - Output current and grid voltage during V2G operation mode.

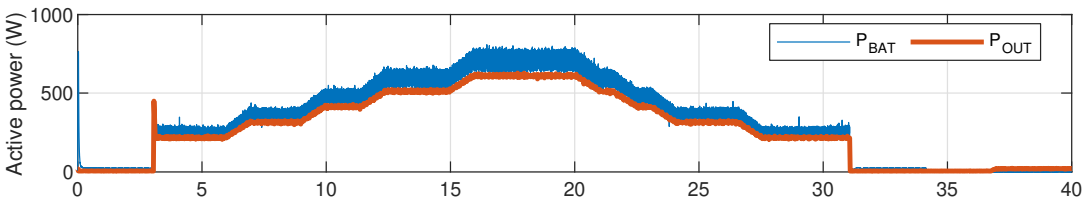

Figure 6.6: Test 2 - Battery and output power during V2G operation mode.

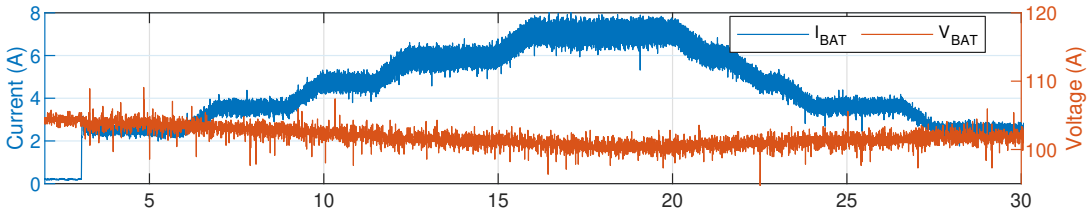

Figure 6.7: Test 2 - Battery current and voltage during V2G operation mode.

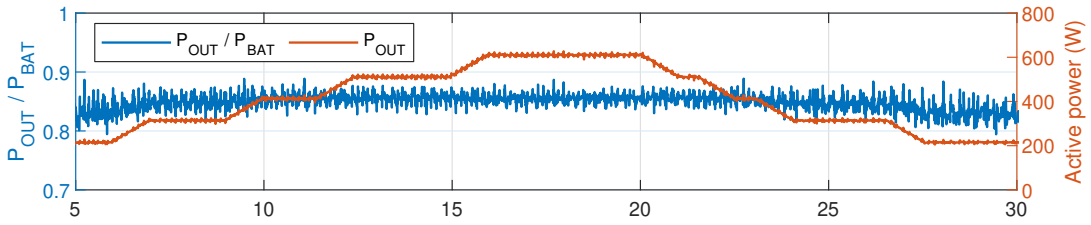

Figure 6.8: Test 2 - Calculated efficiency - $P_{\mathrm{OUT}}/P_{\mathrm{BATT}}$ - and power output during V2G operation mode.

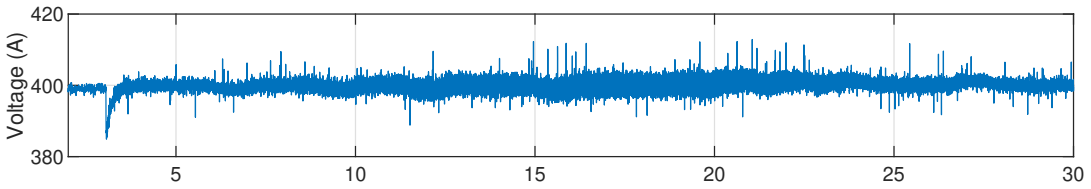

Figure 6.9: Test 2 - DC link voltage during V2G operation mode.

6.1.2 Grid-to-Vehicle (G2V) mode

In this third test the operation mode was set to G2V and the active power references were varied by varying the battery charging current reference during the experiment, which lasts for 50 seconds. The results seen in Figure 6.10 show stable operation in different power combinations, being them:

- The active power references are determined by the chosen battery charging current, which were: -1,5 A, -2 A, -2,5 A and -3 A. Since the battery voltage is approximately 100 V, the power withdrawn from the grid corresponds to -150 W, -200 W, -250 W and -300 W.

Figures 6.11, 6.12 and 6.13 show relevant system measurements, battery and grid power, battery voltage and current and DC link voltage, respectively, to prove the system stability in these power combinations.

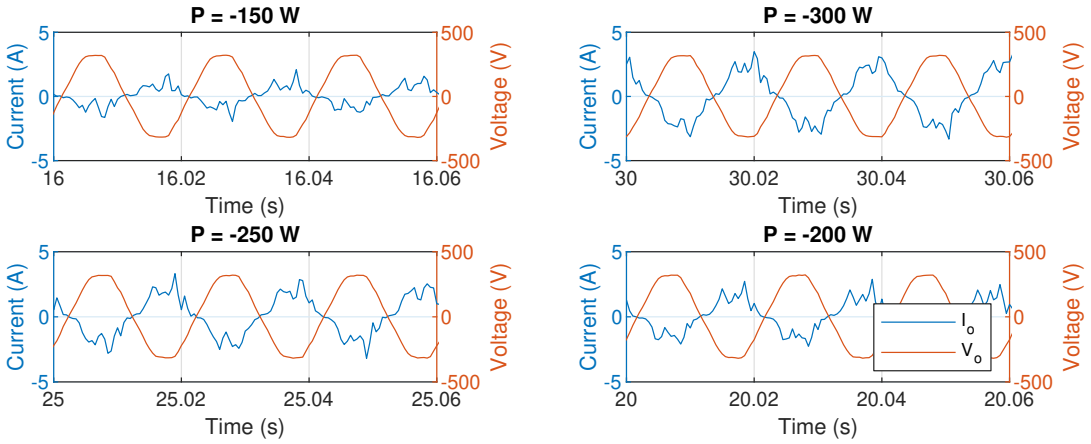

Figure 6.10: Test 3 - Output current and grid voltage during G2V operation mode with manually set charging currents of -1 A, -1,5 A, -2 A, -2,5 A and -3 A.

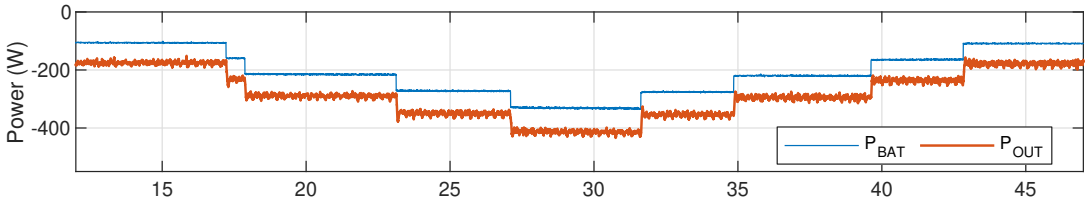

Figure 6.11: Test 3 - Power extracted from the grid and injected into the battery during G2V operation mode with manually set charging currents of -1 A, -1,5 A, -2 A, -2,5 A and -3 A.

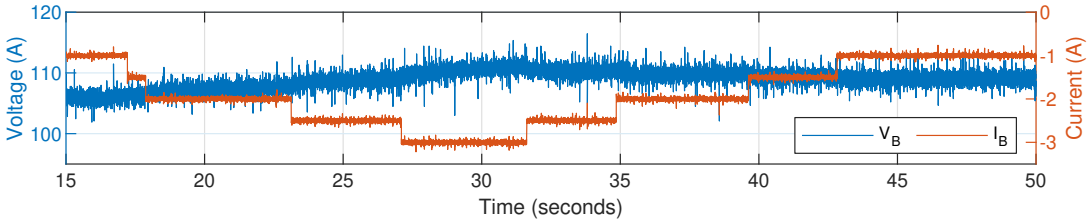

Figure 6.12: Test 3 - Battery voltage and current during G2V operation mode with manually set charging currents of -1 A, -1,5 A, -2 A, -2,5 A and -3 A.

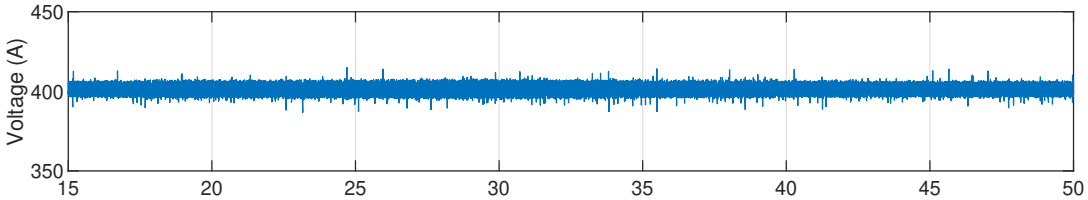

Figure 6.13: Test 3 - DC link voltage during G2V operation mode with manually set charging currents of -1 A, -1,5 A, -2 A, -2,5 A and -3 A.

6.1.3 Operation mode change

A fourth test was performed to evaluate the system stability during transitions between different operation modes while in grid-connected mode, that is, G2V and V2G. Figure 6.14 shows the grid voltage and output current, Figure 6.15 the battery current (in blue) and battery voltage (in red), Figure 6.16 the battery and grid power and Figure 6.17 the DC link voltage during a transition between V2G and G2V.

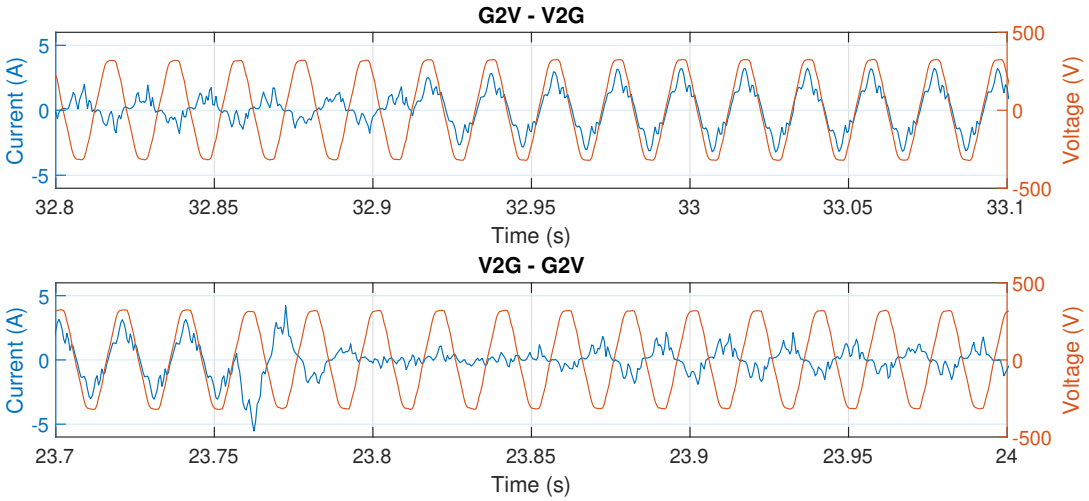

Figure 6.14: Test 4 - Output current and grid voltage during transitions between operation modes.

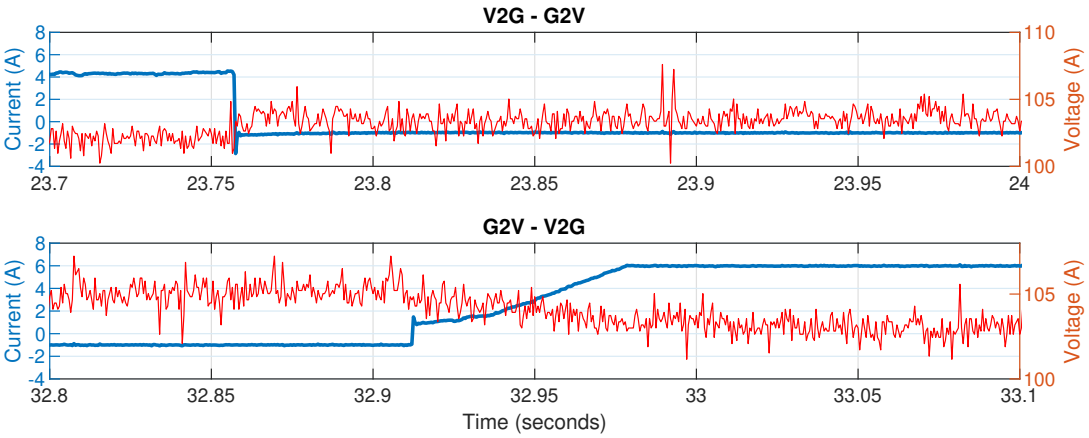

Figure 6.15: Test 4 - Battery voltage and current during transitions between operation modes.

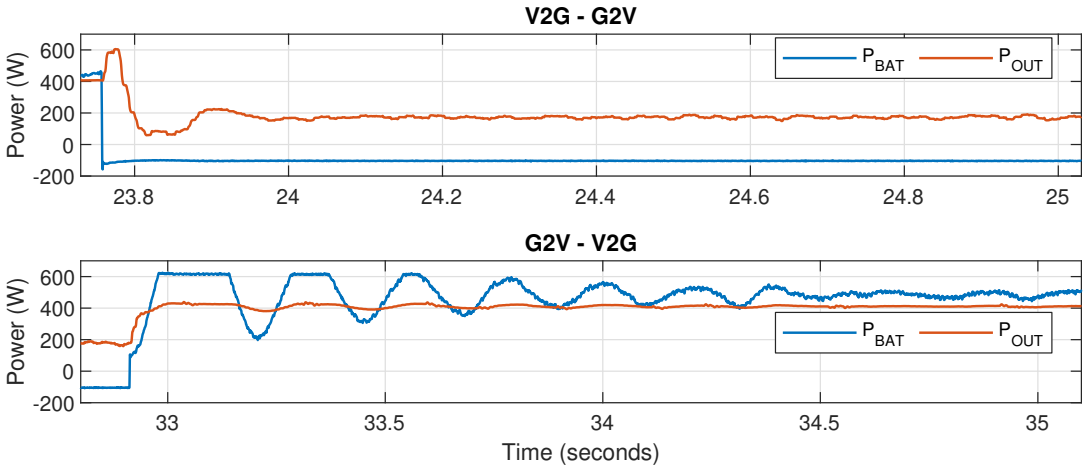

Figure 6.16: Test 4 - Battery and grid power during transitions between operation modes.

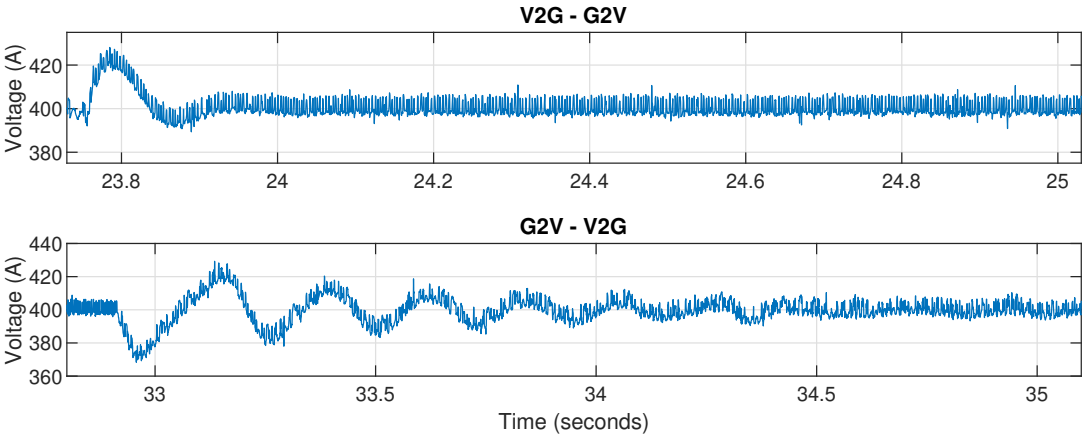

Figure 6.17: Test 4 - DC link voltage during transitions between operation modes.

Chapter 7

Discussion and Analysis

Based on Figures 5.9 and 6.1 which show the system operating in V2G mode respectively in the simulation and experimentally, the system is stable and performs well in different power combinations when operating in V2G mode, being able to deliver active power to the grid by request of an external user, as well as inject or consume reactive power, feature which allows the system to be used as an active power factor correction device. Since the reactive power is set externally, the addition of a closed-loop control, in which the current reactive power consumed in a microgrid is controlled, should allow the system to correct a microgrid power factor and raise it to within the allowed or desired limits.

This manual reactive power control is also possible when the system operates in G2V mode, that is, charging the battery, as evidenced by Figure 5.12 that shows the system operating in G2V mode in simulation with different reactive power references. G2V mode was also tested experimentally by defined the charging current manually. The reactive power references in this test were not varied and a null reactive power was set instead, as displayed in Figure 6.10, that shows G2V operation with different active power consumption to charge the battery with the physical system. This G2V feature is proposed by Leite, Ferreira, and Batista [54], lacking however experimental validation. Pinto, Monteiro, Gonçalves, *et al.* [52] on the other hand validate G2V operation experimentally.

With a higher-hierarchical control algorithm a number of optimization techniques could be used to, for example, charge the battery in certain day periods when energy is cheaper, as described in the introduction, and feed energy back to the grid when demand is higher, thus helping stabilizing the grid and providing revenue to the EV owner if the power delivered is counted and a proportional monetary compensation is predicted in a V2G contract. This could also be useful in a home microgrid with renewable energy sources, although its usefulness

depends heavily on vehicle usage, for example if it stays mostly parked in a garage or on the road and also on factors determined externally by the user, such as desired minimum state of charge, depth of discharge and battery state of health.

The operation mode of the system can also be selected manually, with the system possessing smooth transition capabilities as evidenced by the obtained simulation results in Figures 5.15 and 5.16 - showing the system behaviour in simulation during the transition between the grid-connected operation modes (V2G and G2V) - and the experimental results as visible in Figures 6.14, 6.15 and 6.16 that show the system behaviour in the experimental setup during the transition between grid-connected operation modes as well. While [52] validates their system experimentally operating in three modes - V2G, G2V and V2H, the transition between them is not shown in simulation or experimental tests.

Given that the main features of the system are all set externally - power exchange and operation mode - the proposed system allows complete control from an external entity and thus enables the development and test of different strategies in a context where multiple vehicles of different battery specifications are controlled by an aggregator system, for example. Another advantage of the proposed system is the simulation and experimental validation of the whole structure, containing a DC/DC and DC/AC converter, unlike the structure presented by Vittorias, Metzger, Kunz, *et al.* in which only a DC/AC converter is shown and the operation modes and the transitions are simulated or [56] which contains both converters, but is only validated with simulation and does not explain the operation mode transitions.

An improvement that could be made is using a better current filter to reduce the level of harmonic distortion, since the system presents a high harmonic content when the injected or withdrawn current amplitude is small. Another option is usage of more complex control systems, such as proportional-resonant control algorithms.

The total harmonic distortion was not however exactly quantified and thus compliance of the system with international norms was not assessed. It must also be taken into account that, by changing the filter values, the system dynamics change and thus parameters adjustments are required, for example the PI controllers gains. The efficiency value calculated and shown in Figure 6.8, although a low value compared to other more advanced power topologies

and control algorithms, might be explained by the test with low power ratings. Commercial inverters operate with higher efficiency close to nominal power and, given that the power module has a nominal current value of 75 A and tests with power references up to only 600 W were performed and high values of duty cycles were used for DC/DC converter control, the low efficiency rating is justified.

Operation in grid-isolated mode (V2H) was not tested experimentally unlike in [52], instead relying on the simulation results to validate the proposed V2H mode. With the addition of a controlled switch - a controlled relay, for example - the physical implementation of this operation mode and the proposed re-synchronization strategy, which is not shown in [52], is possible.

The system can be scaled to supply different power ranges, since the control can be applied to similar power structures with a higher power rating, higher battery voltages and, with a few changes, supply a three-phase current, enabling even higher power outputs. In this case another PLL strategy would be required for grid synchronization. Concerning the PLL there are also methods to improve the conversion of a single-phase current to its $\alpha\beta$ components, usually performed by applying a phase-shift delay that, while functional, compromises the dynamic response of the system current controllers.

Chapter 8

Conclusions

The implementation of a single phase bidirectional power interface between an electric vehicle battery and the grid was successful, based on the achieved computational and experimental results presented in this document. Tests were performed both in the simulation and with the experimental setup to extensively test the system and prove it is stable under different operation conditions and with varying power references, as well as dealing well with external requests or events such as mode transitions or grid faults.

While experimental validation of the grid-forming (V2H) mode is not presented in this document, all the proposed system features were validated via simulation with Simulink, including the transition between operation modes, the grid re-synchronization strategy for grid reconnection, fault detection module and operation in grid-connected modes (V2G and G2V).

Despite not being one of the initial objectives, operation in V2G or G2V modes allows for manual definition of the reactive powers to be extracted or delivered to the grid. In this scenario, the system essentially behaves as a reactive power compensation device. This additional feature was tested via simulation with varying reactive power references as well as in V2G mode with the experimental setup.

In G2V mode the system also counts with a battery charging algorithm. This algorithm follows a constant-current and constant-voltage charging scheme and was validated in simulation as well. With the experimental setup only the constant-current charging mode was tested and validated, however, since the constant-voltage charging scheme merely compares the battery voltage with a set-point and generates a current reference, the experimental validation with a manually set current reference proves the feasibility of the constant-voltage charging scheme as well.

A simulation-validated system in which all these features are packed together, that is, battery charging (G2V), V2G, V2H and reactive power compensation, is not found in any of the literature cited within this document.

The system was tested using a real-time controller board from dSPACE. On one hand this controller allows for rapid control prototyping, on the other hand it does not reflect the actual implementation of such a system for commercial purposes. For this scenario, the control has to be implemented with a micro-controller or a DSP.

Experimental validation further corroborates the results found via simulation, showing that a physical implementation of the system with the proposed control algorithms is feasible, robust and able to effectively control the power flow between a battery and the electric grid, thus reaching the main thesis objective.

8.1 Future work

This section contains suggestions on future lines of research related to the topic at hand, with the objective of further improving and testing of the proposed bidirectional interface between vehicle and grid.

- Experimental validation with higher power outputs and operation in grid-isolated (V2H) mode;
- PI controller parameters tuning to achieve a better dynamic performance during transitions between operating modes;
- Usage of proportional-resonant controllers for harmonics compensation.

References

[1] J. Stewart, *BBC Future - Can a city really ban cars from its streets?* [Online]. Available: http://www.bbc.com/future/story/20140204-can-a-city-really-go-car-free (visited on Mar. 19, 2019).

[2] P. Oltermann, *The Guardian - Hamburg becomes first German city to ban older diesel cars*. [Online]. Available: https://www.theguardian.com/world/2018/may/23/hamburg-first-german-city-ban-older-diesel-cars-air-quality-pollution (visited on Mar. 19, 2019).

[3] M. McGrath, *BBC - Four major cities move to ban diesel vehicles by 2025*. [Online]. Available: https://www.bbc.com/news/science-environment-38170794 (visited on Mar. 19, 2019).

[4] M. Åhman, "Government policy and the development of electric vehicles in Japan", *Energy Policy*, vol. 34, no. 4, pp. 433 –443, 2006, ISSN: 0301-4215. DOI: https://doi.org/10.1016/j.enpol.2004.06.011.

[5] Clean Energy Ministerial, *About the Clean Energy Ministerial | Drupal*. [Online]. Available: http://www.cleanenergyministerial.org/about-clean-energy-ministerial (visited on Oct. 8, 2018).

[6] International Energy Agency, *Electric Vehicles Initiative (EVI)*. [Online]. Available: https://www.iea.org/topics/transport/evi/ (visited on Oct. 8, 2018).

[7] Nationale Plattform Elektromobilität, *Die Ziele | Nationale Plattform Elektromobilität*. [Online]. Available: http://nationale-plattform-elektromobilitaet.de/ (visited on Nov. 20, 2018).

[8] Bundesministerium für Umwelt, Naturschutz und nukleare Sicherheit, *Sigmar Gabriel: Klimaschutz nutzt auch Verbrauchern und Wirtschaft*. [Online]. Available: https://www.bmu.de/pressemitteilung/sigmar-gabriel-klimaschutz-nutzt-auch-verbrauchern-und-wirtschaft/ (visited on Nov. 20, 2018).

[9] P. Pinto, *MOBI.E: 400 postos de carregamento de veículos elétricos com energia Galp*. [Online]. Available: https://pplware.sapo.pt/informacao/galp-vai-fornecer-eletricidade-a-rede-publica-de-veiculos-eletricos/ (visited on Nov. 24, 2018).

[10] Inteli, *MOBI.E*. [Online]. Available: http://www.inteli.pt/pt/go/mobie (visited on Nov. 24, 2018).

[11] Prefeitura da Cidade de São Paulo, *Diário Oficial da Cidade de São Paulo, Lei Ordinária Número 15.997*, 2014.

[12] R. Garcia and M. Briet, *Veículos elétricos ganham incentivos e podem deixar a cidade mais silenciosa e menos poluída*. [Online]. Available: http://www.saopaulo.sp.leg.br/apartes-anteriores/revista-apartes/numero-17/a-toda-carga/ (visited on Jan. 8, 2019).

[13] International Energy Agency, *Global EV Outlook 2018: towards cross-modal electrification*, 2018. [Online]. Available: https://webstore.iea.org/global-ev-outlook-2018 (visited on Oct. 9, 2018).

[14] ——, *GEVO - Key Findings*, 2018. [Online]. Available: https://www.iea.org/gevo2018/ (visited on Nov. 24, 2018).

[15] N. Nitta, F. Wu, J. T. Lee, and G. Yushin, "Li-ion battery materials: Present and future", *Materials Today*, vol. 18, no. 5, pp. 252 –264, 2015, ISSN: 1369-7021. DOI: https://doi.org/10.1016/j.mattod.2014.10.040.

[16] B. Nykvist and M. Nilsson, "Rapidly falling costs of battery packs for electric vehicles", vol. 5, pp. 329–332, Mar. 2015.

[17] Eurostat, *Share of renewable energy in gross final energy consumption.* [Online]. Available: https://ec.europa.eu/eurostat/tgm/table.do?tab=table&plugin=1&language=en&pcode=t2020_31 (visited on Nov. 26, 2018).

[18] P. Denholm, M. O'Connell, G. Brinkman, and J. Jorgenson, "Overgeneration from Solar Energy in California: A Field Guide to the Duck Chart", National Renewable Energy Laboratory, Tech. Rep., 2015.

[19] J. St-John, *Hawaii's Solar-Grid Landscape and the 'Nessie Curve'.* [Online]. Available: https://www.greentechmedia.com/articles/read/hawaiis-solar-grid-landscape-and-the-nessie-curve (visited on Dec. 5, 2018).

[20] N. Reimer, *Lausitz: Ohne Kohle in Cottbus | ZEIT ONLINE.* [Online]. Available: https://www.zeit.de/wirtschaft/2018-07/lausitz-cottbus-kohleausstieg-braunkohle-gaskraftwerk (visited on Jan. 17, 2019).

[21] The Guardian, *Canada plans to phase out coal-powered electricity by 2030 | World news.* [Online]. Available: https://www.theguardian.com/world/2016/nov/21/canada-coal-electricity-phase-out-2030 (visited on Jan. 17, 2019).

[22] M. A. Gonzalez-Salazar, T. Kirsten, and L. Prchlik, "Review of the operational flexibility and emissions of gas- and coal-fired power plants in a future with growing renewables", *Renewable and Sustainable Energy Reviews*, vol. 82, pp. 1497 –1513, 2018, ISSN: 1364-0321. DOI: https://doi.org/10.1016/j.rser.2017.05.278.

[23] B. Matek, "Flexible opportunities with geothermal technology: Barriers and opportunities", *The Electricity Journal*, vol. 28, no. 9, pp. 45 –51, 2015, ISSN: 1040-6190. DOI: https://doi.org/10.1016/j.tej.2015.09.020.

[24] C. Wahlquist, *South Australia's Tesla battery on track to make back a third of cost in a year.* [Online]. Available: https://www.theguardian.com/technology/2018/sep/27/south-australias-tesla-battery-on-track-to-make-back-a-third-of-cost-in-a-year (visited on Dec. 2, 2018).

[25] M. Galkin-Aalto, *Electricity storage facility.* [Online]. Available: https://www.helen.fi/en/news/2016/electricity-storage-facility/ (visited on Dec. 3, 2018).

[26] J. Coignard, S. Saxena, J. Greenblatt, and D. Wang, "Clean vehicles as an enabler for a clean electricity grid", *Environmental Research Letters*, vol. 13, no. 5, p. 054 031, May 2018. DOI: 10.1088/1748-9326/aabe97. [Online]. Available: https://doi.org/10.1088\%2F1748-9326\%2Faabe97.

[27] *Solar PV Systems - SOLA - Solar Company Cape Town | JHB | Africa.* [Online]. Available: https://i0.wp.com/www.solafuture.co.za/wp-content/uploads/2018/02/Peak-shaving-graph.png?ssl=1 (visited on Jun. 19, 2019).

[28] Nissan, *Nissan LEAF to help stabilize German electricity grid - Global Newsroom.* [Online]. Available: https://newsroom.nissan-global.com/releases/nissan-leaf-to-help-stabilize-german-electricity-grid (visited on Dec. 9, 2018).

[29] B. K. Sovacool, J. Axsen, and W. Kempton, "The Future Promise of Vehicle-to-Grid (V2G) Integration: A Sociotechnical Review and Research Agenda", *Annual Review of Environment and Resources*, vol. 42, no. 1, pp. 377–406, 2017. DOI: 10.1146/annurev-environ-030117-020220.

[30] Nissan, *Vehicle to Home Electricity Supply System.* [Online]. Available: https://www.nissan-global.com/EN/TECHNOLOGY/OVERVIEW/vehicle_to_home.html (visited on May 25, 2019).

[31] D. P. Tuttle, R. L. Fares, R. Baldick, and M. E. Webber, "Plug-in vehicle to home (V2H) duration and power output capability", in *2013 IEEE Transportation Electrification Conference and Expo (ITEC)*, Jun. 2013, pp. 1–7. DOI: 10.1109/ITEC.2013.6574527.

[32] W. Kempton and S. E. Letendre, "Electric vehicles as a new power source for electric utilities", *Transportation Research Part D: Transport and Environment*, vol. 2, no. 3, pp. 157 –175, 1997, ISSN: 1361-9209. DOI: https://doi.org/10.1016/S1361-9209(97)00001-1.

[33] M. Ferdowsi, "Plug-in hybrid vehicles - a vision for the future", in *2007 IEEE Vehicle Power and Propulsion Conference*, Sep. 2007, pp. 457–462. DOI: 10.1109/VPPC.2007.4544169.

[34] K. M. Tan, V. K. Ramachandaramurthy, and J. Y. Yong, "Integration of electric vehicles in smart grid: A review on vehicle to grid technologies and optimization techniques", *Renewable and Sustainable Energy Reviews*, vol. 53, pp. 720 –732, 2016, ISSN: 1364-0321. DOI: https://doi.org/10.1016/j.rser.2015.09.012.

[35] B. K. Sovacool, L. Noel, J. Axsen, and W. Kempton, "The neglected social dimensions to a vehicle-to-grid (V2G) transition: a critical and systematic review", *Environmental Research Letters*, vol. 13, no. 1, p. 013 001, Jan. 2018. DOI: 10.1088/1748-9326/aa9c6d.

[36] F. Mwasilu, J. J. Justo, E.-K. Kim, T. D. Do, and J.-W. Jung, "Electric vehicles and smart grid interaction: A review on vehicle to grid and renewable energy sources integration", *Renewable and Sustainable Energy Reviews*, vol. 34, pp. 501 –516, 2014, ISSN: 1364-0321. DOI: https://doi.org/10.1016/j.rser.2014.03.031.

[37] G. R. Parsons, M. K. Hidrue, W. Kempton, and M. P. Gardner, "Willingness to pay for vehicle-to-grid (V2G) electric vehicles and their contract terms", *Energy Economics*, 2014, ISSN: 01409883. DOI: 10.1016/j.eneco.2013.12.018.

[38] J. Geske and D. Schumann, "Willing to participate in vehicle-to-grid (V2G)? why not!", *Energy Policy*, vol. 120, pp. 392 –401, 2018, ISSN: 0301-4215. DOI: https://doi.org/10.1016/j.enpol.2018.05.004.

[39] W. Kempton and J. Tomić, "Vehicle-to-grid power fundamentals: Calculating capacity and net revenue", *Journal of Power Sources*, vol. 144, no. 1, pp. 268 –279, 2005, ISSN: 0378-7753. DOI: https://doi.org/10.1016/j.jpowsour.2004.12.025.

[40] H. N. T. Nguyen, C. Zhang, and M. A. Mahmud, "Optimal coordination of G2V and V2G to support power grids with high penetration of renewable energy", *IEEE Transactions on Transportation Electrification*, vol. 1, no. 2, pp. 188–195, Aug. 2015, ISSN: 2332-7782. DOI: 10.1109/TTE.2015.2430288.

[41] H. Krueger and A. Cruden, "Modular strategy for aggregator control and data exchange in large scale vehicle-to-grid (v2g) applications", *Energy Procedia*, vol. 151, pp. 7 –11, 2018, 3rd Annual Conference in Energy Storage and Its Applications, 3rd CDT-ESA-AC, 11–12 September 2018, The University of Sheffield, UK, ISSN: 1876-6102. DOI: https://doi.org/10.1016/j.egypro.2018.09.019.

[42] Z. Liu, D. Wang, H. Jia, N. Djilali, and W. Zhang, "Aggregation and bidirectional charging power control of plug-in hybrid electric vehicles: Generation system adequacy analysis", *IEEE Transactions on Sustainable Energy*, vol. 6, no. 2, pp. 325–335, Apr. 2015, ISSN: 1949-3029. DOI: 10.1109/TSTE.2014.2372044.

[43] A. W. Thompson, "Economic implications of lithium ion battery degradation for Vehicle-to-Grid (V2X) services", *Journal of Power Sources*, vol. 396, pp. 691 –709, 2018, ISSN: 0378-7753. DOI: https://doi.org/10.1016/j.jpowsour.2018.06.053.

[44] S. B. Peterson, J. Apt, and J. Whitacre, "Lithium-ion battery cell degradation resulting from realistic vehicle and vehicle-to-grid utilization", *Journal of Power Sources*, vol. 195, no. 8, pp. 2385 –2392, 2010, ISSN: 0378-7753. DOI: https://doi.org/10.1016/j.jpowsour.2009.10.010.

[45] D. Wang, J. Coignard, T. Zeng, C. Zhang, and S. Saxena, "Quantifying electric vehicle battery degradation from driving vs. vehicle-to-grid services", *Journal of Power Sources*, vol. 332, pp. 193 –203, 2016, ISSN: 0378-7753. DOI: https://doi.org/10.1016/j.jpowsour.2016.09.116.

[46] J. D. Bishop, C. J. Axon, D. Bonilla, M. Tran, D. Banister, and M. D. McCulloch, "Evaluating the impact of V2G services on the degradation of batteries in PHEV and EV", *Applied Energy*, vol. 111, pp. 206 –218, 2013, ISSN: 0306-2619. DOI: https://doi.org/10.1016/j.apenergy.2013.04.094.

[47] M. Dubarry, A. Devie, and K. McKenzie, "Durability and reliability of electric vehicle batteries under electric utility grid operations: Bidirectional charging impact analysis", *Journal of Power Sources*, vol. 358, pp. 39 –49, 2017, ISSN: 0378-7753. DOI: https://doi.org/10.1016/j.jpowsour.2017.05.015.

[48] K. Uddin, M. Dubarry, and M. B. Glick, "The viability of vehicle-to-grid operations from a battery technology and policy perspective", *Energy Policy*, vol. 113, pp. 342 –347, 2018, ISSN: 0301-4215. DOI: https://doi.org/10.1016/j.enpol.2017.11.015.

[49] A. Marongiu, M. Roscher, and D. U. Sauer, "Influence of the vehicle-to-grid strategy on the aging behavior of lithium battery electric vehicles", *Applied Energy*, vol. 137, pp. 899 –912, 2015, ISSN: 0306-2619. DOI: https://doi.org/10.1016/j.apenergy.2014.06.063.

[50] K. Uddin, T. Jackson, W. D. Widanage, G. Chouchelamane, P. A. Jennings, and J. Marco, "On the possibility of extending the lifetime of lithium-ion batteries through optimal V2G facilitated by an integrated vehicle and smart-grid system", *Energy*, vol. 133, pp. 710 –722, 2017, ISSN: 0360-5442. DOI: https://doi.org/10.1016/j.energy.2017.04.116.

[51] A. Sharma and S. Sharma, "Review of power electronics in vehicle-to-grid systems", *Journal of Energy Storage*, vol. 21, pp. 337 –361, 2019, ISSN: 2352-152X. DOI: https://doi.org/10.1016/j.est.2018.11.022.

[52] J. G. Pinto, V. Monteiro, H. Gonçalves, B. Exposto, D. Pedrosa, C. Couto, and J. L. Afonso, "Bidirectional battery charger with grid-to-vehicle, vehicle-to-grid and vehicle-to-home technologies", in *IECON 2013 - 39th Annual Conference of the IEEE Industrial Electronics Society*, Nov. 2013, pp. 5934–5939. DOI: 10.1109/IECON.2013.6700108.

[53] M. Jang, M. Ciobotaru, and V. G. Agelidis, "A compact single-phase bidirectional buck-boost-inverter topology", in *2012 International Conference on Renewable Energy Research and Applications (ICRERA)*, Nov. 2012, pp. 1–6. DOI: 10.1109/ICRERA.2012.6477308.

[54] V. Leite, A. Ferreira, and J. Batista, "Bidirectional vehicle-to-grid interface under a microgrid project", in *2014 IEEE 15th Workshop on Control and Modeling for Power Electronics (COMPEL)*, Jun. 2014, pp. 1–7. DOI: 10.1109/COMPEL.2014.6877175.

[55] I. Vittorias, M. Metzger, D. Kunz, M. Gerlich, and G. Bachmaier, "A bidirectional battery charger for electric vehicles with V2G and V2H capability and active and reactive power control", in *2014 IEEE Transportation Electrification Conference and Expo (ITEC)*, Jun. 2014, pp. 1–6. DOI: 10.1109/ITEC.2014.6861855.

[56] R. Zgheib, K. Al-Haddad, and I. Kamwa, "V2g, g2v and active filter operation of a bidirectional battery charger for electric vehicles", in *2016 IEEE International Conference on Industrial Technology (ICIT)*, Mar. 2016, pp. 1260–1265. DOI: 10.1109/ICIT.2016.7474935.

[57] M. Kwon and S. Choi, "An electrolytic capacitorless bidirectional EV charger for V2G and V2H applications", *IEEE Transactions on Power Electronics*, vol. 32, no. 9, pp. 6792–6799, Sep. 2017, ISSN: 0885-8993. DOI: 10.1109/TPEL.2016.2630711.

[58] M. Kwon, S. Jung, and S. Choi, "A high efficiency bi-directional ev charger with seamless mode transfer for v2g and v2h application", in *2015 IEEE Energy Conversion Congress and Exposition (ECCE)*, Sep. 2015, pp. 5394–5399. DOI: 10.1109/ECCE.2015.7310418.

[59] R. Teodorescu, M. Liserre, and P. Rodriguez, *Grid Converters for Photovoltaic and Wind Power Systems*, ser. Wiley - IEEE. Wiley, 2010, ISBN: 9780470667040.

[60] U. K. Madawala and D. J. Thrimawithana, "A bidirectional inductive power interface for electric vehicles in v2g systems", *IEEE Transactions on Industrial Electronics*, vol. 58, no. 10, pp. 4789–4796, Oct. 2011, ISSN: 0278-0046. DOI: 10.1109/TIE.2011.2114312.

[61] A. Narula and V. Verma, "Bi – directional trans – z source boost converter for g2v/v2g applications", in *2017 IEEE Transportation Electrification Conference (ITEC-India)*, Dec. 2017, pp. 1–6. DOI: 10.1109/ITEC-India.2017.8356947.

[62] E. dos Santos and E. da Silva, *Advanced Power Electronics Converters: PWM Converters Processing AC Voltages*, ser. IEEE Press Series on Power Engineering. Wiley, 2014, ISBN: 9781118972052.

[63] A. Ahmed, *Power Electronics for Technology*. Prentice Hall, 1999, ISBN: 9780132310697.

[64] W. C. Duesterhoeft, M. W. Schulz, and E. Clarke, "Determination of instantaneous currents and voltages by means of alpha, beta, and zero components", *Transactions of the American Institute of Electrical Engineers*, vol. 70, no. 2, pp. 1248–1255, Jul. 1951, ISSN: 0096-3860. DOI: 10.1109/T-AIEE.1951.5060554.

[65] R. H. Park, "Two-reaction theory of synchronous machines generalized method of analysis-part i", *Transactions of the American Institute of Electrical Engineers*, vol. 48, no. 3, pp. 716–727, Jul. 1929, ISSN: 0096-3860. DOI: 10.1109/T-AIEE.1929.5055275.

[66] N. S. Nise, *Control Systems Engineering, 7th Edition*. Wiley, 2015, ISBN: 9781118800829.

[67] K. Ogata, *Modern Control Engineering*, 5th ed., ser. Instrumentation and Controls Series. Prentice Hall, 2010, ISBN: 978-0-13-615673-4.

[68] K. H. Ang, G. Chong, and Y. Li, "PID control system analysis, design, and technology", *IEEE Transactions on Control Systems Technology*, vol. 13, no. 4, pp. 559–576, Jul. 2005, ISSN: 1063-6536. DOI: 10.1109/TCST.2005.847331.

[69] R. Zhang, M. Cardinal, P. Szczesny, and M. Dame, "A grid simulator with control of single-phase power converters in d-q rotating frame", in *2002 IEEE 33rd Annual IEEE Power Electronics Specialists Conference. Proceedings (Cat. No.02CH37289)*, vol. 3, Jun. 2002, 1431–1436 vol.3. DOI: 10.1109/PSEC.2002.1022377.

[70] B. Bahrani, A. Rufer, S. Kenzelmann, and L. A. C. Lopes, "Vector control of single-phase voltage-source converters based on fictive-axis emulation", *IEEE Transactions on Industry Applications*, vol. 47, no. 2, pp. 831–840, Mar. 2011, ISSN: 0093-9994. DOI: 10.1109/TIA.2010.2101992.

[71] IEEE, "Standard for Interconnection and Interoperability of Distributed Energy Resources with Associated Electric Power Systems Interfaces", *IEEE Std 1547-2018 (Revision of IEEE Std 1547-2003)*, pp. 1–138, Apr. 2018. DOI: 10.1109/IEEESTD.2018.8332112.

[72] IEC, "Photovoltaic (PV) systems – Characteristics of the utility interface", *IEC 61727:2004*, 2004.

[73] B. Kramer, S. Chakraborty, and B. Kroposki, "A review of plug-in vehicles and vehicle-to-grid capability", in *2008 34th Annual Conference of IEEE Industrial Electronics*, Nov. 2008, pp. 2278–2283. DOI: 10.1109/IECON.2008.4758312.

[74] IEC, "Standard for Testing Procedure of Islanding Prevention Measures for Grid Connected Photovoltaic Power Generation Systems", *IEC 62116:2014*, 2014.

[75] F. Noor, R. Arumugam, and M. Y. Vaziri, "Unintentional islanding and comparison of prevention techniques", in *Proceedings of the 37th Annual North American Power Symposium, 2005.*, Oct. 2005, pp. 90–96. DOI: 10.1109/NAPS.2005.1560507.

[76] A. Sharma and R. Sunitha, "Unintentional islanding detection in microgrid", in *2017 International Conference on Energy, Communication, Data Analytics and Soft Computing (ICECDS)*, Aug. 2017, pp. 2519–2523. DOI: 10.1109/ICECDS.2017.8389907.

[77] Zhihong Ye, A. Kolwalkar, Yu Zhang, Pengwei Du, and Reigh Walling, "Evaluation of anti-islanding schemes based on nondetection zone concept", *IEEE Transactions on Power Electronics*, vol. 19, no. 5, pp. 1171–1176, Sep. 2004, ISSN: 0885-8993. DOI: 10.1109/TPEL.2004.833436.

[78] W. Bower and M. Ropp, "Evaluation of islanding detection methods for utility-interactive inverters in photovoltaic systems", Jan. 2002. DOI: 10.2172/806700.

[79] S. V. Araujo, A. Engler, B. Sahan, and F. L. M. Antunes, "LCL filter design for grid-connected NPC inverters in offshore wind turbines", in *2007 7th Internatonal Conference on Power Electronics*, Oct. 2007, pp. 1133–1138. DOI: 10.1109/ICPE.2007.4692556.

[80] S. Samerchur, S. Premrudeepreechacharn, Y. Kumsuwun, and K. Higuchi, "Power control of single-phase voltage source inverter for grid-connected photovoltaic systems", in *2011 IEEE/PES Power Systems Conference and Exposition*, Mar. 2011, pp. 1–6. DOI: 10.1109/PSCE.2011.5772504.

[81] Mathworks, *Implement generic battery model - Simulink*. [Online]. Available: https://www.mathworks.com/help/physmod/sps/powersys/ref/battery.html (visited on Jun. 2, 2019).

[82] M. Ciobotaru, R. Teodorescu, and F. Blaabjerg, "A new single-phase PLL structure based on second order generalized integrator", in *2006 37th IEEE Power Electronics Specialists Conference*, Jun. 2006, pp. 1–6. DOI: 10.1109/pesc.2006.1711988.

[83] Mitsubishi Electric, *Mitsubishi <Intelligent Power Modules> PM75RLA120 Flat-Base and Insulated Package Type*. [Online]. Available: http://www.me-sh.cn/products/pdf/pm75rla120_e.pdf (visited on Jun. 19, 2019).

[84] Powerex, *BP7B –G1 Series Intelligent Power Module (IPM) Interface Circuit Reference Design*. [Online]. Available: www.pwrx.com/pwrx/docs/BP7B%20Application%20note.pdf (visited on Jun. 19, 2019).

[85] dSPACE, *ControlDesk*. [Online]. Available: https://www.dspace.com/de/gmb/home/medien/product_info/controldesk_next_generation.cfm (visited on Apr. 2, 2019).

Appendix A

Other Appendix(es)

A.1 Simulink Model

A.1.1 Parameters

Table A.1: Simulation parameters

Parameter name	Variable name	Value	Unit
Simulations parameters			
Step time	step_time	2,00E-06	s
	real_ts	1,00E-04	s
Grid parameters			
Amplitude	grid_amplitude	325,27	V
Frequency	grid_frequency	50	Hz
Grid filter			
Filter resistance	R_grid	0,67	Ω
Filter inductance	H_grid	5,6-03	H
Filter capacitance	C_grid	1,00E-06	F
DC bus parameters			
DC bus voltage reference	v_DCBus_ref	400	V
Capacitance	C_DC	1,00E-03	F
Initial capacitor voltage	C_DC_init_voltage	400	V
Battery parameters			
Nominal voltage	V_bat	96	V
Nominal capacity	Ah_bat	20	Ah

Table A.1 continued from previous page

Parameter name	Variable name	Value	Unit
Initial state of charge	SOCi_bat	90	%
Parallel capacitor value	-	0,5E-6	F
Series inductance value	-	12E-3	H
Series inductance resistance value	-	0,45	Ω
PI controllers - dq Currents - Parameters			
Proportional gain	kp_iS	20	-
Integrative gain	ki_iS	30	-
PI controllers - VDC - V2G - Parameters			
Proportional gain	kp_vDC_V2G	0,2	-
Integrative gain	ki_vDC_V2G	10	-
PI controllers - VDC - G2V - Parameters			
Proportional gain	kp_vDC_G2V	0,1	-
Integrative gain	ki_vDC_G2V	10	-
PI controllers - Battery current - Parameters			
Proportional gain	kp_bb	0,1	-
Integrative gain	ki_bb	5	-
PLL parameters			
PLL sampling time	pll_sampling_time	2,00E-06	s
	kSogi	0,2	
	kom	0,2	
Physical parameters			
PWM switching frequency	f_switching	10,0E+03	Hz
PWM sampling time	pwm_sample_time	2,00E-06	s
Inductance	L	5,60E-03	H

A.1.2 Phase-Locked Loop (PLL)

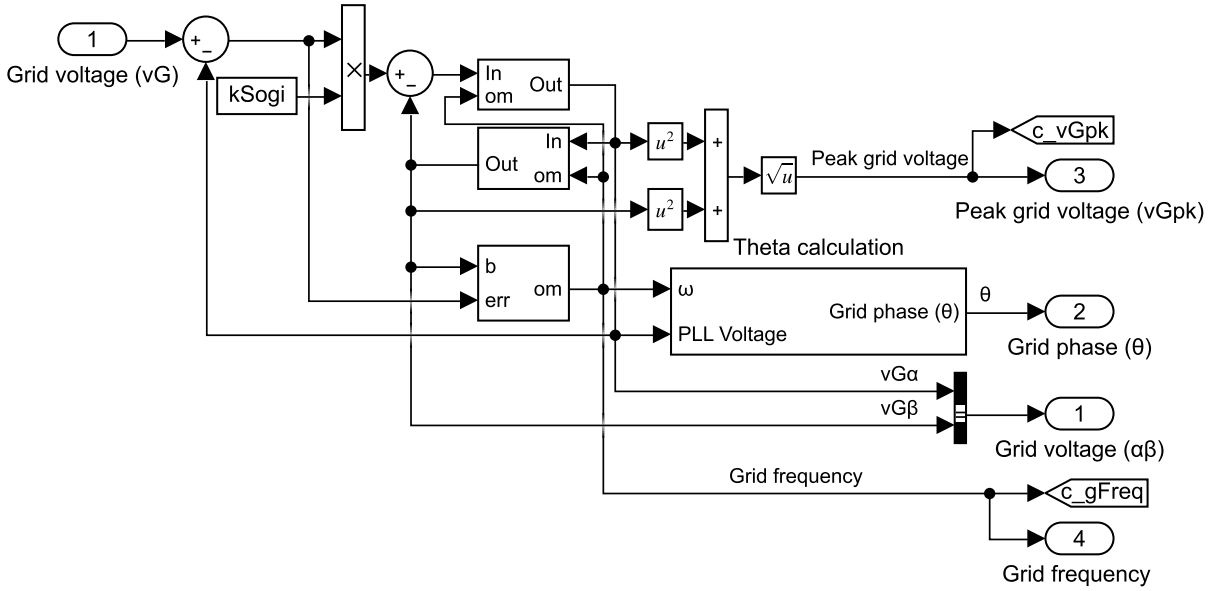

Figure A.1: Grid voltage phase-locked loop (PLL) in SImulink

A.1.3 Control overview

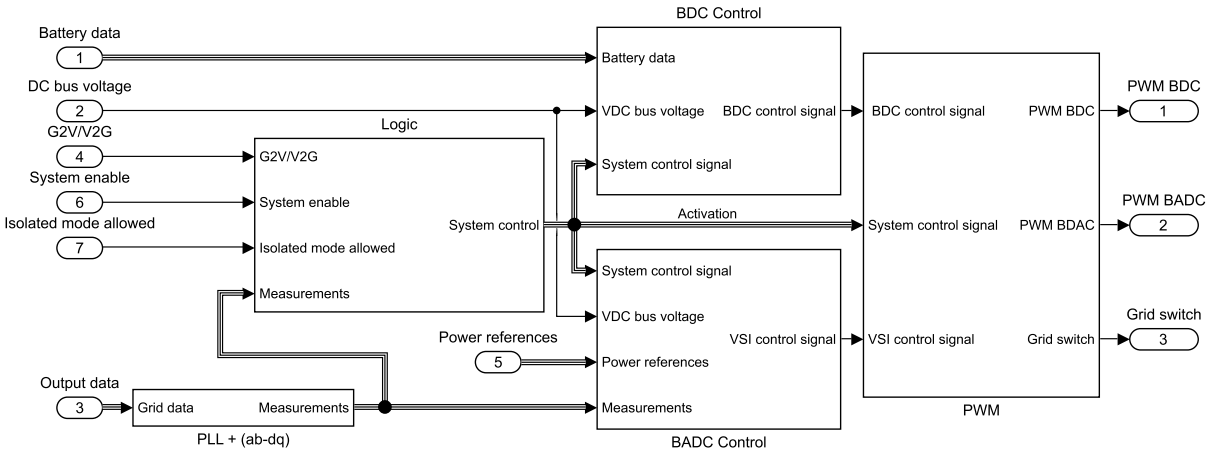

Figure A.2: Control structure in Simulink showing the BDC and BADC control, the PWM generator and the logic controller

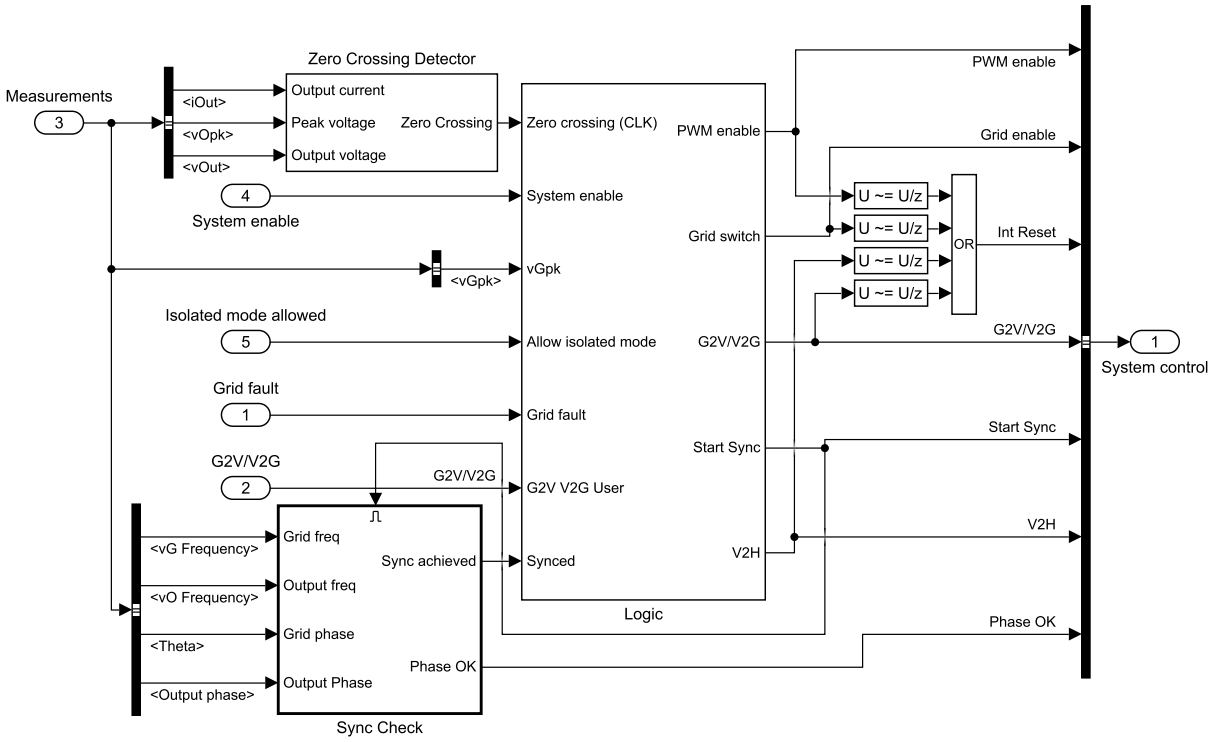

Figure A.3: Logic control overview

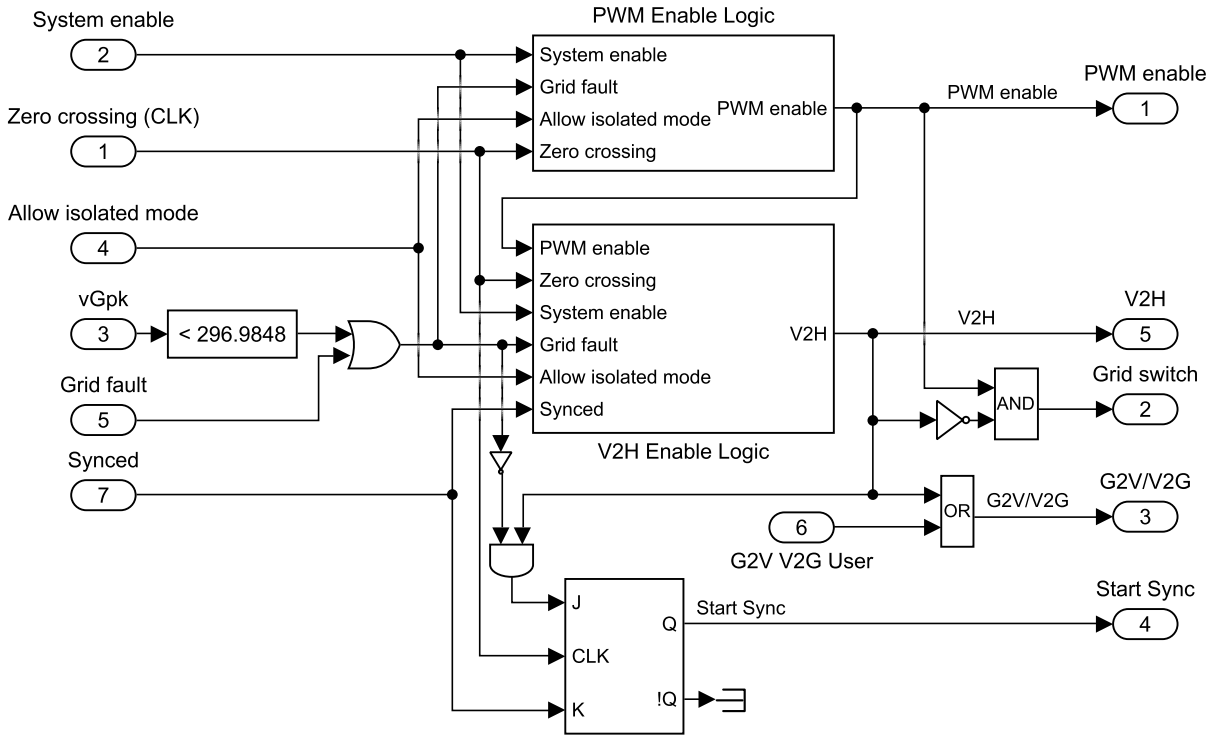

Figure A.4: Logic to determine mode of operation and manage the transition between grid-isolated and grid-tied modes

A.1.4 BADC control overview

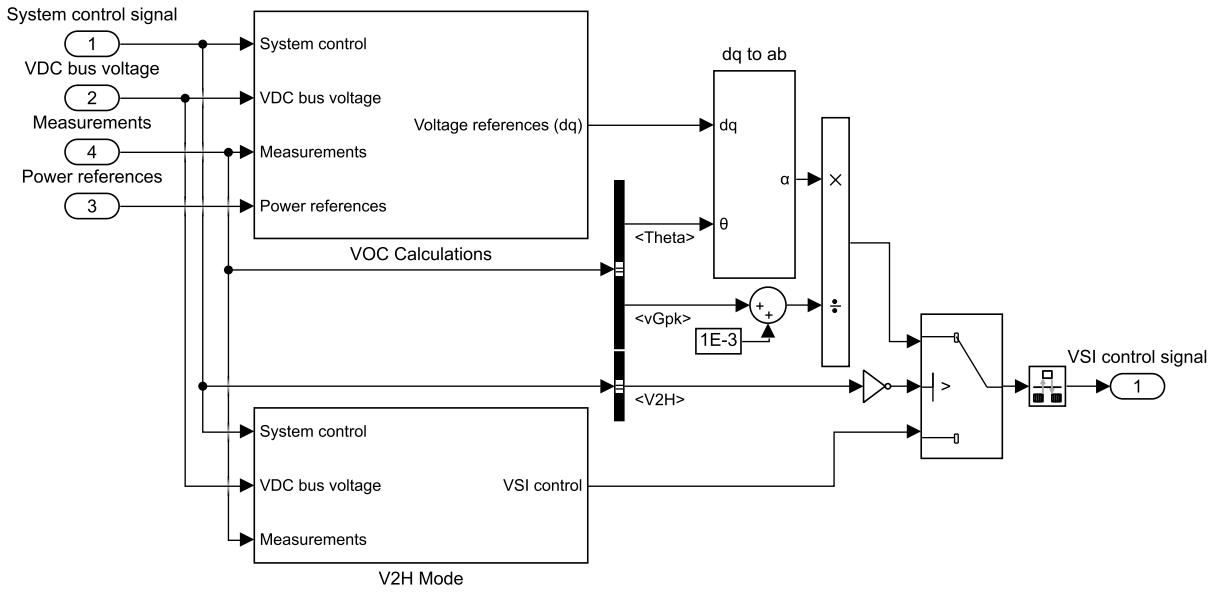

Figure A.5: BADC control diagram in Simulink showing the VOC and V2H control modes

A.1.5 Voltage-oriented Control

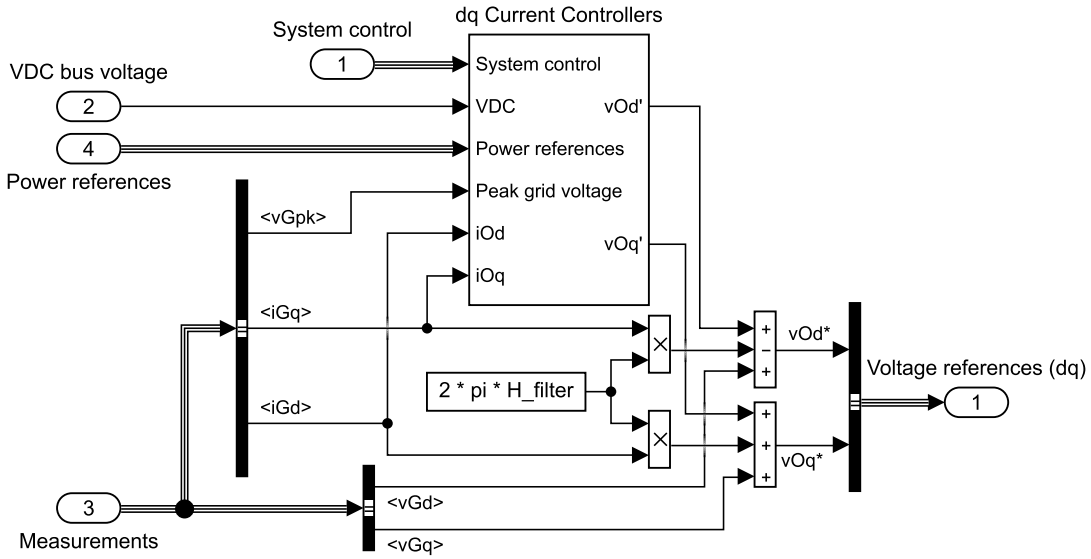

Figure A.6: Voltage-oriented control calculations to generate V_d^* and V_q^*

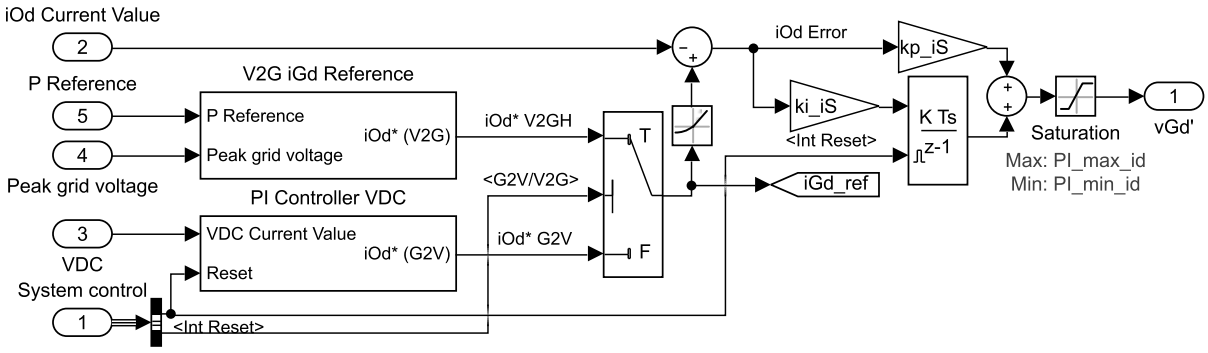

Figure A.7: Output current *d*-component controller

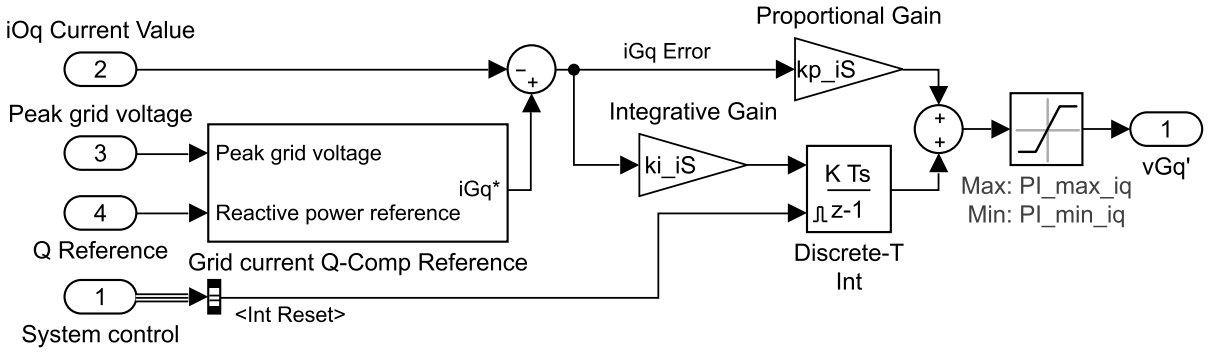

Figure A.8: Output current *q*-component controller

A.1.6 Vehicle-to-Home - Grid-isolated

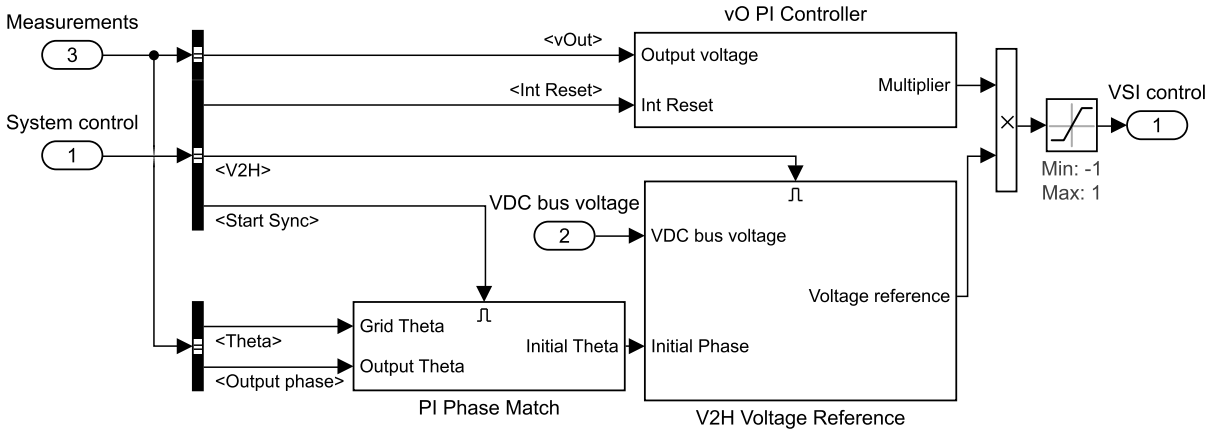

Figure A.9: V2H control overview

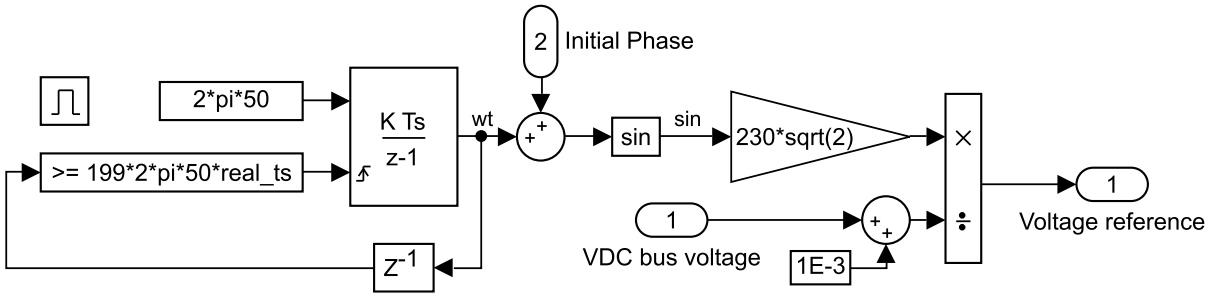

Figure A.10: V2H voltage reference generator

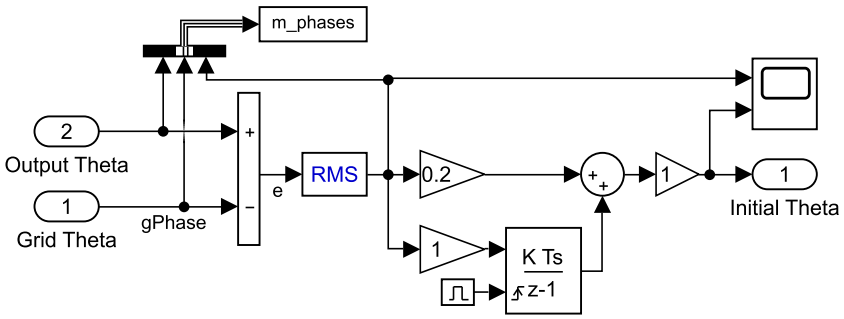

Figure A.11: V2H output phase controller for re-synchronization with the grid

A.1.7 BDC control

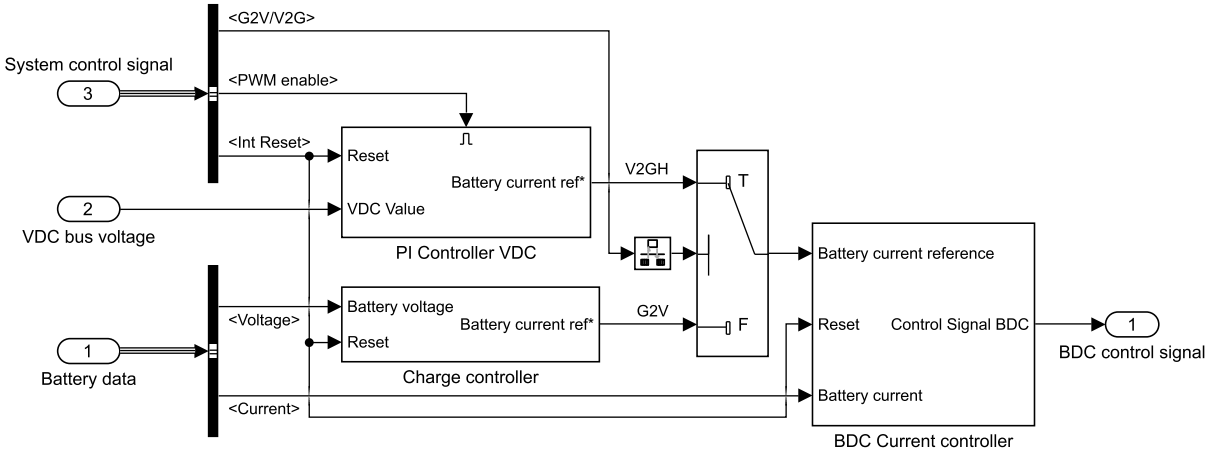

Figure A.12: BDC control overview

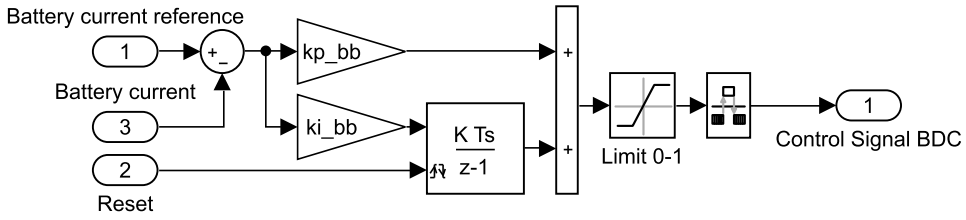

Figure A.13: BDC current controller

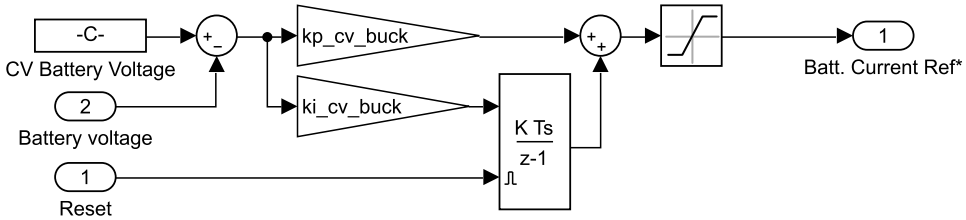

Figure A.14: BDC constant-voltage charging current controller

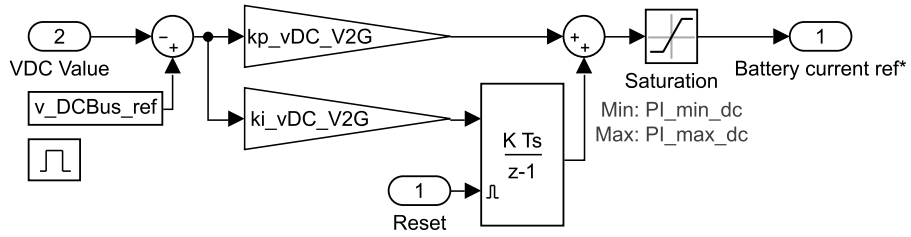

Figure A.15: BDC V_{DC} controller

A.1.8 Fault detection module

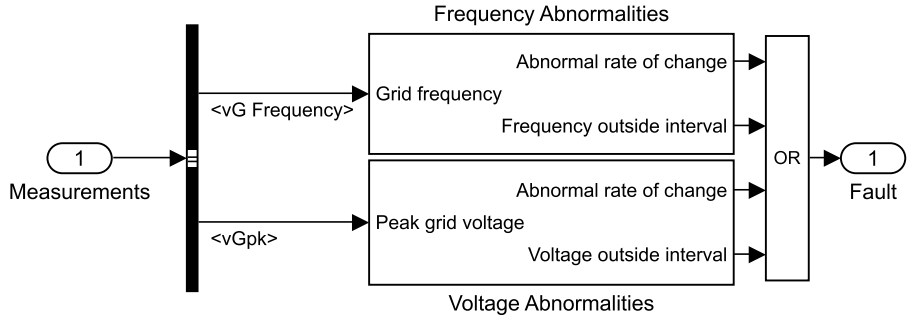

Figure A.16: Fault detection module overview

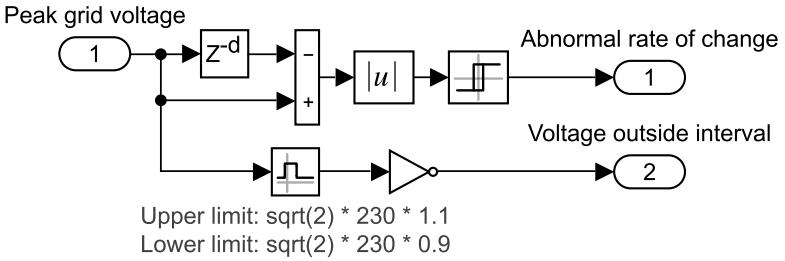

Figure A.17: Voltage fault detection

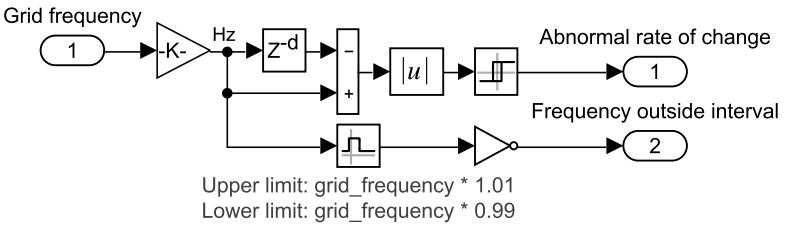

Figure A.18: Frequency fault detection

A.1.9 Pulse-Width Modulation

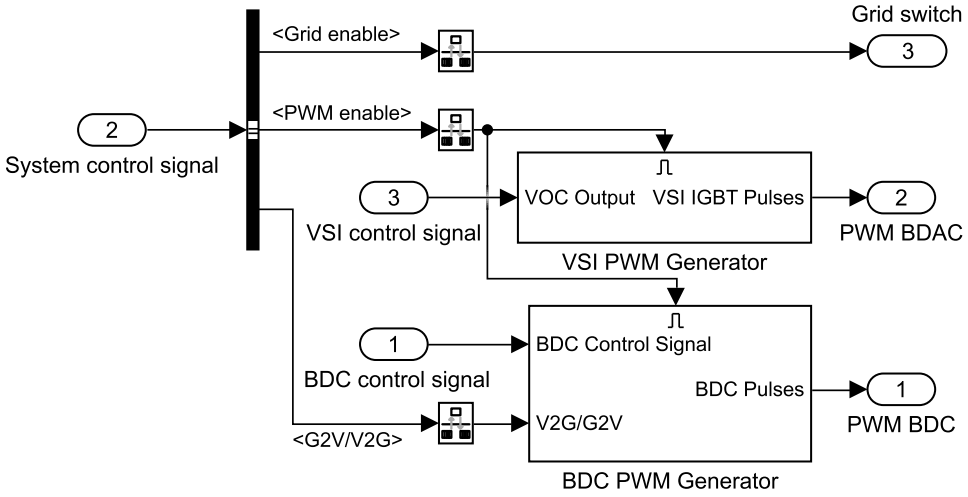

Figure A.19: PWM

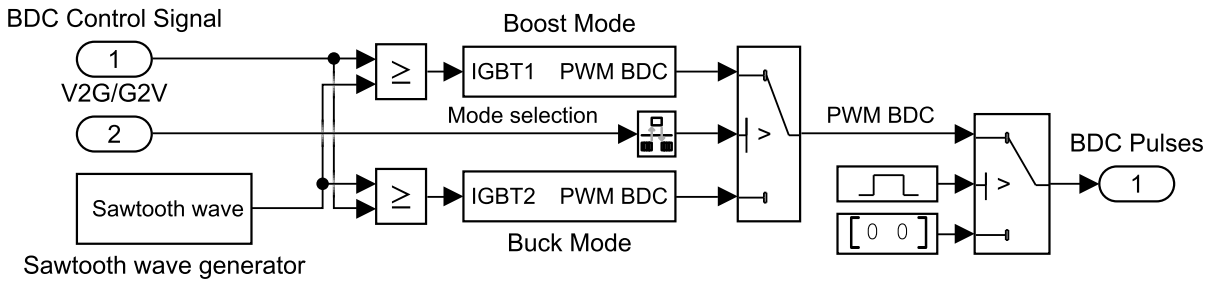

Figure A.20: BDC PWM

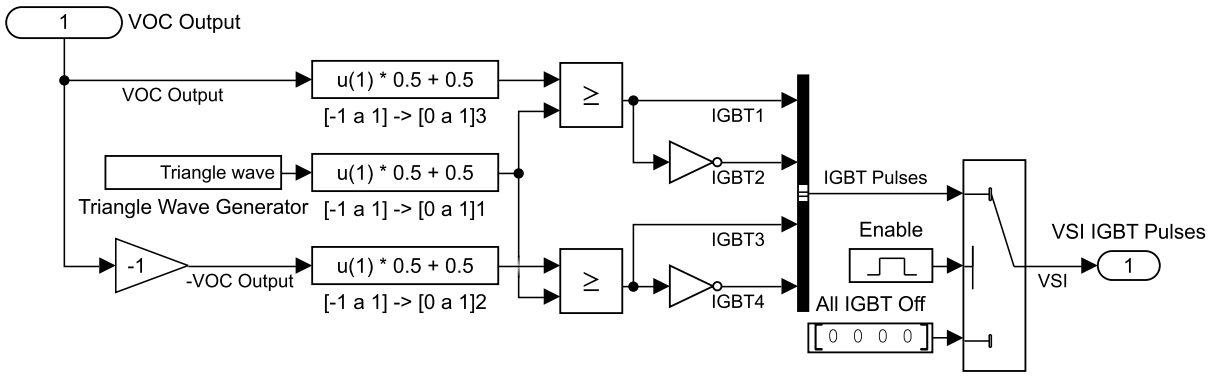

Figure A.21: BADC PWM